The Dissertation Committee for Curtis Paul Rasmussen Certifies that this is the approved version of the following Dissertation:

BROKEN PASSIVITY AND TIME-REVERSAL-SYMMETRY BOUNDS IN ACOUSTIC DEVICES

Committee:

Michael R. Haberman, Supervisor

Andrea Alù, Co-Supervisor

Mark F. Hamilton

Preston S. Wilson

BROKEN PASSIVITY AND TIME-REVERSAL-SYMMETRY BOUNDS IN ACOUSTICS DEVICES

by

Curtis Paul Rasmussen

Dissertation

Presented to the Faculty of the Graduate School of

The University of Texas at Austin

in Partial Fulfillment

of the Requirements

for the Degree of

Doctor of Philosophy

The University of Texas at Austin

August 2021

Dedication

For Annie, who is music.

Acknowledgements

My fascination with acoustics grew out of a love of music. Whether at the piano, in the car, or in the church, I found early on that beat and melody have the power to stir my soul. Thank you to my parents for a childhood filled with song.

To my parents and siblings: thank you for the many years full of fun and for always believing in me. You are where I find strength. I am grateful also for the love and support of the incredible relatives I won through marriage. And to the new generation coming along: welcome to the party. You will find love here.

My advisor, Andrea Alù, is nothing short of a powerhouse. Thank you, Andrea, for the insightful edits, stimulating brainstorms, and valuable career guidance over the years. Your remarkable combination of intellectual brilliance, dedicated work ethic, and constant willingness to help has benefitted me enormously, and I am grateful.

I am also deeply indebted to my professor at the University of Texas at Austin, Mike Haberman. It was with his help that I was able to secure the fellowship that funded most of my research. I am grateful to his research group for their friendship and for letting me use the lab equipment that made my experimental work possible. Thank you, Mike, for introducing me to acoustic metamaterials and for the years of helpful feedback on my work.

My gratitude also belongs with the mentors who have led me to where I am. Thanks to Kent Gee, Jon Blotter, Scott Sommerfeldt, and Brian Anderson at Brigham Young University, for getting me started in acoustics and for their support and wise guidance over the years. And thank you to Ben Bard. I had such a good time working for him. He showed me how to be a leader and I thank him for his friendship.

The acoustics program at the University of Texas at Austin is a well-oiled wonder. Thank you to Mark Hamilton whose classes could not possibly be any better. His lectures on physical acoustics gave me the analytical tools I needed to carry out the work described here. And thank you to Preston Wilson for teaching me transducer circuit theory, which has likewise proved invaluable time and again for my research. Thanks also to those who organized the weekly acoustics seminars, wide-ranging and always interesting.

As luck would have it, my lab mates were all uncommonly interesting and kind people. I thank them for their friendship and wish them all the best in their various pursuits around the world. Thank you to Robert Duggan for being sounding board number one and a friend to my family. To Hoyeong Kwon, for always keeping things fun and for having a car. Thank you to Li Quan, Yarden Mazor, and Dimitrios Sounas for stimulating discussions and productive collaborations. And thanks to the rest of the crew: Zhicheng Xiao, Ahmed Kord, Sander Mann, Mykhailo Tymchenko, Guangwei Hu, Yoshi Kasahara, Younes Ra'di, Matt Byrne, Diego Farfan, Michele Cotrufo, and Alex Krasnok. They are all scholars of the highest order and I feel lucky to have worked alongside them.

I appreciate the support of the many staff members without whose help my research would have been impossible. Thank you to Diana Strickland for her friendly assistance, from coordinating the lab move to scheduling the excellent weekly presentations. And a big thanks to Karen Little and Apipol Piman of the WNCG. They kept everything running smoothly for me despite the complications of coordinating an external fellowship, assisted in the huge task of moving a research lab across the country, and coordinated our office space as we settled into the beautiful new EER building.

I was thrilled to have the freedom to explore that comes with generous funding. The lion's share of this freedom came from the NDSEG fellowship sponsored by the Office of Naval Research. Thank you for your trust in me. Thank you also to the University of Texas

at Austin whose initial funding got me started on the right foot and to the Acoustical Society of America for their scholarship support.

To my kids, I love you. Whether you remember them or not, we had so many fun adventures around Austin these past few years. And I got a kick out of hearing your little voices repeat the names of my classes ("Electromagnetic field theory," "Nanophotonics"). You make me happy.

And to Annie – you are the one. When we met, it was the satisfying snap of two magnets coming together. And it just keeps getting better, doesn't it? You are my partner in learning. I owe this all to you.

Abstract

Broken Passivity and Time-Reversal-Symmetry Bounds in Acoustic Devices

Curtis Paul Rasmussen, Ph.D.

The University of Texas at Austin, 2021

Supervisors: Michael R. Haberman, Andrea Alù

We collect information about the world through our senses, two of which, hearing and touch, are attuned to the mechanical vibrations travelling around us. Scientists and engineers have learned to control these acoustic waves, and in so doing they have opened new possibilities in how we interact with each other and the natural world. One area of rapid progress is acoustic metamaterials, which are architected structures that can shape sound waves in ways that go beyond what is possible with natural materials. Given the potential of these new materials, it is important to consider their limits and identify the underlying physical principles responsible for them. In this dissertation we examine limitations in the response of acoustic materials and devices due to passivity and time-reversal symmetry.

An important constraint that arises due to time-reversal symmetry is reciprocity. Reciprocity must be broken to create devices that allow sound through in only one direction. This work explores acoustic nonreciprocity with particular attention to applications in surface acoustic wave devices and topological acoustic demonstrations.

One way to achieve acoustic nonreciprocity is with fluid flow. Based on this technique, we present an acoustic Mach-Zehnder isolator and nonreciprocal leaky-wave antenna.

A different but equally fundamental and important constraint in acoustics technology is the trade-off between the size, efficiency, and bandwidth of a small resonator. By considering arbitrary stored and radiated sound fields surrounding a compact source, we derive a theoretical lower bound on the quality factor of a passive acoustic radiator. This work discusses opportunities to overcome this constraint by considering active resonators. We experimentally demonstrate a three-fold bandwidth improvement to the passive case by synthesizing a non-Foster circuit load for a piezoelectric sonar transducer.

By using a Green's function approach and by connecting the physics of a disordered array to the statistical theory of random walks, we also explore the physics of near-zero-index materials, and leverage their unusual sound-matter interactions to enable robust and highly directive acoustic sources. This work introduces an entirely new way to achieve highly directional sound beyond traditional techniques.

Table of Contents

List of Figures

Figure 2.4: Topological acoustics. (a) Photograph of mechanical Chern insulator consisting of a plate with attached piezoelectric disks. Synthetic angular momentum biasing is imparted by modulations in circuits connected to the piezoelectric disks. Darabi et al., Sci. Adv. 6, eaba8656 (2020). Copyright 2020 Author(s), licensed under a Creative Commons Attribution (CC BY) license. (b) Displacement measurements show an excitation traveling around the perimeter of the system, protected against defects by the topological order of the 2D lattice. Darabi et al., Sci. Adv. 6, eaba8656 (2020). Copyright 2020 Author(s), licensed under a Creative Commons Attribution (CC BY) license. (c) In a demonstration of topological pumping in airborne acoustics, the boundary of an acoustic waveguide is modulated by the mechanical rotation of a shaft. Sound is topologically transported through the waveguide when incident from the right end, but largely blocked when incident from the left end. Reproduced with permission from Xu et al., Phys. Rev. Lett. 125, 253901 (2020). Copyright 2020 American Physical Society. (d) Left: The eigenfrequency evolution as a function of the crank angle over a complete cycle. Right: The normalized pressure in the waveguide at points (i)–(iii). Solid lines are theoretical results; markers show the experimental results. Energy supplied to the right end feeds the right localized mode, crosses the bulk, and ends up in the edge state on the opposite side after the pump cycle is completed. Reproduced with permission from Xu et al., Phys. Rev. Lett. 125, 253901 (2020). Copyright 2020 American Physical Society. (e) In another demonstration of topological pumping, two arrays of hollow cylinders

Chapter 1: Introduction

1.1 Broken time-reversal symmetry

While sound is not visible to the human eye, with a little imagination we can visualize the songs of birds or the rumble of passing cars as waves expanding outward and bouncing through the surrounding landscape. We can create mental movies of passing sound waves by visualizing sound in this way and even imagine how these movies would look if played backward. Through this mental exercise, we find that many sound waves look perfectly natural when they are reversed. For example, the sound wave of a birdsong travelling by from left to right when played backwards simply looks like a birdsong moving instead from right to left. The movie played backwards appears to obey the laws of physics as readily as when played forward and we would simply suppose that the unseen songbird was on our right instead of on our left. Even the sound waves spreading out from a concert violinist on a stage could be reversed and still look plausible – we would simply need to envision a large array of speakers surrounding the violinist, all simultaneously playing a recording of the musical number, creating waves that, instead of emanating away, converge toward the violinist. This ability of sound waves to look natural either forward or reversed is due to the time-reversal invariance of acoustic wave propagation. Mathematically, the scalar wave equation, $\partial_t^2 p = c^2 \nabla^2 p$, is invariant under the transformation $t \rightarrow -t$. Time-reversing a solution of this equation returns an equally valid solution [1].

How can this reversibility be broken? Perhaps the simplest effect that breaks time-reversibility is loss. As sound travels, it decreases in volume both through geometrical spreading and through absorption. The spreading effect is perfectly time reversible, but absorptive losses violate the reversal relationship. Imagine the birdsong passing from left to right. As it travels, it loses to heat about one decibel of sound pressure level for every

one hundred meters that it travels due to dissipative effects. In the forward version of the mental movie, we picture a passing wave that fades in strength as it travels with the surroundings slightly heated by its passing. The movie played in reverse shows a wave that mysteriously seems to suck up heat and gains in strength as it passes from right to left. This looks unnatural as it violates the second law of thermodynamics. The absorption process is time-reversible in the sense that the heat, which is composed of a multitude of collisions and vibrations of air particles, could conspire in perfect unison to add amplitude to a passing sound wave, but this process goes against the grain of the inevitable local entropy increase and so we say it breaks the time-reversibility.

Other effects break time-reversal symmetry while, additionally, violating another important symmetry of wave propagation, namely reciprocity. Reciprocity relations are mathematical equivalencies between signals received when source and receiver locations are swapped [2,3]. These relations are inherent to linear, time-invariant wave propagation in the presence of time-reversibility. Effects based on the motions of particles that modify acoustic wave propagation can break reciprocity [4]. Examples include fluid flow (i.e., wind currents carrying sound waves), magnetoelasticity (i.e., moving charged particles creating magnetic fields that couple to acoustic vibrations), and elastic gyricity (i.e., spinning particles coupling to acoustic vibrations). Reciprocity is violated as there is a coupling between these motions and the wave motion that does not occur equally from different directions.

To check whether these material motions break reciprocity or time-reversal symmetry, we examine the behavior of wave propagation in the reciprocal scenarios while the directions of these motions remain unreversed. For reciprocity, we examine the effect of swapping source and receiver locations while the material motions are unchanged. For time-reversal symmetry, we play the movie forward and backward while keeping the

motions moving in the same direction in both cases. If reversing the movie while keeping the motions unchanged is unphysical, we say that there is broken time-reversal symmetry. Defining broken time-reversal symmetry or reciprocity in this way is useful from an engineering standpoint as a typical scenario involves a device that includes some symmetry-breaking motions which are steady, no matter the direction acoustic waves might take through it.

These concepts and definitions are illustrated by continuing the birdsong example. We suppose there is a steady wind blowing from left to right, speeding up the chirps and whistles of a songbird on the left as its song heads with the wind. We play the movie backward now, keeping the wind in its left-to-right direction, and it looks unnatural because the sound, now going against the wind, is travelling faster than it should. The time-reversal symmetry is broken. Reciprocity is broken as well as there is a difference between signals recorded by two microphones – one on the right recording a birdsong from the left and another on the left recording an identical birdsong from the right (see Ref. [5] for a discussion of reciprocity broken by flow). The broken reciprocity is evident as the two recorded signals are time-shifted relative to each other. The birdsong begins sooner in the recording of the right microphone compared to that of the left due to the rightward wind. As a further example, we consider a wind that is instead blowing directly up from out of the ground, say through a vent under our feet. As the wind is now perpendicular to the motion of the sound, whose propagation we take to be in the horizontal plane, the effect of the wind is to sweep the sound up vertically in the air as it passes. In the forward movie we see sound travel from lower left to upper right in the presence of an upward wind; in the backward movie we see sound travel from upper right to lower left, which is clearly at odds with the upward wind. Again, time-reversal symmetry is broken. However, reciprocity is intact as swapping source and receiver between right and left locations results in identical

recorded signals. While wind or other material motions are able to break reciprocity, the breaking is not guaranteed.

Breaking time-reversibility is useful as it enables acoustic phenomena and devices where sound behaves differently when the wavenumber, and therefore the direction of travel, is reversed. This includes beamforming arrays that can receive and transmit in different directions [6,7], one-way acoustic waveguides that are immune to backscatter [6,8,9], and structures hosting topologically protected unidirectional surface states [10–12].

1.2 BROKEN PASSIVITY

When sound passes through a material without gaining energy there are restrictions placed on the wave's behavior. The absence of acoustic gain is known as passivity and it implies causality, where a material's response function describable by a convolution integral has no contribution from future times [13]. In a passive material, the real and imaginary parts of the response function are connected through the Hilbert transform (the Kramers-Kronig relations). These relations imply that exotic material parameters are always accompanied by frequency dispersion, which limits the functional bandwidths of passive devices. Additionally, in passive reciprocal materials, the imaginary part of the acoustic density and bulk modulus are necessarily positive (for the $e^{-i\omega t}$ convention) [14].

Breaking passivity requires an energy source that can feed the acoustic wave. While material flows such as ocean currents or gyric materials composed of rotating spinners may contain motions that break reciprocity, they do not supply energy to acoustic waves and are unable to create acoustic gain. This can be understood by considering that, in the absence of friction, these motions require no energy input in order to be maintained. A force is required to get a flow circulating in a waveguide, but after the initial acceleration, no more force is needed. In the linear acoustic model, a passing sound wave extracts no

energy from the motion, though its propagation is affected. Other techniques are needed to couple energy into the wave. Passivity can be broken using an electroacoustic transducer loaded with a gain element such as an op amp. This is a straightforward way to break passivity in acoustics due to the maturity of electroacoustic transducer technology [15]. Time-modulation can also provide energy to acoustic waves, such as with a parametric pump [16].

New functionalities are unlocked through the inclusion of gain elements. By breaking passivity, the narrow ranges of exotic material parameters implied by the Kramers-Kronig relations can be widened. It has been shown, for example, how it is possible in an active material to achieve a constant negative material parameter over a finite frequency range [17,18]. For sources, breaking passivity can widen the bandwidths of radiation resonances as it circumvents a fundamental relationship between radiator size and bandwidth, known in electromagnetics as the Chu limit. This limit, a consequence of the inevitable stored energy surrounding a source, constrains the useable bandwidth and efficiency of small radiators and effective materials composed of subwavelength resonators. Another constraint that is broken through the use of gain is Foster's reactance theorem. Applicable to systems describable by a one-port network representation, Foster's theorem states that, in the absence of loss or gain, the system's reactance or susceptance always increases with frequency [19,20]. A consequence of this is the inability of passive systems to provide broadband impedance compensation. Loss may be introduced to improve the bandwidth performance, but only at a loss of efficiency. Through the use of gain media, wider impedance compensation bandwidths are enabled without necessarily degrading efficiency.

Idealized components, such as negative inductors, capacitors, and resistors can be synthesized from active elements and act as conceptually simple building blocks for use in

electroacoustic circuit models. Negative resistances can be used to compensate the positive resistances that arise due to inevitable losses from dissipation in propagation or inefficiencies in transducers. Furthermore, with suitable spatial arrangements of gain and loss, novel parity-time symmetric effects, such as unidirectional transparency and a decoupling between an emitter and the eigenstates of its environment are made possible [15,21–24]. It should be noted, however, that active systems do not enjoy the same protection from instabilities that passive systems enjoy. Instabilities, where the wave amplitude grows without bound either at a single point (absolute instability), at a moving point (convected instability), or in a bounded medium (global instability) may be introduced and in many applications must be avoided.

1.3 DISSERTATION ORGANIZATION

This work explores broken time-reversal symmetry and passivity in acoustics, through theoretical analysis and experimental demonstrations. Chapter 2 is an overview of acoustic nonreciprocity, including an introduction to reciprocity theorems and techniques used to break them. The wide usefulness of broken reciprocity is made clear through a review of promising applications, such as surface acoustic wave technology and topological acoustics. In chapter 3, nonreciprocal devices based on material flow are presented, including the acoustic Mach-Zehnder isolator which allows sound to pass through in only one direction and a nonreciprocal metamaterial leaky-wave antenna capable of transmitting in a different direction than it receives. In chapter 4, the acoustic Chu limit is developed and it is shown how, by breaking passivity, a synthesized non-Foster circuit element can widen resonant bandwidths. In an experimental demonstration, the amplitude-bandwidth of a piezoelectric transducer is improved by 450% while maintaining system stability. A discussion of the applicability of the technique to acoustic

metamaterials is also included, with exotic material properties realizable over large bandwidths. Chapter 5 presents a highly-directive acoustic source based on a metamaterial compressibility-near-zero response. Conclusions and future work are outlined in chapter 6.

Chapter 2: Acoustic nonreciprocity[1]

In this chapter we further consider the similarities and differences between time-reversal symmetry and reciprocity and give a broad review of recent research in broken reciprocity. Breaking reciprocity is one of the main motivating factors in current research on time-reversal-symmetry-breaking effects as it is essential in creating robust one-way propagation where sound waves or elastic vibrations are permitted to travel in only one direction. This unidirectional response forms the basis for devices such as acoustic isolators and circulators, and it also unlocks new functionalities for complex systems such as acoustic topological insulators. After reviewing the principles of acoustic reciprocity, we look at techniques to achieve large reciprocity breaking, including nonlinearities, moving media, spatiotemporal modulation, and nonlinear bianisotropy. We then discuss the recent surge of progress in nonreciprocal surface acoustic wave devices and topological acoustic systems, areas which we predict will continue to flourish in the coming years. We anticipate that these and other applications of nonreciprocity will continue to enhance acoustic technology and form the basis for new acoustic devices. Reciprocity is a fundamental principle in wave manipulation, and techniques for breaking its symmetry will continue to be discovered, refined, optimized, and applied to several acoustic domains as the understanding of the underlying principles and new technologies mature.

2.1 INTRODUCTION

The study of acoustics explores the excitation, propagation and measurement of acoustic waves in natural and engineered environments. Among these, the study of acoustic propagation has flourished in the past twenty years, in large part due to the emergence of

[1] Reprinted from C. Rasmussen, L. Quan, and A. Alù, Acoustic nonreciprocity, J. Appl. Phys. **129**, 210903 (2021), with the permission of AIP Publishing.

acoustic metamaterials [25–27], which have greatly extended our ability to manipulate sound waves. Early studies focused on the exploration of reciprocal functionalities. In this scenario, acoustic metamaterials, no matter the complexity of their structure and no matter how counterintuitive their routing of acoustic waves may be, are subject to the rule of reciprocity. That is, if we interchange the location of sound source and receiver the received signal will always be the same, regardless of the microstructure of the material. This general rule is satisfied in both time and frequency domains.

The concept of reciprocity is easily confused with time-reversal symmetry, as they are both symmetries between two different wave fields with strong relations with each other. Time-reversal symmetry can be understood by visualizing a video of an acoustic wave played backward. When this backward-scrolling video is an allowed physical process (that is, it obeys the relevant laws of physics), time-reversal symmetry is intact. This global reversing of the wavefield in a region of space is the central focus of the field of time-reversed acoustics [1]. For example, a time-reversed acoustic experiment may seek to create a converging spherical wave, the time-reversed version of a point source, where an array of sources is used to create the converging wave with a focus at the location where the original source would reside. Studies in acoustic reciprocity differ in that they are typically concerned with the symmetric relation between a source and receiver. That is, instead of examining the relationship between a forward and a fully-reversed wave field, reciprocity establishes a relationship between field amplitudes and phases at locations or ports in wave fields that may appear globally quite different from each other. There is also the difference that strict time-reversal means that all involved physical processes must be reversed, whereas reciprocity is typically concerned with reversing propagation features. This difference is apparent in the presence of material loss, which is the most common example in which reciprocity and time-reversal symmetry diverge. When an acoustic wave

travels through a lossy medium the wave energy is dissipated through countless microscopic collisions of the particles in the medium. When time is reversed (i.e., the movie is played backward) the inverted collisions perfectly come together to create gain for the reversed wave. The movie looks unrealistic because it shows an unlikely local spontaneous decrease in entropy, but the Newtonian equations describing the collisions have not been violated. In reciprocity, sources and receivers are swapped, but material loss can still be present, implying that waves are equally attenuated in either direction, as it would occur in a realistic experimental setup. In a reciprocal system, transmission in opposite directions is still identical, even though the lossy channel obviously does not obey time-reversal symmetry as the signals decay in both directions. It is for this reason that, compared with time-reversal symmetry, reciprocity is often considered a more general phenomenon in wave engineering [28].

The reciprocity principle was originally introduced by Helmholtz in 1860 [2]. It concerns the definition of acoustic reciprocity where, by interchanging the sound source and receiver, both the amplitude and phase of the received signal remain the same. This general notion of reciprocity can be illustrated by considering the very familiar example of human communications. We assume that if we can hear someone talking to us, they should be able to hear us if we talk back to them with the same volume. We do not expect the shape of the room or any nearby sound absorbing materials to change this property, which is an intuitive understanding that reciprocity holds even in the presence of spatial inhomogeneities and linear dissipation.

Acoustic reciprocity may also involve reciprocal couplings of the acoustic field with other phenomena, for example, electromagnetic waves. Many acoustic transducers used for sound generation and reception are based on the coupling of acoustic and electromagnetic phenomena in piezoelectrical materials. This coupling obeys reciprocity,

hence, if the electrical and acoustic signals are interchanged, the piezo-electric and electric-piezo switching efficiencies are identical. With this property, an acoustic transducer can be utilized as both a sound source and an acoustic sensor.

The photoacoustic (or optoacoustic) effect, based on which ultrasound waves are generated by the thermal expansion of a material as it absorbs light, is another situation in which acoustic propagation involves other phenomena. Interestingly, reciprocity does not hold for this effect. Photoacoustic waves are generated by light absorption in a material sample, causing thermal expansion, and then resulting in ultrasound propagation [29]. The reversed coupling effect, i.e., generating light by sound waves has been rarely reported due to thermal phenomena being involved in the coupling. Actually, the reciprocity principle can be broken in several other situations. Aside from nonreciprocal coupling with other phenomena, any kind of acoustic nonlinearity or bias through moving media will result in nonreciprocity. In fact, the acoustic wave equation itself is nonlinear, indicating that acoustic propagation can become nonreciprocal as the intensities grow in the presence of geometrical asymmetries [30–33]. Only in the small signal approximation can the wave equation be considered linear and admit a reciprocity principle.

Biased moving media, such as air currents between two speakers, also breaks the symmetrical transmission of reciprocity as sound propagation in the upstream and downstream directions are different. So why do we adopt acoustic reciprocity in our daily life? Why, when conversing with others, do we generally not notice any asymmetry? Because in most scenarios the acoustic pressures involved are indeed very small and because the speeds of any nearby breeze are often tiny compared with the speed of sound. The resulting small amounts of nonreciprocity are too weak to be observed or matter. The aim of nonreciprocal acoustic wave engineering, then, is to strengthen these effects by developing techniques to enlarge nonreciprocity for small pressure amplitudes and slow-

moving media. While any amount of nonlinearity or external modulation breaks the exact reciprocity symmetry, in practice systems must be carefully designed to achieve an effect large enough to be useful. Two useful metrics in quantifying nonreciprocity are isolation, commonly defined as the ratio between forward and backward transmission, and insertion loss, which is how much signal power is lost in the forward transmission due to the presence of the nonreciprocal element. We will first review statements of reciprocity in acoustics, then discuss techniques for large reciprocity breaking, highlighting some of the promising applications for nonreciprocity and discussing future possibilities for this vibrant field of research.

2.1.1 Example reciprocity statements in acoustics

A reciprocity relation is any symmetrical relation between field quantities when sources and receivers are interchanged. For example, suppose there is a monopole source distribution m_i and a dipole source distribution $\boldsymbol{d}_i$ in the acoustic field (p_i, $\mathbf{v}_i$), where i can be 1 or 2, indicating acoustic fields generated by source distributions 1 and 2, respectively. In the frequency domain, the sound equations can be written as

$$-i\omega\frac{p_i}{\rho_0 c_0^2}+\nabla\cdot\mathbf{v}_i=-i\omega\frac{m_i}{\rho_0}, \tag{2.1}$$

$$-i\omega\rho_0\mathbf{v}_i+\nabla p_i=-\omega^2\mathbf{d}_i. \tag{2.2}$$

After some mathematical manipulation, we can arrive at the reciprocity relation

$$\iiint_V\left(p_1m_2-p_2m_1+i\omega\rho_0\mathbf{v}_1\cdot\mathbf{d}_2-i\omega\rho_0\mathbf{v}_2\cdot\mathbf{d}_1\right)=0. \tag{2.3}$$

Suppose there is a monopole source $m_1=M_1\delta\left(\mathbf{r},\mathbf{r}_1\right)$ located at $\mathbf{r}_1$ and another monopole source $m_2=M_2\delta\left(\mathbf{r},\mathbf{r}_2\right)$ located at $\mathbf{r}_2$. Substituting these into Eq. (2.3), we get

$$\frac{p_1(\mathbf{r}_2)}{M_1} = \frac{p_2(\mathbf{r}_1)}{M_2}. \tag{2.4}$$

If we assume $M_1 = M_2$, Eq. (2.4) indicates that the acoustic pressure at $\mathbf{r}_2$ produced by a monopole source at $\mathbf{r}_1$ will be identical to the acoustic pressure at $\mathbf{r}_1$ produced by a monopole source at $\mathbf{r}_2$, as sketched in Fig. 2.1(a).

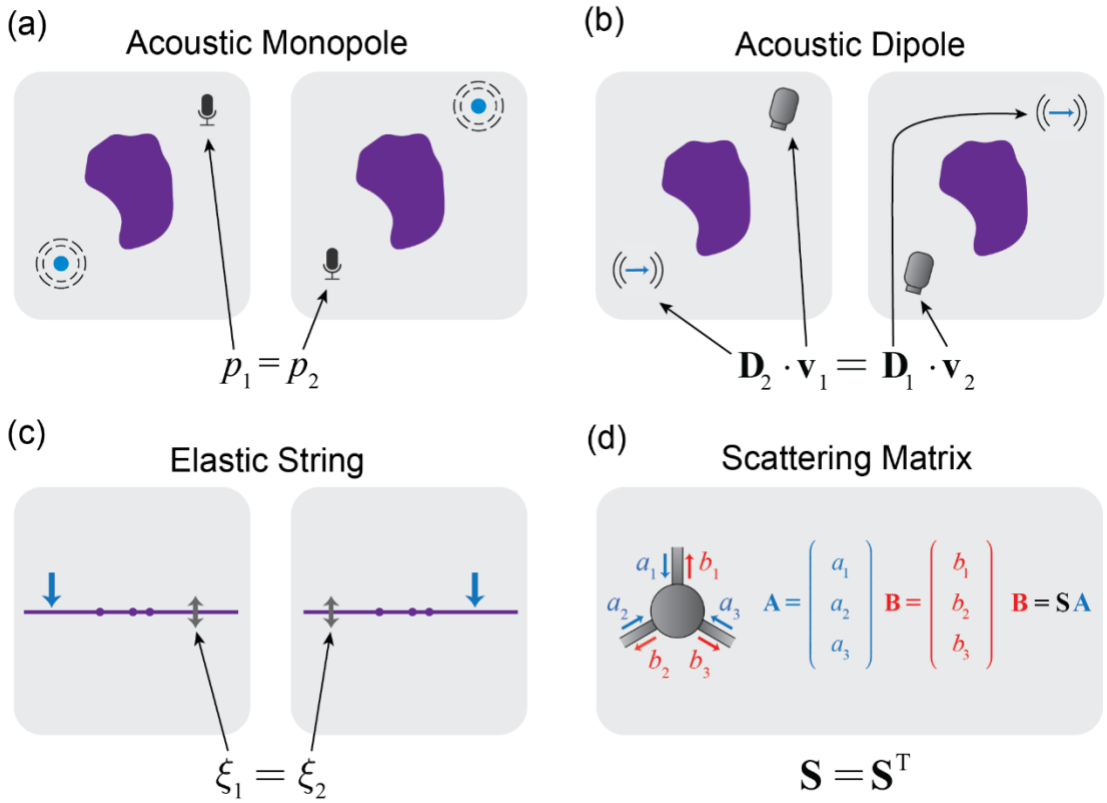

Figure 2.1: Forms of acoustic reciprocity. Reciprocity indicates a symmetry between two fields when sources and receivers are interchanged. (a) For monopole sources, the pressure at a receiver in field 1 is equal to the pressure at a receiver in field 2 when the source and the receiver are swapped. (b) Projected acoustic velocities are equal for acoustic dipole sources. (c) In an elastic string, the induced displacements are equal. (d) In a scattering problem with well-defined ports, reciprocity is the condition that the input and output ports are related by a symmetric scattering matrix.

If there is instead a dipole source $\mathbf{d}_1 = \mathbf{D}_1 \delta(\mathbf{r}, \mathbf{r}_1)$ located at $\mathbf{r}_1$ and another dipole source $\mathbf{d}_2 = \mathbf{D}_2 \delta(\mathbf{r}, \mathbf{r}_2)$ at $\mathbf{r}_2$, from Eq. (2.3) we get

$$\mathbf{D}_2 \cdot \mathbf{v}_1 = \mathbf{D}_1 \cdot \mathbf{v}_2. \tag{2.5}$$

This reciprocity relation is illustrated in Fig. 2.1(b). If we suppose $\mathbf{D}_2 = \mathbf{D}_1$ and they are both in the *x*-direction, we could infer $v_{1x} = v_{2x}$, indicating that the *x*-component of the particle velocity at $\mathbf{r}_2$ produced by an *x*-directed dipole source at $\mathbf{r}_1$ will be identical to the *x*-component of the velocity at $\mathbf{r}_1$ produced by an *x*-directed dipole source at $\mathbf{r}_2$. Other forms of reciprocity follow similar derivations, for example a statement of reciprocity in an elastic string, where the induced displacements due to interchanged loads are equal [Fig. 2.1(c)], and in a general scattering formalism, where the reciprocity statement implies that the resulting scattering matrix is symmetric [Fig. 2.1(d)].

2.1.2 Nonreciprocity research in electromagnetics

Research on reciprocity breaking in electromagnetics began earlier than in acoustics in part because magneto-optical materials, which can strongly break reciprocity through the application of a dc magnetic bias, are relatively common in nature. Hence, the earliest nonreciprocal wave devices were mostly based on ferrites and found application in both microwave engineering and optics. The principle of magneto-optical nonreciprocity is to utilize the biasing static magnetic field to influence the electron cyclotron orbiting motion inside the material, which nonreciprocally affects electromagnetic wave propagation through the material. This is the working principle of the earliest electromagnetic waveguide circulators and isolators [34,35]. However, nonreciprocal devices based on magneto-optical media are usually bulky and large because the underlying phenomena are rather weak, which prevent on-chip integration.

Later, several magnetic-free approaches were proposed to break reciprocity. Inspired by the biased magnetic field to break reciprocity, an effective approach was to use dynamic modulation to create an effective magnetic field [36]. In this technique, although there is no real magnetic field biasing the structure, a gauge field is formed that mimics the magnetic field and can manipulate light nonreciprocally [37]. Spatio-temporal modulation on the basis of resonant systems was then proposed by mimicking angular momentum as a way of replacing the magnetic bias, which removes the degeneracy between opposite resonant states, to realize giant nonreciprocity with modest requirements on the modulation frequency and amplitude. This approach was first applied by modulating effective material parameters [38], and it was later introduced into circuit designs [39] and finally realized in on-chip integration [40]. Other approaches to break electromagnetic reciprocity are based on nonlinear materials combined with geometrical asymmetries [41–43].

2.2 BREAKING RECIPROCITY IN ACOUSTICS

Similar techniques have found success in breaking acoustic reciprocity. In general, reciprocity theorems cease to apply in the presence of effects that violate the underlying assumptions of linearity, passivity, and time-invariance, though their presence does not guarantee broken reciprocity. For example, as sketched in Fig. 2.2(a) for an acoustic wave, reciprocity may be broken as the wave passes through a nonlinear medium, but only if there is an accompanying spatial asymmetry. Aside from nonlinearity, reciprocity can also be violated by the presence of any quantity that is odd under time reversal, meaning that their sign changes with a change of sign of the time coordinate (the position of the particle is time even – the length quantity is unchanged by the time reversal; the velocity of a particle is time odd – the time reversal switches its direction). For this reason, reciprocity does not hold when an acoustic wave is travelling through moving media, such as an ocean current.

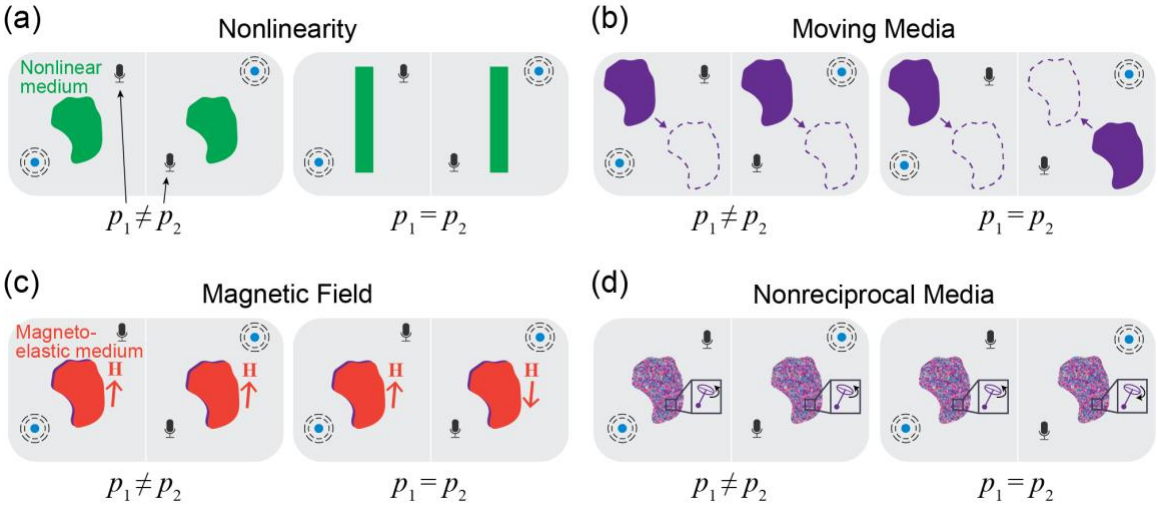

Figure 2.2: Breaking acoustic reciprocity. (a) Nonlinear media can break reciprocity. However, reciprocity is maintained unless there is spatial asymmetry. (b) Moving media, such as airflow, can break reciprocity between fields 1 and 2 as the direction of motion of the media is the same in both scenarios. (c) Nonreciprocity is induced when a magnetic field couples to an acoustic wave, as in the case of a magnetoelastic medium in the presence of an external magnetic bias H. This can also be understood as a moving medium, considering that the dc magnetic field is moving charged particles. (d) A medium with nonreciprocal microstructure, such as an elastic gyric medium, displays nonreciprocity. This is again a form of moving medium, as it is a result of microscopic motions that are not reversed in the two scenarios.

However, reciprocity is restored if the time-odd quantities are reversed along with the source and receiver positions [Fig. 2.2(b)]. Magnetic fields, which arise due to moving charged particles, break reciprocity unless the direction of the charged particles (and hence the direction of the magnetic bias) is also reversed [Fig. 2.2(c)]. And reciprocity only holds for nonreciprocal media, where the homogenized material properties arise from hidden sources of motion such as gyroscopic spinning as in Fig. 2.2(d), when the directions of the hidden motions are reversed. As examples of techniques to break reciprocity, we now discuss nonlinearity, moving media, spatiotemporal modulation, and bianisotropy in greater detail.

2.2.1 Nonlinearity

In principle, the acoustic wave equation is nonlinear, and strong nonlinear features may be observed as the intensities grow. Nonlinearity in acoustics can introduce frequency harmonics, seen in the time response as waveform distortions, and an amplitude-dependent response, which results from effective material properties that vary with the amplitude. The systematic study of nonreciprocal acoustics started by looking at nonlinearities. In 2009, by combining a phononic crystal with nonlinear materials, a so-called acoustic diode was proposed to realize sound energy isolation [30]. The idea is to place a phononic crystal adjacent to a nonlinear material so that the phononic crystal is able to block sound waves at the fundamental frequency while allowing transmission of the second harmonic. If the acoustic wave encounters the phononic crystal first it is totally blocked. But, when incident from the opposite direction, the wave passes instead through the nonlinear material first where some of the acoustic energy is converted into the second harmonic and is then free to pass through the phononic crystal. Due to the effective filter function of the phononic crystal, the transmission asymmetry for this system can be very high. However, since there is no phase-matching in the system, energy conversion from the fundamental frequency to the harmonic is very limited, resulting in a comparatively low working efficiency. This proposal was implemented experimentally by utilizing the high nonlinearity of ultrasound contrast agent microbubbles [31]. To overcome the low efficiency in energy conversion, an active approach was then proposed [32]. Here, Helmholtz resonators were used for frequency filtering in place of a phononic crystal and a loudspeaker was used in place of a nonlinear media. In 2011, a different approach based on bifurcation-based acoustic switching was proposed for sound isolation [33]. Similar designs have included modulating geometric nonlinearity [44] and utilizing nonlinear interfaces [45]. These nonlinear approaches to nonreciprocity do not require frequency shifting and energy conversion, and

hence are able to operate at the fundamental frequency. However, due to the involved nonlinearities, waveform distortion is unavoidable [46,47].

2.2.2 Moving media

Nonreciprocal devices based on nonlinearity suffers from several drawbacks. First, the working properties are generally amplitude dependent. Second, waveform distortion is always involved due to media nonlinearity. Third, to obtain large levels of transmission asymmetry the operation amplitudes need to be relatively high. And, fourth, there is possible degradation in performance when both forward and backward waves are present at the same time, a problem known in photonics as dynamic reciprocity [48], with a tradeoff between forward transmission and nonreciprocal intensity range [41]. These drawbacks have encouraged research into alternative routes to acoustic nonreciprocity.

Nonreciprocal phenomena are commonly encountered in underwater acoustics and aerodynamics, as in the case of large ocean currents or high-speed airflow. Giant nonreciprocity typically requires very high moving speeds and/or very long distances to accumulate the nonreciprocal effect. However, in 2014, by introducing biased angular momentum into a circular resonator with sharp resonance, giant acoustic isolation was achieved with a slow airflow in a subwavelength scale metamaterial [8]. The introduced angular momentum split the resonance mode for clockwise and anti-clockwise waves into two different frequencies, mimicking the Zeeman effect in quantum mechanics. Though in this setup the frequency splitting is proportional to the biased flow speed, because the resonator supported a very sharp resonance, even a tiny frequency difference could result in large sound isolation. This design was then soon applied in proposals for acoustic Chern insulators [49,50], with an experimental realization recently reported [51]. Nonreciprocal acoustic isolators based on the Mach-Zehnder interferometer have also been reported

where, by coupling two acoustic waveguides with different moving media (in reality, typically one waveguide is with static media while the other is with moving flow), one can realize constructive interference in one direction and destructive interference in the opposite direction [6,9]. Some of these designs were introduced by the author and are the subject of chapter 3.

2.2.3 Spatiotemporal modulation

While biased moving media is a good solution for sound isolation, the working bandwidth is typically narrow and the robustness to dissipation is quite weak. In addition, the moving flow will typically cause undesired additional sound, for example noise from fans which are used to create a steady flow. Moreover, the moving media approach is practically limited to fluids, which prevent its applicability in elastic wave propagation. Spatiotemporal modulation, which can mimic the effect of moving media, was subsequently proposed. By dynamically changing the effective bulk modulus of three connected resonant cavities, acoustic isolation levels of over 40 dB with insertion losses as low as 0.3 dB were seen in simulations of a noise-free, integrable, frequency scalable subwavelength device [52]. In this study, the volume of the cavities was alternately modulated in the clockwise direction, which introduces an effective angular momentum to break the reciprocity among the ports. In another example, by modulating two tightly coupled resonators inside an acoustic waveguide, an isolation factor greater than 25 dB has also been reported [53]. This approach has additionally been utilized in nonreciprocal sound transmission between two acoustic resonators [54]. Specifically, by introducing an initial spatial phase bias to the space-time modulated coupled resonators, acoustic energy could be always confined in one of the two connected resonators. All above-mentioned spatiotemporal modulations involve changes to the volumes of resonators, which is a

modulation of the effective bulk modulus. To instead achieve nonreciprocity through a time-varying effective density, a scheme has been proposed to modulate elastic membranes [55]. Using piezoelectric transducers to modulate solid media, similar nonreciprocal transmission has also been reported for elastic waves [56,57]. Another approach is mechanical modulation in nonlinear media to change the local effective stiffness [44,58].

2.2.4 Nonreciprocal bianisotropy

In regular acoustic media, momentum change is a function of acoustic velocity, and volume change is a function of acoustic pressure. Acoustic bianisotropy, also called Willis coupling, considers the coupling between acoustic pressure and velocity, resulting in momentum and volume change as functions of both acoustic pressure and velocity [59]. In Willis media, the mass conservation equation and the momentum equation can be written as [14,60–63]

$$\frac{\partial u}{\partial x} = i\omega\left(E_{eff}^{-1}p + \xi_{eff}u\right), \tag{2.6}$$

$$\frac{\partial p}{\partial x} = i\omega\left(\rho_{eff}u + \varsigma_{eff}p\right). \tag{2.7}$$

Here E_{eff} and ρ_{eff} are the effective bulk modulus and density, while ξ_{eff} and ς_{eff} are the Willis coefficients, quantifying the coupling between acoustic pressure and velocity. The dispersion relation of the above two equations is

$$k_{\pm} = \pm\frac{\omega\sqrt{\left(\xi_{eff}-\varsigma_{eff}\right)^2 + 4\rho_{eff}E_{eff}^{-1}}}{2} + \frac{\omega\left(\xi_{eff}+\varsigma_{eff}\right)}{2}. \tag{2.8}$$

The first term with plus and minus signs indicates the reciprocal portion of the wavenumber while the second term indicates the nonreciprocal portion of the wavenumber. When $\xi_{eff} \neq 0$ and $\varsigma_{eff} \neq 0$ but $\xi_{eff} + \varsigma_{eff} = 0$, the nonreciprocal portion of the wavenumber

is zero, indicating that the presence of Willis coupling does not necessarily imply that reciprocity is broken. However, when $\xi_{eff} + \varsigma_{eff} \neq 0$, Willis coupling can result in large nonreciprocity. Based on active Willis materials, broadband sound isolation has been reported in both airborne acoustics [64,65] and mechanical waves [66]. On the passive side, by modulating both elastic moduli and mass density in space and time in a wave-like fashion, nonreciprocal wave propagation has also been reported [67–69]. There is some debate about whether this method of introducing effective moving materials should be considered a passive approach, because it requires extra energy to operate the system. However, this type of modulation only converts the energy in the moving parts while leaving the acoustic energy conserved and therefore it is useful to distinguish it from modulation schemes which explicitly input acoustic energy. A nonreciprocal acoustic lens based on passive modulation of Willis coupling which only images an object from one side has also been proposed [70].

2.3 APPLICATIONS

Reciprocity is a powerful concept in the analysis, design and operation of acoustic systems. Knowing that a system obeys reciprocity implies that there are underlying symmetries that can in many cases simplify the analysis of complex systems. For instance, a complex measurement of an acoustic quantity can in many instances be substituted by a simpler one when reciprocity holds. Consider what a driver hears when operating a vehicle. How much of the total noise produced by the vehicle is due to the airborne sound generated by the tires? Answering this question directly could mean placing microphones in the ears of an artificial head in the driver's seat and then deactivating or disconnecting all other sources of sound, such as any structure-borne vibrations. This is no small feat. But the same information can be obtained through a reciprocal measurement. In this case sound sources

are instead placed in the ears of the artificial head and the resulting pressure is then measured at points on the tire surface [71]. For many years reciprocity has served as a useful tool in physical acoustics, including for calibrating microphones [72], for deriving analytical scattering solutions in the presence of a flaw [73], and for inverse parameter estimation in seismic experiments [74].

While the absence of reciprocity might make the analysis more difficult, it enables novel wave guiding phenomena, such as in the examples so far discussed. Nonreciprocity finds application in all typical acoustic wave domains: air, water, biological tissues, and solids. We discuss here in particular two areas of application that are poised to make lasting contributions in the acoustics community. The first is surface acoustic wave (SAW) devices, which are a promising platform for nonreciprocity because of their widespread industrial and research use. The second application area is topological acoustics, where nonreciprocity is tied to the time-reversal symmetry breaking that is essential to many topological effects.

2.3.1 Nonreciprocal SAWs

Waves confined to an interface between two materials are called surface waves and are characterized by an exponential decay of the wave amplitude into the materials. The lower symmetry and tighter energy confinement of surface waves relative to bulk waves have made them a promising avenue for large nonreciprocal response. In these waves the matter at the interface undergoes harmonic motion as displacement from equilibrium is counterbalanced by a restoring force. In the case of ocean waves, the displaced water at the water/air interface is restored by the gravitational force. In solid media, the dominate restoring force is the elastic resistance to deformation. Surface waves on solids are called Rayleigh waves, after Lord Rayleigh who described their existence in an 1885 paper [75].

In these waves, the solid particles undergo elliptical motion where the size of the ellipses shrinks with depth. In an isotropic solid these ellipses lie fully in the plane made by the direction of travel and the surface normal. And, in a semi-infinite elastic block, these waves are non-dispersive.

Rayleigh waves are of technological significance as they are the primary type of wave used by SAW devices. In these devices, metal electrodes launch and receive Rayleigh waves on a piezoelectric substrate. Because the Rayleigh wave speed in a typical substrate is a few thousand meters per second, the wavelengths in a SAW signal are many orders of magnitude smaller than they would be if the signal was in the form of an electromagnetic wave. The ability of SAW devices to process signals in a small volume makes them well suited as components of integrated circuits and they are consequently widely used in modern electronic systems (a typical cell phone contains dozens of SAW filters) [76,77]. SAW devices are also widely used in microfluidics, such as in the manipulation of biological matter, and are also being increasingly utilized in basic quantum research, for example as a way to controllably transmit single electrons [76]. To date these devices have been largely constrained by reciprocity. But recent effort has begun to show how this restriction might be efficiently overcome, opening even more possibilities for these microelectromechanical devices. For example, incorporating nonreciprocity could allow a single SAW device to serve dual roles as a filter and an isolator. Nonreciprocity can also help minimize the degrading effect of reflections from the substrate boundaries.

To date, the most studied technique for SAW nonreciprocity is the magnetoelastic effect. The amount of nonreciprocity achieved by the coupling of magnetic and elastic fields is dependent on the relative orientations of the applied magnetic field, the direction of wave propagation, and any special directions dictated by various symmetries of the system such as the crystal structure and material shape [78]. The first studies on surface

wave magnetic nonreciprocity were conducted decades ago, but only modest effects were demonstrated. In one early study, nonreciprocity was observed in a single-crystal aluminum block where the applied magnetic field caused the conduction electrons to undergo cyclotron orbits, influencing the elastic wave propagation nonreciprocally due to the presence of the symmetry-breaking surface. The nonreciprocity was small, and the setup needed to be kept at very low temperature (4 K) [79].

Through a recent surge of interest, devices are now being introduced that can obtain large nonreciprocal effects while at room temperature. In a remarkable demonstration, a magnetic SAW device operating at 1435 MHz was recently reported to achieve 48.4 dB of isolation, which is substantially higher than that of commercial Faraday isolators (~20 dB) in this frequency range [80]. The setup, illustrated in Fig. 2.3(a), consists of SAW waves generated on a piezoelectric $LiNbO_3$ substrate and then sent through a ferromagnetic (FeGaB) bilayer stack where resonant magnetoelastic coupling between SAW and magnetic spin waves induces large dissipation. This magnetically induced interaction is nonreciprocal and, as plotted in Fig. 2.3(b), depends on the relative angles of the anisotropy direction of the ferromagnetic layer, applied magnetic field (highest isolation was seen at ~10 Oe), and direction of SAW propagation. In another study, a similar ferromagnetic bilayer structure was found to achieve high amounts of nonreciprocity over a wide 6 GHz frequency range in simulations [81]. Nonreciprocity has also been studied in devices that use Dzyaloshinskii-Moriya interactions in a ferromagnetic/metal bilayer [82,83] and in platforms with magnetic nanowires [84,85]. Another recent approach was to achieve nonreciprocity through magneto-rotation, as illustrated in Fig. 2.3(c) [86]. SAW devices with magnetic layers have also shown promise as magnetic field sensors [87] and nonreciprocal spin wave devices [88].

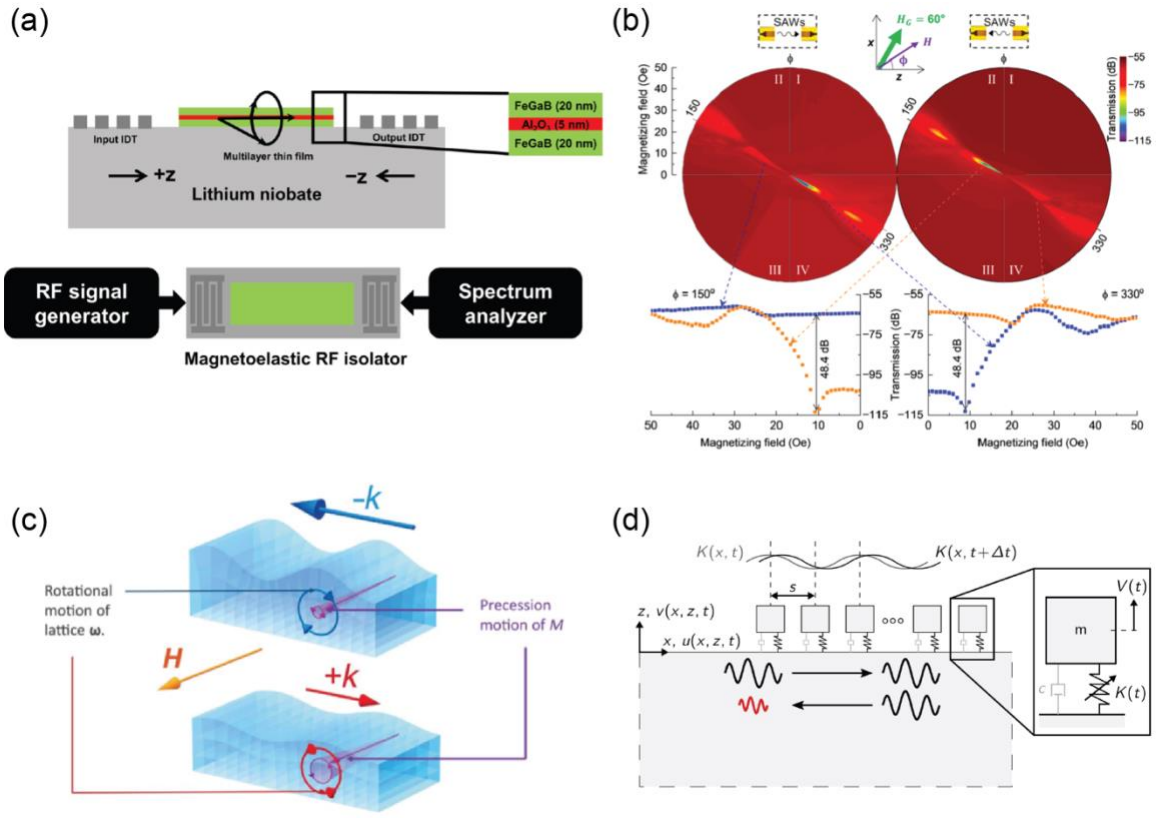

Figure 2.3: Nonreciprocal SAW devices. (a) Schematic of a magnetoelastic SAW isolator. The propagating wave is attenuated more when traveling in the reverse direction, in which case it is resonantly coupled to magnetic spin waves in the FeGaB bilayer. Shah et al., Sci. Adv. 6, eabc5648 (2020). Copyright 2020 Author(s), licensed under a Creative Commons Attribution (CC BY) license. (b) Color maps show the amount of transmission at different angles and magnitudes of external magnetic field. When the magnetic field is angled at 150° or 330° and ∼10 Oe, the device exhibits 48.4 dB of isolation. Shah et al., Sci. Adv. 6, eabc5648 (2020). Copyright 2020 Author(s), licensed under a Creative Commons Attribution (CC BY) license. (c) A magneto-rotation effect is studied as an alternative to magnetoelastic coupling to achieve magnetic nonreciprocity. Xu et al., Sci. Adv. 6, eabb1724 (2020) Copyright 2020 Author(s), licensed under a Creative Commons Attribution (CC BY) license. (d) Nonreciprocity due to spatiotemporal modulation is investigated by considering a surface loaded with an array of resonators. The modulation is a traveling wave modulation of the spring constants. Reproduced with permission from Palermo et al., J. Mech. Phys. Solids 145, 104181 (2020). Copyright 2020 Elsevier. Note that this setup is equivalent to the one shown in Ref. 70, published simultaneously.

While not yet demonstrated experimentally, spatiotemporal modulation is another feasible route to SAW nonreciprocity. A pair of papers, published simultaneously in the same journal, analyzed one possibility of this where an elastic surface is loaded with an array of masses with modulated spring constants, as shown in Fig. 2.3(d) [89,90]. Connecting SAW devices to modulating circuit components, such as switches or varactors, is another direction being pursued [91,92].

2.3.2 Topological acoustics

Nonreciprocal acoustics has also found application in the dynamic field of topological acoustics, which is the study of acoustic systems that can be characterized by quantities (topological invariants) that remain unchanged even when the system is distorted through continuous transformations. Both topological acoustics and its counterpart in electromagnetics, topological photonics, arose from pioneering work on the integer quantum Hall effect in condensed matter physics. In this effect, seen in a collection of electrons constrained to move in a plane and subject to a magnetic field which breaks the time-reversal symmetry, there are electron states that are confined to the outer surface, largely unaffected by the shape of the surface. Analogues to this effect have been shown in acoustics where time-reversal symmetry is broken through the use of a moving fluid or time modulation. If the acoustic system is then excited by a source in a suitable frequency range, the vibrations counterintuitively travel exclusively around the perimeter of the system, though the middle remains open. Figures 2.4(a) and 2.4(b) shows a realization of this effect in elastic wave propagation on a polyester plate with attached time-modulated piezoelectric disks [10]. The spatiotemporal modulation breaks time-reversal symmetry and opens topological band gaps in the system that support topologically protected modes propagating along the edges of the lattice.

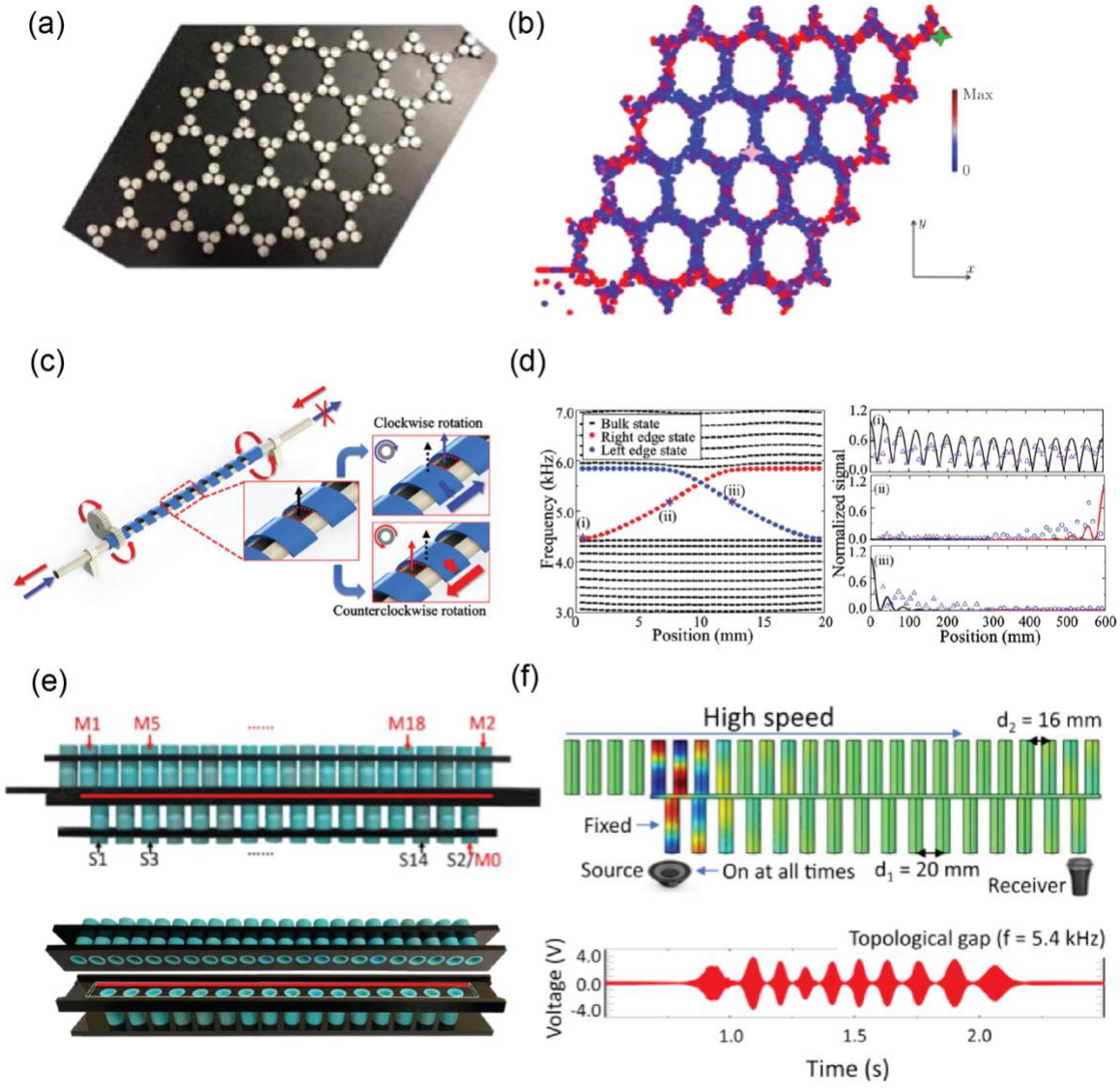
(a)
(b)
Max
0
y
x
(c)
Clockwise rotation
Counterclockwise rotation
(d)
Bulk state
Right edge state
Left edge state
Frequency (kHz)
Position (mm)
Normalized signal
Position (mm)
(e)
M1
M5
M18
M2
S1
S3
S14
S2/M0
(f)
High speed
d2 = 16 mm
Fixed
Source
On at all times
d1 = 20 mm
Receiver
Topological gap (f = 5.4 kHz)
Voltage (V)
Time (s)

Figure 2.4

Figure 2.4: Topological acoustics. (a) Photograph of mechanical Chern insulator consisting of a plate with attached piezoelectric disks. Synthetic angular momentum biasing is imparted by modulations in circuits connected to the piezoelectric disks. Darabi et al., Sci. Adv. 6, eaba8656 (2020). Copyright 2020 Author(s), licensed under a Creative Commons Attribution (CC BY) license. (b) Displacement measurements show an excitation traveling around the perimeter of the system, protected against defects by the topological order of the 2D lattice. Darabi et al., Sci. Adv. 6, eaba8656 (2020). Copyright 2020 Author(s), licensed under a Creative Commons Attribution (CC BY) license. (c) In a demonstration of topological pumping in airborne acoustics, the boundary of an acoustic waveguide is modulated by the mechanical rotation of a shaft. Sound is topologically transported through the waveguide when incident from the right end, but largely blocked when incident from the left end. Reproduced with permission from Xu et al., Phys. Rev. Lett. 125, 253901 (2020). Copyright 2020 American Physical Society. (d) Left: The eigenfrequency evolution as a function of the crank angle over a complete cycle. Right: The normalized pressure in the waveguide at points (i)–(iii). Solid lines are theoretical results; markers show the experimental results. Energy supplied to the right end feeds the right localized mode, crosses the bulk, and ends up in the edge state on the opposite side after the pump cycle is completed. Reproduced with permission from Xu et al., Phys. Rev. Lett. 125, 253901 (2020). Copyright 2020 American Physical Society. (e) In another demonstration of topological pumping, two arrays of hollow cylinders are connected by a narrow central channel. Reciprocity is broken by the system as the top cylinder array is continuously translated. Reproduced with permission from Cheng et al., Phys. Rev. Lett. 125, 224301 (2020). Copyright 2020 American Physical Society. (f) A source injects energy into the left edge of the bottom array. The time trace shows the response at the receiver on the right end, where signal is repeatedly picked up each time the system goes through a complete pumping cycle. Reproduced with permission from Cheng et al., Phys. Rev. Lett. 125, 224301 (2020). Copyright 2020 American Physical Society.

Topological effects also arise in passive systems that obey reciprocity, such as the acoustic counterparts of the spin Hall and valley Hall effects. These phenomena are interesting as they exhibit robust propagation effects similar to the integer Hall effect without the need to break time-reversal symmetry, although this means that they are often more susceptible to breakdown due to perturbations that break the needed spatial symmetries in the system.

An exciting recent development has been the experimental demonstration of topological pumping, where an edge state is adiabatically carried through the bulk to the opposite edge. Using a motorized crank to rotate a helical waveguide boundary as shown in Fig. 2.4(c), researchers transported an acoustic wave from one end to the other of a waveguide using topological pumping [93]. The energy is transported from one end of the system to the other as the modal structure evolves from being localized at the right end to being localized at the left end [Fig. 2.4(d)]. As the pumping is topological, it is robust to perturbations. This is a clearly a nonreciprocal result, and energy sent in from one direction is not equivalently carried back in the opposite direction. One limitation of topological pumping is that the transfer of the localized states must occur slowly enough for the adiabatic condition to apply. The speed of the topological energy transfer from one edge state to another can be increased by exploring more complex modulations of couplings, as examined recently with optimal control methods [94]. Further progress can be made by tapping into the rich literature on shortcuts to adiabaticity [95].

An exciting recent development has been the experimental demonstration of topological pumping, where an edge state is adiabatically carried through the bulk to the opposite edge. Using a motorized crank to rotate a helical waveguide boundary as shown in Fig. 2.4(c), researchers transported an acoustic wave from one end to the other of a waveguide using topological pumping [93]. The energy is transported from one end of the

system to the other as the modal structure evolves from being localized at the right end to being localized at the left end [Fig. 2.4(d)]. As the pumping is topological, it is robust to perturbations. This is a clearly a nonreciprocal result, and energy sent in from one direction is not equivalently carried back in the opposite direction. One limitation of topological pumping is that the transfer of the localized states must occur slowly enough for the adiabatic condition to apply. The speed of the topological energy transfer from one edge state to another can be increased by exploring more complex modulations of couplings, as examined recently with optimal control methods [94]. Further progress can be made by tapping into the rich literature on shortcuts to adiabaticity [95].

Topological acoustics is a currently a highly active area of inquiry with new phenomena being demonstrated almost weekly. By no means exhaustive, a list of other nonreciprocal topological advances described in recent articles includes a hybrid integer / valley Hall acoustic effect [12], particle pulling using topological chiral modes [11], feedback control as a versatile platform for topological effects [96], and observation of bulk-edge correspondence in a non-Hermitian active mechanical system [97].

2.4 DISCUSSION AND OUTLOOK

Nonreciprocity in acoustic wave propagation is useful because it dampens the effect of obstacles. Vibrations can travel to an intended destination in spite of perturbations that would otherwise impede their progress. For example, the inclusion of an isolator as part of an acoustic signal chain guarantees that no signal will be reflected back to the source, regardless of what comes after it in the signal chain. And a device with a topologically protected edge mode ensures one-way acoustic propagation even through convoluted material interfaces. This simplifies the design of complete acoustic systems, because it introduces extra latitude in the design – many designs can have the same functionality.

What ingredients are required to violate reciprocity is well understood. But there is still substantial work to be done in developing the most effective nonreciprocity recipes for various applications. A feel for this large variation in potential applications can be obtained by considering three common scenarios of engineered acoustic propagation and the frequency ranges involved. First, airborne acoustics, where most devices deal with frequencies that fall in the range of human hearing (20 to 20 000 Hz), though higher frequencies are also routinely utilized in devices such as ultrasonic vehicle detectors. Second, biomedical ultrasound, where vibrations travelling through complex biological tissue fall in the 2 to 15 MHz range for diagnostic imaging and 0.25 to 2 MHz for high-intensity heating or ablating of tissue. And third, underwater sonar, where common working frequencies cover a range from about 1 kilohertz to a megahertz. The large range of length scales and material properties at play in applied acoustics indicates that a diverse range of strategies for efficient nonreciprocal phenomena is needed. In this regard it can be useful to consider which nonreciprocity techniques have or have not yet been applied in different acoustic wave platforms. Examples of these combinations are shown in Fig. 2.5. Ideas for future work can be found by considering combinations of techniques mentioned in the top row, representing different mechanisms to achieve nonreciprocity paired with the acoustic platforms mentioned in the lower row. The arrows indicate combinations that have been already at least partially explored, but several others remain to be explored.

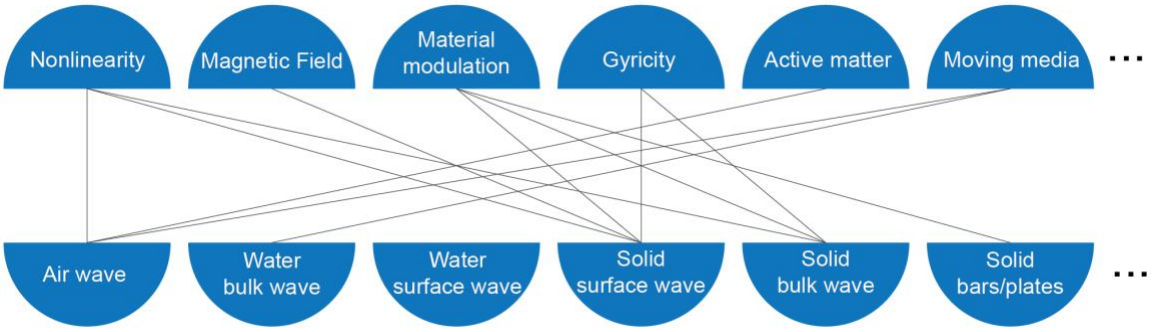

Figure 2.5: Acoustic nonreciprocity combinations. Top row: mechanisms to achieve nonreciprocity. Bottom row: example acoustic wave platforms. By exploring the different combinations, researchers have the opportunity to further widen the scope of acoustic nonreciprocity. Links illustrate a few combinations that have been explored at least to a certain extent.

Aside from the study of techniques to break reciprocity, a field that will continue to be studied in its own right, nonreciprocal components will continue to find place in demonstrations of novel acoustic phenomena. An example of this is seen in acoustic arrays, used widely for beamforming in sonar communications and biomedical imaging, where the breaking of reciprocity means that the reception and transmission can be independently tuned. Initial studies have numerically studied how this might be accomplished [6,7], but experimental demonstrations are still lacking. There is also work to be done with nonreciprocal acoustic metasurfaces. Breaking reciprocity and time-reversal symmetry for a surface breaks the constraint that the reflection and transmission coefficients are equivalent between a pair of incidence angles. That is, breaking reciprocity and time-reversibility allows $R_{\theta_1\to\theta_2} \neq R_{\theta_2\to\theta_1}$ and $T_{\theta_1\to\theta_2} \neq T_{\theta_2\to\theta_1}$, opening new degrees of freedom for transmissive and reflective surfaces [98].

As highlighted above, two application areas with high potential for further investigation in this context are SAW devices and topological acoustics. While nonreciprocal SAW devices based on magnetoelastic coupling have received extensive

recent attention, further work could develop nonreciprocal SAW devices based on nonlinearity, building on established nonlinear SAW theory [99,100]. Even within the magnetoelastic paradigm, there is much left to explore in terms of heterostructure composition and theoretical descriptions of the complex spin/elastic wave interactions in these structures. It would also be instructive to consider the topological features of unidirectional SAW devices. The current wave of discoveries in topological acoustics will certainly continue forward. In addition, though topological effects can arise in reciprocal systems, the much larger degree of robustness given to these systems by nonreciprocity implies that methods to break reciprocity will continue to remain pertinent and important for this field. One promising direction is pursuing time modulation as a synthetic spatial dimension to realize higher-dimensional topological effects in lower spatial dimensionalities. Another possibility going forward is using nonreciprocity techniques to break time-reversal symmetry in order to create new forms of acoustic Weyl semimetals, which have been realized so far only through the breaking of inversion symmetries [101–103]. Nonlinear topological phenomena, such as topological phase transitions triggered by the intensity of the input signal, have also been recently discussed [104,105], on the model of their electromagnetic counterparts [106,107], but much of the potential of nonlinear topological acoustics remains untapped.

The study of nonreciprocity also intersects with research in out-of-equilibrium systems, such as active matter, where the constituent particles of the wave-bearing materials have internal sources of energy. This includes the study of the nonreciprocal wave dynamics in everything from flocking birds to biological swimmers and colloidal spinners [108,109]. Continued study of such nonreciprocal systems will lead to demonstrations of novel nonreciprocal physics and provide more insight into the complex emergent behavior frequently observed in these systems. Platforms allowing precise

control over particle couplings, such as electromechanical devices attached to programmable microcontrollers [96,110], are a promising way to demonstrate new wave phenomena. In general, as the speeds involved in wave propagation in mechanical and acoustical systems are much smaller than in other wave physics domains and as the scales are often conveniently macroscopic, they are an attractive realm for demonstrating increasingly complex nonreciprocal wave phenomena.

In this chapter we have discussed the fundamental principles of acoustic reciprocity and explained its relationship with time-reversal symmetry. While various other forms of reciprocity in fluid dynamics [111] and elastodynamics [112] exist, we have reviewed as examples reciprocity relations for simple sources in an acoustic medium. We have shown how, by breaking the underlying assumptions of reciprocity, there are a number of opportunities for breaking acoustic reciprocity and pointed out recent experimental demonstrations of these techniques. Research in acoustic nonreciprocity is now mature to the point that applications are possible as we have shown through our discussion of nonreciprocal SAW devices and topological acoustics. We have also highlighted the many other possibilities for further investigation.

Physical symmetries are transformations that leave a system unchanged and offer powerful frameworks for understanding a wide variety of phenomena. Reciprocity is a symmetry in that it is a transformation that interchanges sources and receivers while leaving certain field quantities unchanged. Much like other symmetries, it offers a simplifying view of a number of related phenomena. The study of this symmetry, how to break it, and how it can be harnessed to control acoustic fields, is a rich endeavor that will continue to inspire new research for many years to come.

Chapter 3: Nonreciprocal acoustic propagation and leaky-wave radiation in a waveguide with flow[2]

We now examine a few specific implementations of broken time-reversal symmetry in creating acoustic devices with unidirectional functionalities. These devices depend on material flow to break the time-reversibility and include spatial asymmetries to additionally violate reciprocity.

Isolators, devices with unidirectional wave transmission, are integral components in computing networks, enabling a one-way division of a large system into independent subunits. Isolators are created by breaking the inversion symmetry between a source and a receiver, known as reciprocity. In acoustics, a steady flow of the background medium in which sound travels can break reciprocity, but significant isolation is typically achieved only for large, often impractical speeds. In this work, we propose acoustic isolator designs enabled by duct flow that do not require large flow velocities. A basic isolator design is simulated based on the acoustic analogue of a Mach-Zehnder interferometer, with monomodal entry and exit ports. The simulated device footprint is then reduced by using bimodal ports. Further, a nonuniform velocity profile combined with a grating to induce phononic transitions is considered, which, combined with filters, can provide significant isolation. By coupling a waveguide with flow to free space through an array of small apertures, largely nonreciprocal leaky-wave radiation is demonstrated, breaking the symmetry between reception and transmission patterns of an acoustic linear aperture array. These investigations open interesting pathways towards efficient acoustic isolation, which

[2] Reprinted with permission from C. P. Wiederhold, D. L. Sounas, and A. Alù, Nonreciprocal acoustic propagation and leaky-wave radiation in a waveguide with flow, J. Acoust. Soc. Am. **146**, 802 (2019). Copyright 2019, Acoustical Society of America. Note that author's name changed from C. P. Wiederhold to C. Rasmussen in 2019.

may be translated into integrated acoustic and surface acoustic waves, as well as phononic technology.

3.1 INTRODUCTION

Reciprocity in sound propagation is the principle for which the same transmission signal is expected when source and receiver switch places. In a multi-port system, this implies that the scattering matrix of a reciprocal system is inherently symmetric [113,114], i.e., the acoustic signal transmitted from one port to a second one is identical to the signal transmitted from the second to the first when all other ports are impedance matched. Recent interest in acoustic and elastodynamic devices that break reciprocity has been driven by their applicability in several practical situations, including in sonar and ultrasound technology, or for full-duplex acoustic communications, in which asymmetric transmission or routing of signals to different portions of a transmit-receive module are desirable [82,115–118]. In a multi-port system nonreciprocity provides protection from arbitrary backscatter from the loads, which can protect sensitive equipment and allows components to be added in a modular fashion. In antenna theory, reciprocity requires that an emitter's reception pattern is always identical to its transmission pattern, for all angles. By breaking this reciprocity, an antenna can transmit more than it receives which shields it from echoes. Electromagnetic radiators with this broken reciprocity have been studied and fabricated, with applications including thermal management [119,120]. Reciprocity breaking is also integral to the study of topological acoustics, where it gives rise to unidirectional topological modes that can propagate in a crystal lattice immune to defects and disorder [49,121–125].

It is known that a steady fluid flow is a simple avenue to break reciprocity for sound [117,126], and recent work has shown how adding a slow material flow to a resonant device

can make it, under a suitable design, highly nonreciprocal [8]. In the following, we describe the operation, design, and performance of innovative acoustic isolators not based on resonant cavities. The first isolator design, an acoustic Mach-Zehnder interferometer, consists of a single mode duct split into two paths and later recombined. By exploiting the directional interference between these paths it is possible to realize an efficient isolator. A more compact version of this isolator is then explored, at the expense of using bimodal input and output waveguides. We then also use bimodal ducts with a nonuniform velocity profile and a grating to induce a phononic transition. To conclude we consider how simple duct flow may also realize non-reciprocal leaky-wave radiation for sound.

3.2 BREAKING RECIPROCITY USING FLOW

Reciprocity in acoustics is inherently rooted in the linearity and time-reversal symmetry of the wave equation, which in the time harmonic regime using the $e^{-i\omega t}$ convention reads [5]:

$$\nabla^2 p + \left(\frac{\omega}{c}\right)^2 \left(1 + \frac{i}{\omega}\vec{v}\cdot\nabla\right)^2 p = 0, \tag{3.1}$$

where p is the acoustic pressure, ω the angular frequency, c the small-signal speed of sound, i the imaginary unit, and $\vec{v}$ the time-invariant velocity field. Consider two sourceless time-harmonic fields, p_1 and p_2, each satisfying this equation. Multiplying the wave equation for p_1 by p_2 and subtracting the result from the wave equation for p_2 multiplied by p_1 gives

$$\nabla\cdot\left(p_2\nabla p_1 - p_1\nabla p_2\right) = \frac{1}{c^2}\left[p_2\left(i\omega - \vec{v}\cdot\nabla\right)^2 p_1 - p_1\left(i\omega - \vec{v}\cdot\nabla\right)^2 p_2\right]. \tag{3.2}$$

In the case of no flow the right-hand side of this equation vanishes leaving a reciprocity relationship between fields 1 and 2. But, as the equation demonstrates, a reciprocity relationship is not guaranteed when a steady flow is present.

Reciprocity is a result of the time-reversibility of the fluid dynamics. The propagation of acoustic waves is underpinned by time-symmetric equations of classical mechanics and should exhibit reciprocity when all the relevant field quantities are transformed appropriately in time. The velocity vector field, $\vec{v}$, representing the underlying motion of the fluid particles in steady flow, flips sign under the time reversal operation, *T*. When this odd vector is not flipped between fields 1 and 2, the conditions for *T* are not fully satisfied, and nonreciprocity is possible. A challenge of this way of breaking reciprocity is that the required flow velocity should be large compared to the group velocity of sound for the effects to be large.

It is also possible to break reciprocity using nonlinear techniques [30–33,127], but nonreciprocity becomes then a function of the input intensity and does not allow for simultaneous excitation from multiple ports. The magnetic field, an odd vector field, can also be used to break reciprocity, as in magnetoelastic coupling [82,115], but these phenomena tend to be very weak in natural materials. At first glance it would seem that reciprocity would also not hold in the presence of loss when, under *T*, material absorption is not transformed into gain. But reciprocity is described in terms of ratio of field quantities, such as the ratio of the transmitted vs incident powers. In this case, if the loss is maintained as loss in the reciprocal condition, the wave is attenuated when propagating in either direction and these ratios remain unchanged [28], though there is the possibility of still breaking reciprocity if the loss is direction dependent [128]. In the following, we explore how to engineer acoustic devices to take advantage of small medium flows to realize large nonreciprocal effects.

3.3 WAVEGUIDE WITH UNIFORM FLOW

In a rigid walled waveguide with transversely uniform flow, the phase velocity of a sound wave in the direction of the fluid flow differs from the sound speed according to $c_{ph} = c + \vec{v} \cdot \hat{k}$, where $\hat{k}$ is the wavevector direction. For the waveguide's plane wave mode, this means that it travels faster or slower by an amount $v = |\vec{v}|$ depending on whether it is propagating with or against the direction of flow. Higher-order modes, described as the superposition of waves reflecting off the sides of the duct at an angle θ, have their phase speed along the waveguide axis increased or decreased by $v\cos\theta$.

The dispersion relation in a waveguide with uniform flow along the *x*-axis and no *z*-component of the wavenumber is, from Eq. (3.1),

$$k_x^2 + k_y^2 = \left(\frac{\omega}{c} \mp \frac{v}{c} k_x \right)^2 . \tag{3.3}$$

For the plane wave mode, with $k_y = 0$, the group velocity, $\partial\omega/\partial k$, is increased or decreased by v. On a band diagram, this modification appears as a change of the slope of the plane wave line, which extends to zero frequency (Fig. 3.1). For higher-order modes the behavior is simplified when the Mach number, v/c, is small. In this regime, the wavenumber of all modes is increased or decreased by $v\omega/c^2$. The flow creates an asymmetry in the dispersion diagram about the frequency axis. This asymmetry can be quantified by the nonreciprocal phase shift, $\Delta\beta = |\beta_p| - |\beta_m|$, the difference in the real part of the wavenumber along the waveguide axis, k_x, between a forward and a backward propagating wave. At low Mach numbers the phase difference is approximately equivalent in the forward and backward directions and it is linear with the fluid velocity, $\Delta\beta = 2\delta\beta = 2v\omega/c^2$, with $\delta\beta$ being the wavenumber shift due to fluid flow. It is this nonzero nonreciprocal phase shift that can be exploited to create a sound isolator.

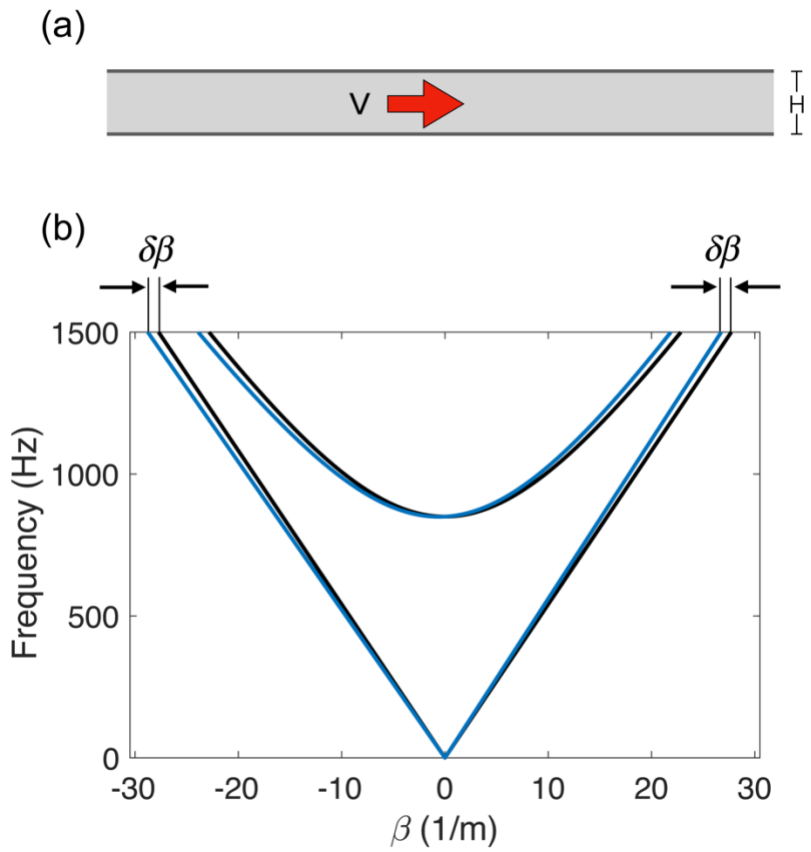

Figure 3.1: (a) Diagram of waveguide with uniform flow. (b) Band diagram of propagating waveguide modes when the waveguide height H is 0.2m and the operating frequency is 1500 Hz for 0 (black) and 12.4 m/s (blue) flow velocity. The nonreciprocal phase shift is approximately $2\delta\beta$ for a low Mach number flow.

3.4 Acoustic Isolators

3.4.1 Background

An isolator is a two-port device that allows large transmission in one direction while blocking backscattered waves [34]. A wave entering the device through an input port, say port 1, is transmitted out the exit port, port 2, while a wave coming from port 2 is blocked

from exiting either port 1 or 2. Such a device clearly breaks reciprocity and linearity and passivity require that it includes loss, meaning its scattering matrix is inherently non-symmetric and non-unitary. Reciprocity must be broken because, if left intact, large transmission through the device from port 1 to port 2 necessarily implies large transmission through the device from port 2 to port 1. And there must be a mechanism for loss because without loss the scattering matrix being unitary allows only non-reciprocity in the phase but not in the amplitude. The loss can come from cumulative effects, such as thermoviscous attenuation, or by including additional ports that collect the energy incident from port 2. A three-port device that breaks reciprocity, called a circulator, was recently demonstrated in acoustics using moderate flow in a circular resonant cavity [8]. The small $\delta\beta$ induced in the cavity was largely amplified by its resonance, implying a trade-off between bandwidth and flow velocity. A circulator can function as an isolator when one of the ports is terminated with a matched impedance, such as a wave absorbing anechoic wedge. The unused port provides the loss required by the isolator.

3.4.2 Nonreciprocal Mach-Zehnder isolator

A Mach-Zehnder interferometer is a device that splits a monochromatic beam of light in two and recombines the beams after they travel down separated paths [129,130]. The amount of interference, constructive or destructive, at the point where the beams are recombined indicates the phase difference accumulated by the beams on their individual paths. To work as an isolator, an interferometer additionally needs the two essential features of an isolator: broken reciprocity and loss. Reciprocity is broken by embedding nonreciprocal phase shifters in the two arms of the Mach-Zehnder interferometer. These are the areas where the phase of the beam advances more in one direction than in the reverse direction. In electromagnetic Mach-Zehnder isolators, nonreciprocal phase shifters are

implemented using magnetic materials [131,132] or suitably modulated material properties [133,134]. In our proposed acoustic Mach-Zehnder interferometer (Fig. 3.2), the nonreciprocal phase shifters are areas of flow. In these waveguide sections the phase of a propagating sound wave advances more when travelling in the direction of flow than when travelling against it. The loss comes from extra ports included above and below the input and output ports. Sound incident from port 2 exits the system through these ports terminated with impedances matched to the waveguide impedance.

Beam splitting in our proposed acoustic Mach-Zehnder interferometer is accomplished using a multimode interference coupler, a type of beam splitter found in optics [135]. It operates by decomposing the incident energy into many transverse modes. Output ports are placed on the other side of the splitter at locations where the modal interference pattern has high field strength so that ideally all of the input energy is equally split into the two output paths. In our design, a sound wave enters the system in the dominant mode (plane-wave like) from port 1 at a frequency below the cutoff of any higher-order modes. It enters the beam splitter where, because the input to the cavity is along the centerline, the interference pattern of the modes is transversely symmetric. By optimizing the length of the cavity and placing the two cavity outputs equidistant from the centerline, the sound is split equally into the upper and lower paths. The phase at the entrance to these two paths is also equal. The two separated waves traverse their individual paths before being recombined with another identical beam splitter on the output (right) side of the device. If the waves from the two paths have the same phase when they reach the second beam splitter, they excite the symmetric mode of the cavity and the wave predominantly gets out through the center waveguide. On the other hand, if they have a phase difference of 180 degrees, the antisymmetric mode is excited and there is no output power at the center waveguide, since this mode has a zero at the location of this waveguide.

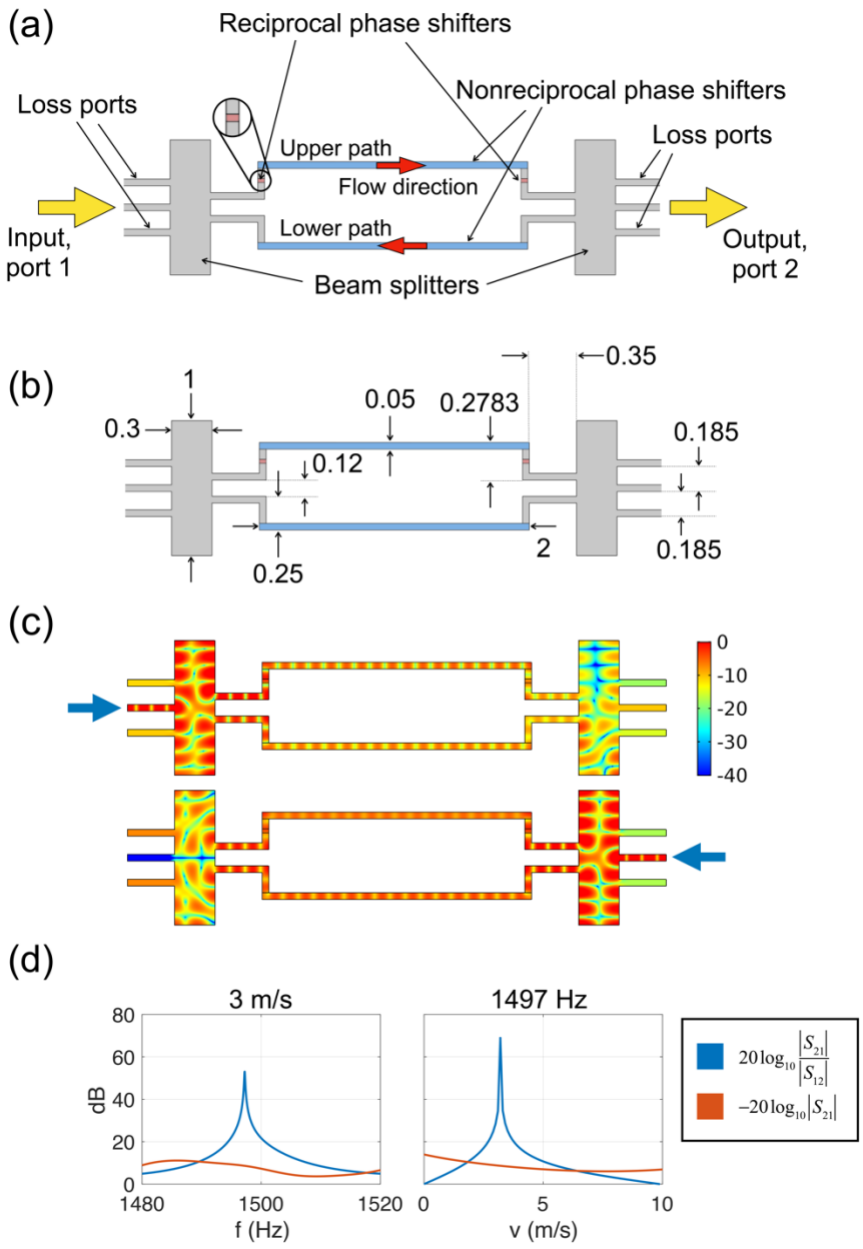

Figure 3.2: (a) Schematic of nonreciprocal acoustic Mach-Zehnder isolator. (b) Dimensions of isolator given in meters. All waveguides are equal in height. The geometry is left/right symmetric. (c) Normalized sound pressure level in decibels when the flow velocity is 3 m/s, frequency is 1497 Hz, and the wave enters from the left/right. (d) Isolation and insertion loss as a function of frequency when the flow velocity is 3 m/s, and as a function of flow velocity when the frequency is 1497 Hz.

For any other phase difference between the two waveguides, the output power is between these two extreme cases. The intensity of the wave exiting the output port is then dependent on the difference between the phase length of the upper path versus the lower path.

In order to break reciprocity, it is also necessary to break the vertical symmetry of the device. Reciprocal phase shifting areas serve this purpose. Their necessity can be seen by considering a horizontal and vertical reflection of the geometry without them. The transformation from these two reflections returns the same device geometry even though the input and output ports are now flipped. The result is that transmission from port 1 to port 2 is the same as from port 2 to port 1. It is possible to break the symmetry between the two paths, and thus break reciprocity, by putting flow in just one of the two paths, negating the need for the reciprocal phase shifting segments. But this then requires a higher rate of flow. An alternative way is to add reciprocal phase shifters to one of the paths, which is what we do here (upper path in Fig. 3.2). The reciprocal phase shifting segments in this case are simply extra duct length. The physical length of the upper path is then slightly longer than that of the lower path.

The device is modelled as a slab with acoustically hard walls. A wave entering the device from port 1 (input port, on left) ideally passes through the device and exits port 2 (output port, on right). But a wave incident from port 2 ideally neither exits port 1 nor is reflected back out port 2. It instead exits the system through one of extra ports included above and below the input and output ports. These extra ports are needed for it to function as an isolator since the acoustic medium and waveguide walls are assumed lossless. In the upper path the wave travels in the same direction as the material flow and in the lower path against the flow, producing a nonreciprocal phase response at the other end. The length is chosen to achieve a nonreciprocal phase difference of $-\pi/2$ between the two paths for propagation in the forward direction. The included reciprocal phase shifters make the upper

path slightly longer than the lower path, yielding a $\pi/2$ reciprocal phase difference between them. In the forward direction these two phase differences cancel out, and the waves constructively interfere at the beam splitter on the right side, giving large transmission to port 2. When a plane wave instead enters the device from the right (port 2), the reciprocal phase difference is still $\pi/2$, but the nonreciprocal phase difference is now also $\pi/2$. The beams arrive at the left beam splitter out of phase and therefore destructively interfere. There is an interference null where port 1 branches off the beam splitter and interference maxima at the loss ports, where most of the energy exits the system. The interference can also be explained in terms of asymmetric wave speeds. In the forward direction, the wave in the upper path travels faster than in the lower path, because it is in the same direction as the flow. But the upper path wave also has to travel a longer distance because of the extra duct sections (the reciprocal phase shifters). The longer distance and faster speed cancel, and the upper path wave arrives in phase with the lower path wave for constructive interference at the point of recombination. In the reverse direction, the upper path wave has to both travel further and at a speed reduced by the flow. It arrives out of phase with the lower path wave and destructively interferes.

Isolation is given by $20\log\left|S_{21}/S_{12}\right|$ where the scattering parameter S_{ij} is the ratio of the field exiting the system through port *i* to the field entering the system from port *j*. Using the finite element software COMSOL Multiphysics we see that the peak isolation is 69 dB with a modest flow velocity of 3.2 m/s at an operating frequency of 1497 Hz. The nonreciprocal phase difference of $-\pi/2$ requires that $l\Delta\beta = \pi/2$, where l is the length of the flow region. Using the relation between $\Delta\beta$ and v for the plane wave mode predicts a needed flow velocity of 4.8 m/s. This prediction is based on the isolator being an idealized Mach-Zehnder. The duct corners and imperfect multimode beam splitters cause it to deviate from this ideal model, as they add reactive loads to the system, reducing the

required flow velocity. However, there is still a similar tradeoff between required flow rate and length of the flow region. The total footprint of the device is roughly 4 x 18 λ at the operating frequency, with the smallest dimension being the height of the ducts.

While developed in two dimensions for conceptual simplicity, this design can naturally be extended to three dimensions, as the plane wave mode has no out-of-plane wavevector component. But the fields inside the cavities are not propagating plane waves, so the locations of the adjoining ducts need to be chosen appropriately to get the desired energy splitting. Membranes could be used to contain flow in the desired regions. With no tension applied, such membranes have a response dictated by the bending stiffness, and can present small impedance under proper conditions [5,136]. Air flow could enter the device through regions that present a high impedance to the passing acoustic waves. Helmholtz resonators, quarter wave resonators, or subwavelength metamaterials could be used to this end [137]. The flow in the device is shown as unidirectional, but could be part of a flow system that loops back on in a region external to the device.

3.4.3 Parallel isolator

An improved isolator design that reduces the required footprint can be obtained by considering two transverse modes at the input and output waveguides (Fig. 3.3). An incoming plane wave from the input port is split into two by a hard wall, modelled as perfectly thin, that runs down the middle of the waveguide. The upper beam encounters a side cavity, which reciprocally shifts its phase relative to the lower beam. The other necessary component of our isolator, a nonreciprocal phase shift, again comes from flow regions. As the separating wall ends, the beams are recombined in phase, and a plane wave is transmitted through the output port. If instead the system is excited from the right, an incoming plane wave is split into two paths which are out of phase at the point of

recombination because of the nonreciprocal phase shift. Since the waveguide supports an odd second-order mode, instead of being reflected back the two signals efficiently couple to the odd mode, which then propagates away from the device through the input port.

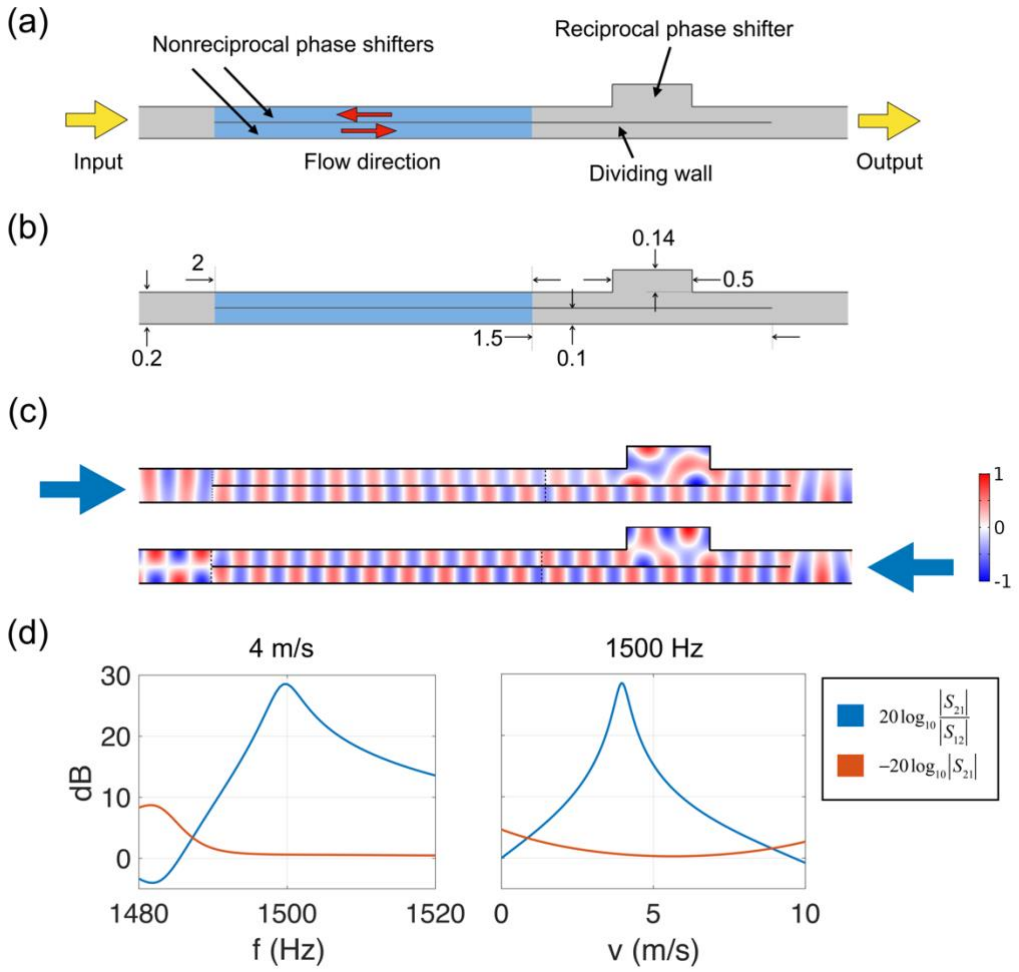

Figure 3.3: (a) Schematic of isolator with parallel flow-biased waveguides. (b) Dimensions of isolator given in meters. (c) Normalized pressure amplitude when the flow velocity is 4 m/s, frequency is 1500 Hz, and a plane wave is incident from the left/right. (d) Isolation and insertion loss versus frequency when the flow velocity is 4 m/s, and versus flow velocity when the frequency is 1500 Hz.

Using this device in combination with mode filters at the entrance and exit to absorb the odd mode completes the isolating behavior. From the left, an input plane wave passes through the device with high transmission, but if the same plane wave enters the device from the right is converted to the odd mode and absorbed by the filter on the left, implying large nonreciprocity and isolation. The device peak isolation is 29 dB, with a lower insertion loss than the first design. The required flow velocity is roughly 4 m/s with a device footprint of 2 x 15 λ at the optimal frequency.

3.4.4 Phononic transition isolator

Spatiotemporal modulation in wave-carrying media can induce transitions to other modes of the system with a resultant change in frequency and wavenumber [138]. This mode conversion is known in optics as a photonic transition, in analogy to quantum electronic transitions in solid state physics. For example, an electromagnetic wave travelling in a silicon waveguide can be transitioned from one mode of propagation, say mode 1, to another, say mode 2. The transition takes place as the wave travels through a region where the material property is modulated with a travelling wave perturbation of the form $\cos(\Delta\omega t - \Delta k z)$ where t is time, the z-direction is along the waveguide axis, and $\Delta\omega$ and Δk are the frequency and wavenumber difference between modes 1 and 2. The amplitudes of modes 1 and 2 oscillate in the modulated region whose length is chosen so that only mode 2 is present at its end. Full oscillations between modes 1 to 2 are possible, and the small modulation lends the problem to an analytical treatment using perturbation theory. When a wave is instead incident as mode 1 from the opposite side, very little mode conversion takes place and it remains in mode 1 form. This happens because the incident wave is now travelling in the direction opposite to that of the material property perturbation, so the mode matching condition is no longer satisfied. The total effect is large

nonreciprocal mode conversion. When the system is combined with appropriate filters, the phenomenon is used to create highly-nonreciprocal linear isolators for light [39,139].

In acoustics, fluid flow modifies the phase speed for passing waves and can be used to induce transitions between modes. However, a travelling wave perturbation of the velocity field is difficult to achieve as the background fluid flow is not governed by a wave equation. If instead steady flow is used, nonreciprocal mode conversion is still possible, but extra features are needed to make the effect large and the analysis is not as straightforward. Time-invariant flow implies that mode conversion can only occur between modes of the same frequency. The system in this case is governed by the convected wave equation [Eq. (3.3)] where there is no mechanism for frequency conversion.

Full-wave simulations are relied on to optimize the setup (Fig. 3.4), with guidelines taken from the perturbation analysis of photonic transitions. For one, optimal coupling between modes come from maximizing their overlap integral in the presence of the flow, $\int v P_0 P_1$, integrated over the waveguide cross section in the flow region. In our case, P_0 is the profile of the plane wave mode – a constant. P_1 is the profile of the first higher-order mode, given by the cosine function. To maximize the integral with these modal profiles, the velocity function v should be anti-symmetric over the waveguide cross-section. Limiting the flow profile to a single speed and only pointed in the forward direction, the integral is maximized when the flow covers half the waveguide height [Fig. 3.4(a)].

Nonreciprocal mode conversion is now possible, but a large velocity is still needed for good performance. This requirement can be relaxed by introducing a grating to provide a *z*-directed modulation, analogous to the Δk modulation in a photonic transition. The Δk difference between the two waveguide modes predicts a notch spacing of $5.7\,\lambda$, close to the optimal result, $5.9\,\lambda$, obtained from simulations. Unlike the case for photonic transitions, there is still considerable mode oscillation that occurs when a wave passes

through the system in the backwards direction. Modal oscillations occur in both directions, but with different periodicities. The length of the flow region is chosen to enhance the nonreciprocal response. Ideally, a plane wave mode incident from the left oscillates until it exits the system out the right as a plane wave mode. But a plane wave mode incident from the right oscillates in that same distance to the higher order mode, exiting the system on the left.

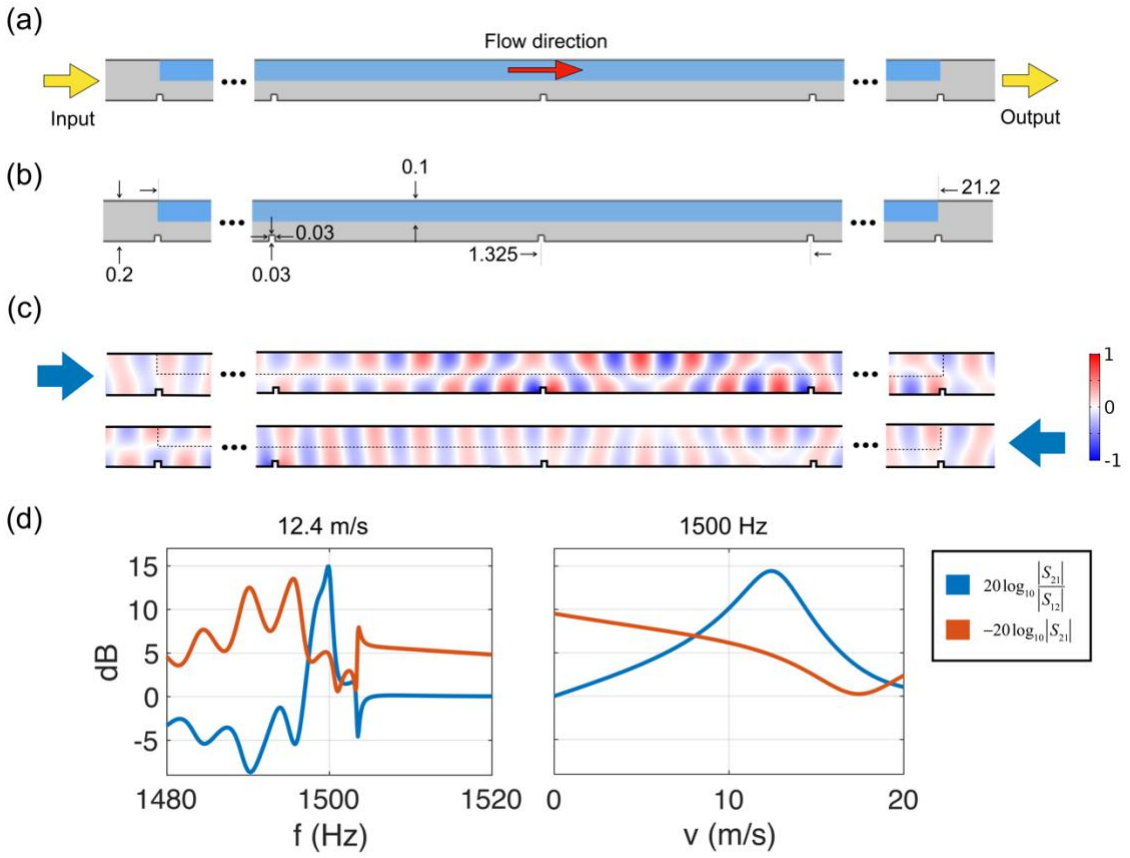

Figure 3.4: (a) Schematic of the phononic transition isolator. (b) Dimensions of isolator given in meters. (c) Normalized pressure amplitude when the flow velocity is 12.4 m/s, frequency is 1500 Hz, and plane wave mode is incident from the left/right. (d) Isolation and insertion loss versus frequency when the flow velocity is 12.4 m/s, and versus flow velocity when the frequency is 1500 Hz.

In the geometry presented here, whether from the right or left, an incident plane wave exits the system on the other side as a linear combination of the two modes, but the weight of each mode is asymmetric in the forward and backward directions [Fig. 3.4(b)]. In practice, mode filters on either side would remove the second mode. The isolation is then given as the ratio between how much of the plane wave mode makes it through the device when entering from the left versus the right. The phononic transition waveguide provides 15 dB of isolation at a flow velocity of 12.4 m/s when its length is ~100 λ (17 grating notches).

3.5 NONRECIPROCAL LEAKY-WAVE ANTENNA

We use broken reciprocity from flow to create a nonreciprocal leaky-wave antenna (Fig. 3.5). Flow fills the full waveguide height. The waveguide is coupled to free space by shunts and is terminated on the right with a matched absorber. The free space background is modelled as a semi-infinite medium with a hard boundary condition in the plane on top of the antenna. As expected from reciprocity, in the absence of flow reception and transmission patterns are equivalent [Fig. 3.5(b), left]. But when flow is added, a large asymmetry between the beampatterns arises. The behavior can be understood by looking at the dispersion lines for the lower order (plane wave like) mode in Fig. 3.1(b), with the blue lines representing the waveguide modes in the flow region and the free space sound cone lying on the lower black line (equivalent to the plane wave dispersion). In transmission, the wave travels in the direction of flow which increases its phase velocity, reducing the wavenumber so the blue line on the right side is within the sound cone. The wavenumber is shifted outside the sound cone in the reverse direction. The transmit beampattern is effectively rotated counterclockwise by including flow while the receive pattern is rotated clockwise. The angle of rotation can be estimated from the simple

waveguide with flow by $\cos^{-1}\left(\left(1+v/c\right)^{-1}\right)$, which for a 12.4 m/s flow, is 15 degrees. In the main emission direction, the receive sensitivity is over 10 dB smaller. The effect relies on operation near endfire, where the rotation of the receive beampattern pushes its main lobe outside of the sound cone. The amount of nonreciprocity seen at the angle of peak emission is dictated by the length of the antenna, which affects the angular width of the lobes, and the flow velocity, which determines how much the lobes in the transmit and receive patterns are rotated away from each other.

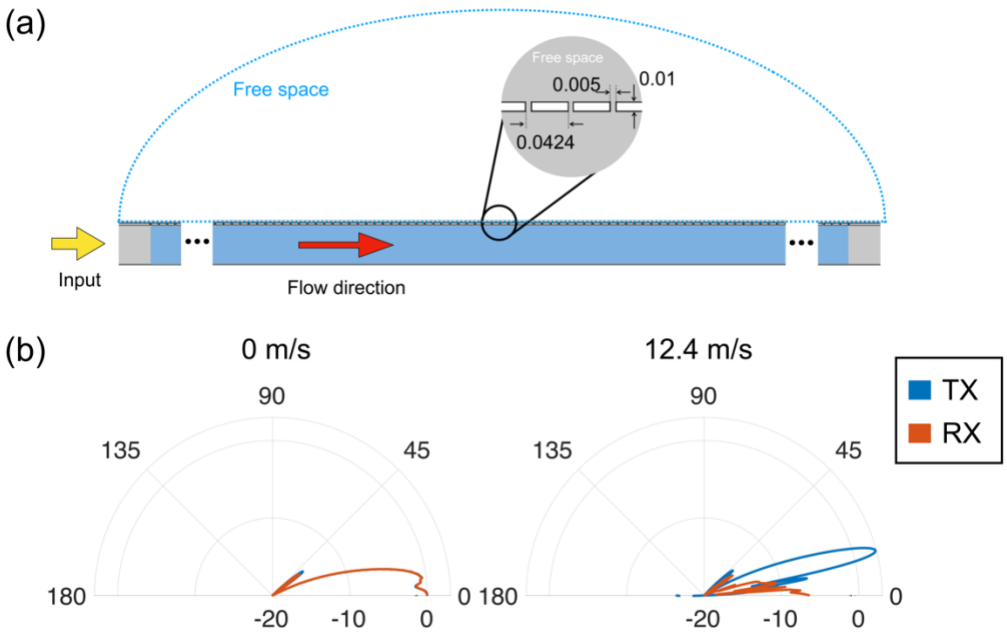

Figure 3.5: (a) Geometry of nonreciprocal leaky-wave antenna. Shunt dimensions given in meters. (b) Transmit and receive beampatterns at a radial distance 130 λ from the antenna without flow (left column) and with flow (right column) for modes 1 (bottom row) and 2 (top row). Values are in decibels, normalized to the maxima when there is no flow.

3.6 CONCLUSION

Steady fluid flow is a powerful way to break time-reversal symmetry in acoustic systems, as it is a property that naturally remains constant regardless of the direction of incoming waves. We have shown that low Mach number flow through straight channels is sufficient to achieve a significant amount of isolation in waveguiding structures. Acoustic Mach-Zehnder interferometry, where incoming sound is split into two paths and later recombined, allows for isolating devices with footprints of a few wavelengths. Alternatively, a waveguide that induces phononic transitions also provides isolation because the transitions are directionally dependent. Frequency-preserving transitions can be enabled by a nonuniform transverse profile combined with a grating. We showed how a directional antenna that violates the typical symmetry between its direction of transmission and reception can be formed by coupling a waveguide with flow to free space. These one-way structures provide a valuable tool in the creation of complex acoustic networks where the ability to isolate one subsection can greatly facilitate system design.

Chapter 4: Non-Foster acoustic radiation from an active piezo-electric transducer[3]

In the previous chapters we have reviewed techniques to break acoustic time-reversal symmetry and used one of these techniques, material flow, to create novel unidirectional acoustic devices. In this chapter we consider the breaking of another common constraint in acoustic devices – the one of passivity. We pay particular attention to the bandwidth limitations that arise in passive acoustic sources and metamaterials and show how these can be surmounted.

In particular, we show that the quality factor of a passive, linear, small acoustic radiator is fundamentally limited by its volume normalized to the emitted wavelength, imposing severe constraints on the bandwidth and efficiency of compact acoustic sources, and of metamaterials composed of arrangements of small acoustic resonators. We demonstrate that these bounds can be overcome by loading a piezoelectric transducer with a non-Foster active circuit, showing that its radiation bandwidth and efficiency can be largely extended beyond what possible in passive radiators, fundamentally limited only by stability considerations. Based on these principles, we experimentally observe a three-fold bandwidth enhancement compared to its passive counterpart, paving the way towards non-Foster acoustic radiation and more broadly active metamaterials that overcome the bandwidth constraints hindering passive systems.

This work is of significance as many of the exciting wave phenomena found in acoustic metamaterials arise as a result of the collective response of subwavelength resonators. To widen the frequency range of these phenomena, it is necessary to understand the source of these bandwidth limitations and explore techniques that can overcome them.

[3] Reprinted with permission from C. Rasmussen and A. Alù, "Non-Foster acoustic radiation from an active piezoelectric transducer," Proc. Natl. Acad. Sci. U.S.A. **118**, e2024984118 (2021).

To that end, we quantify the general tradeoff between size and bandwidth of passive acoustic resonators, and show how this constraint can be overcome by actively loading them. As an example, we demonstrate a large bandwidth enhancement of a sonar transducer by connecting it to a specialized active non-Foster circuit. This important finding can have long-lasting impact in acoustic metamaterials for exotic sound interactions, paving the way to enhanced compact resonant acoustic devices that can be used as sources and sensors of sound and vibrations.

4.1 INTRODUCTION

Techniques to widen the bandwidth over which a system resonates are important in various settings and technologies, given the ubiquity of resonances in wave-based systems. Radiation sources typically operate near a resonance to ensure efficient radiation towards a distant receiver. Resonances are also crucially important in the field of metamaterials, structures with exotic bulk responses arising from subwavelength elements whose resonance ensures strong wave-matter interactions in small volumes. Acoustic metamaterials supporting novel phenomena, such as negative refraction and cloaking, have been recently demonstrated, but their unusual features are inherently limited in frequency because of the narrowband resonances of the underlying unit elements [25,26,140].

In electromagnetics, the well-established trade-off between bandwidth and electrical volume of a small resonant antenna [141] is known as Chu limit, and it provides an important benchmark for antenna design, setting a lower bound on the fractional bandwidth of the antenna given its size [142–145]. Extending the bandwidth beyond this bound is possible only by breaking one or more of its underlying assumptions, notably linearity, passivity and time-invariance. Indeed, temporal modulations of the antenna element or the connected circuitry can overcome this limit, as demonstrated in direct

antenna modulation approaches [146,147], and in switched [148–150] or parametrically modulated [151] systems. Mechanically moving antennas have also been shown to radiate with bandwidths beyond Chu limit [152,153]. Another approach to build broadband electrically small antennas consists in loading them with active circuitry, embedding powered components such as transistors or operational amplifiers (op-amps) to break the passivity condition. This is commonly done by synthesizing a circuit that violates Foster's reactance theorem, i.e., with a reactance that decreases with frequency, e.g., in a negative impedance converter (NIC) circuit topology [154–160]. Such non-Foster circuits have also been recently employed to realize parity-time symmetric systems [15,161]. While in principle the bandwidth of non-Foster antennas can be infinitely extended [162], the main issue that limits the performance of these devices is their stability [163–166].

In the following, we first extend the Chu limit to acoustic radiators showcasing relevant differences between the electromagnetic and acoustic wave domains. We then explore ways to overcome this limit and broaden the bandwidth of small acoustic sources using non-Foster impedance matching. In this context, time modulation has been recently explored to improve the low frequency response of a sonar projector [167,168]. Here, instead, we explore the integration of non-Foster circuit loads in acoustic piezoelectric transducers, commonly used in airborne and waterborne sound transmission, showing a viable path to enhance bandwidth and efficiency of compact sound emitters. We also show how these techniques can be used to widen the bandwidth of exotic material properties in a metamaterial composed of piezoelectric elements.

4.2 Acoustic Chu limit

The quality factor $Q = \omega W / P$ of a resonant sound source is defined as the dimensionless ratio of the time-averaged stored energy W (units of joules) at angular

frequency ω to the power P (units of watts) lost in radiation or dissipation, and it is inversely related to its fractional bandwidth. Following pioneering works in electromagnetics [141,144,145], here we derive a lower bound for Q assuming that the radiator is linear, passive, and time-invariant. As sketched in Fig. 4.1, we consider a sphere of radius a that encloses in its entirety the sound source. In evaluating W, we ignore the additional energy stored inside this spherical region, which depends on the specific implementation of the radiating element, and calculate the stored energy in the acoustic near-fields outside the sphere. This will provide a lower bound to the radiative Q, which can be approached minimizing the stored energy within the source. We also ignore dissipation losses possibly arising within the sphere. They can certainly lower the overall Q, but only at the expenses of lowering the overall radiation efficiency, which is typically not a viable solution to broaden the bandwidth.

The total stored energy in the near-fields of an acoustic source is given by the sum of kinetic and potential energy contributions. In order to induce a resonance, so that the source can efficiently radiate the input energy, an additional reactive element must be added to impedance match the structure. This tuning reactive element must store sufficient energy to make up for the difference between kinetic and potential energies around the source. After impedance matching, the total stored energy is twice the value of either the kinetic or potential energy in the near-fields, depending on which is larger: $W = 2\max\left\{W_k, W_p\right\}$. Assuming no losses other than those associated with radiation, the quality factor at resonance is therefore

$$Q = \frac{2\omega \max\left\{W_k, W_p\right\}}{P_r}. \tag{4.1}$$

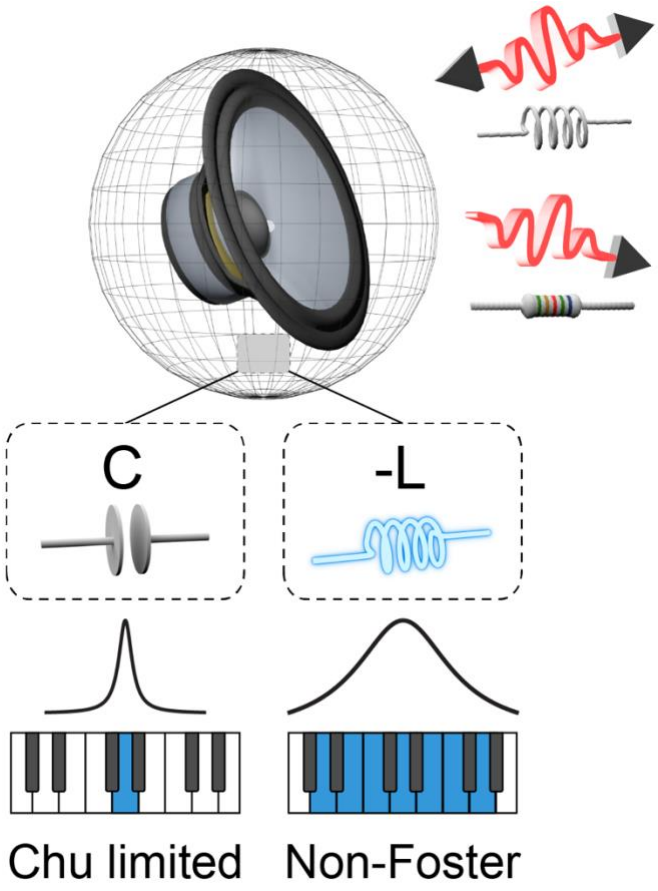

Figure 4.1: An acoustic source connected to a non-Foster element to overcome the Chu bound. The emitted sound field consists of inductive energy stored in the near-fields and resistive energy lost in radiation to the far-field. Adding a capacitive element can create a resonance with a *Q* constrained by the size of the radiator. However, with the use of a non-Foster element such as a negative inductor, the constraint can be overcome.

The total kinetic and potential energies in the waves generated by an acoustic source are composed of both stored and radiated energy, and they are infinite as the traveling portion extends to infinity. The sum of kinetic and potential stored energies can be calculated by subtracting from the total energy the portion traveling outward:

$$W_k + W_p = \int_a^{\infty} \int_0^{2\pi} \int_0^{\pi} \left(\frac{pp^*}{4\rho_0 c_0^2} + \frac{\rho_0 \vec{v} \cdot \vec{v}^*}{4} - \frac{1}{2c_0} \mathrm{Re}\left(p\vec{v}^* \right) \cdot \hat{r} \right) r^2 \sin\theta \, d\theta \, d\varphi \, dr, \qquad (4.2)$$

where * denotes the complex conjugate and $\hat{r}$ is the normalized radial vector. The first and second terms in the integral are indeed the kinetic and potential energy densities, proportional to the squares of the local acoustic pressure and velocity. The last term is the subtracted energy density of the travelling wave. The ambient density and speed of sound are ρ_0 and c_0. The difference between the two stored energies is given by the imaginary part of the equation for the conservation of energy, describing the power flow, corresponding to the reactive acoustic intensity [169]:

$$W_k - W_p = \frac{1}{4\omega} \mathrm{Im} \int_0^{2\pi} \int_0^{\pi} p\left(\vec{v}^* \cdot \hat{r} \right) a^2 \sin\theta \, d\theta \, d\varphi. \qquad (4.3)$$

Combining Eqs. (4.2) and (4.3) we can derive the stored kinetic and potential energies, which can be used in Eq. (4.1). The radiated power is the flux of the power density along any surface that encloses the source:

$$P_r = \frac{1}{2} \mathrm{Re} \oint p\vec{v}^* \cdot d\vec{S}. \qquad (4.4)$$

By generally expressing the radiated field as a sum of outward propagating spherical harmonics centered at the source location, the quality factor can be calculated in terms of a multipole expansion. The pressure is generally given by a sum of multipoles with complex amplitudes A_{lm},

$$p = \sum_{l=0}^{\infty} \sum_{m=-l}^{l} A_{lm} h_l^{(2)}(kr) Y_l^m(\theta, \varphi), \qquad (4.5)$$

where $h_l^{(2)} \equiv j_l - iy_l$ is the spherical Hankel function of the second kind, defined with spherical Bessel functions of the first and second kinds, and Y_l^m is the spherical harmonic

function of degree l and order m. The velocity can be calculated from the pressure gradient using the momentum equation $\vec{v} = i\nabla p / \omega\rho_0$, with the e^{iwt} time convention. Using these expressions, we can evaluate Q in closed form, arriving at

$$Q = \frac{\sum_{l,m} |A_{lm}|^2 Q_l}{\sum_{l,m} |A_{lm}|^2} \tag{4.6}$$

where

$$\begin{aligned} Q_l = \frac{1}{2}\Bigg[ka\left(2 - l\left|h_l^{(2)}\right|^2\right) + (ka)^2\left(j_l j_{l+1} + y_l y_{l+1} - j_l j_l^{'} - y_l y_l^{'}\right) \\ + (ka)^3\left(j_{l-1} j_{l+1} + y_{l-1} y_{l+1} - \left|h_l^{(2)}\right|^2\right)\Bigg] \end{aligned} \tag{4.7}$$

is the individual quality factor when only multipole harmonic of degree l and any order m is excited. It is expressed in terms of spherical Bessel and Hankel functions with argument ka (wavenumber multiplied by radius). The form of Eq. (4.6) reveals that Q is a weighted average of the quality factors of degree l where $|A_{lm}|^2$ are the weights.

We have derived the quality factor in terms of each outward propagating spherical harmonics with index l, with Q_l being the quality factor when the radiation consists solely of harmonic l. As shown in Fig. 4.2, the values of Q_l increase with index l. As the total Q is a weighted sum of these individual values, as a function of the different contributions of each harmonic to the overall radiation, the minimum achievable Q is Q_0. Therefore, the minimum quality factor for a small acoustic radiator scales with the radius of the sphere enclosing the source as $1/ka$, where k is the wavenumber and a the radius, and it can be approached for a purely monopolar source. In electromagnetics, this limit instead scales as $1/(ka)^3$, attained for electric or magnetic dipolar radiation, hence our derivation shows that

acoustic monopolar sources offer broader bandwidths than electromagnetic antennas in the subwavelength limit. In order to approach this lower bound, a passive acoustic source must store as little energy as possible in the region $r < a$. As the size of a passive radiator shrinks, the fields at resonance grow close to the origin, contributing more to the near-field stored energy than to the radiated energy. This fundamentally limits the overall achievable bandwidth.

(a)

	Electromagnetic Q	Acoustic Q
	-	$\frac{1}{ka}$
	$\frac{1}{ka}+\frac{1}{(ka)^3}$	$\frac{2}{ka}+\frac{2}{(ka)^3}$
	$\frac{3}{ka}+\frac{6}{(ka)^3}+\frac{18}{(ka)^5}$	$\frac{4}{ka}+\frac{9}{(ka)^3}+\frac{27}{(ka)^5}$
	$\frac{6}{ka}+\frac{21}{(ka)^3}+\frac{135}{(ka)^5}+\frac{675}{(ka)^7}$	$\frac{7}{ka}+\frac{27}{(ka)^3}+\frac{180}{(ka)^5}+\frac{900}{(ka)^7}$
Chu bound	 $\frac{1}{(ka)^3}$	 $\frac{1}{ka}$

(b)

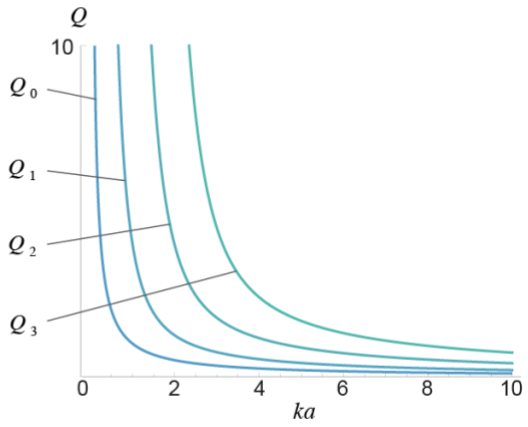

Figure 4.2: Quality factors for multipolar orders 0 to 3. (a) Expressions for acoustic and electromagnetic multipoles. The Chu bound (final row) is the lowest possible Q in the limit $ka \ll 1$. (b) Plot of the acoustic Q showing the divergence for subwavelength radiators. The lowest curve, corresponding to Q_0, is the ultimate bound for acoustic radiators.

4.3 Broadband Impedance Matching Using Non-Foster Circuits

At resonance, the cancellation of excess kinetic or potential stored energy through an impedance matching element makes sure that the input reactance of the system goes to zero. While a system largely detuned by its natural resonance has a very large reactance, corresponding to the large stored energy in its near-fields, we induce a subwavelength

resonance by loading it with a reactive lumped element that compensates for it. However, this form of impedance matching can be achieved only at a single frequency when considering passive loads, due to the fact that Foster's reactance theorem requires both the input and load reactance to grow with frequency. On the contrary, an active non-Foster matching element, not bound by this passivity constraint, can compensate the input reactance over a broad frequency range.

We consider, as a common acoustic source, an electro-acoustic transducer, which radiates an acoustic signal proportional to the input voltage signal applied at its terminal and finds widespread use in research and commercial applications. A common way to couple the electrical and acoustic domains is the piezoelectric effect, based on which an applied electric field creates mechanical strain in the material. When the structure is small relative to the radiation wavelength, a lumped-parameter circuit model can well describe the piezoelectric response, as shown in Fig. 4.3(a). An input voltage is applied to the clamped electrical capacitance C_e and to the mechanical portion of the circuit through a transformer with coupling constant N. The mechanical portion of the circuit is a resonant mass spring system moving at velocity v and radiating into the surrounding medium with radiation impedance Z_{rad}.

These transducers are commonly operated in the frequency range around their mechanical resonance, for which the reactance in the mechanical branch is small while the electrical capacitance dominates the reactive response of the system. A common technique to improve the transducer performance around this frequency is to use a tuning inductor to compensate for this capacitance [170]. The overall quality factor of the dissipation-free source is therefore typically larger than the Chu limit, due to the additional presence of stored energy in the reactive elements C_e, L_m, and C_m, in addition to the energy in the tuning inductor. At resonance, the wavelength of the elastic wave is generally on the same order

of magnitude as the size of the structure. The wave speed of commonly used piezoelectric ceramics is about ten times higher than the one in air and about twice than in water, so the source typically operates at a moderate value of *ka*, with *k* being the wavenumber in the surrounding medium. The Chu limit is not particularly constraining at these frequencies, since *ka* is not small.

Here, we are interested in the source operation in the deeply subwavelength regime. In this frequency range the transducer response is capacitive, as seen in Fig. 4.3, where we show the input susceptance, which linearly increases at low frequencies. A resonance can be induced in this range by using a tuning inductor with a larger inductance than the typical tuning inductor. However, the susceptance of a passive inductor, negative at all frequencies, can cancel the input capacitance only at a single frequency in this low frequency regime [Fig. 4.3(b)]. This is due to Foster's reactance theorem, which requires the reactance (or susceptance) of any passive, lossless circuit to always increase with frequency. In the context of Fig. 4.3(b), the slope of any possible blue curve can only be positive and therefore cancel the low-frequency positive slope of the transducer (green curve) at one or more isolated frequencies.

By breaking the assumption of passivity, the slope of the matching reactance can be made negative using a non-Foster component and the transducer's low-frequency susceptance can be cancelled over a broader frequency range. The susceptance of a negative capacitor is the mirror reflection of the transducer's positive capacitance and it can compensate the capacitive response over a broad frequency range [Fig. 4.3(c)]. A source connected to this transducer with cancelled total susceptance can then radiate with high efficiency over the entire low-frequency range.

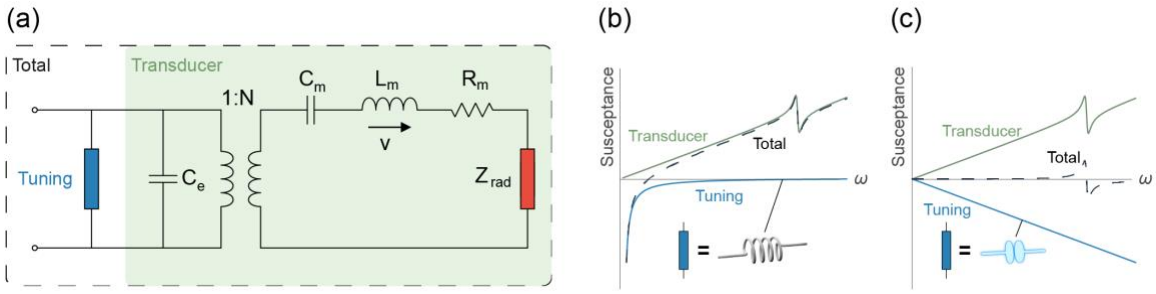

Figure 4.3: Non-Foster cancellation of input susceptance in a piezoelectric radiator. (a) An acoustic piezoelectric circuit model with tuning element, electrical capacitance, electromechanical turns ratio, mechanical RLC components, and radiation impedance. (b), (c) The total susceptance of the circuit (dashed) is the sum of the transducer (green) and tuning (blue) susceptances. (b) The total susceptance is small only around one frequency when the transducer is tuned with an inductor. (c) The susceptance is cancelled over a broad frequency range when tuned with a non-Foster negative capacitance.

When deriving the lower bound on *Q* in the previous section, we did not make any assumption on the specifics of the radiator, and in particular on the additional energy stored in the piezoelectric element, which largely contributes to the total reactance resulting in a *Q* factor larger than the lower bound. A non-Foster matching element, powered by its own energy source, can partially compensate for the stored energies in the transducer and acoustic near-fields, offering an effective way to lower the overall *Q* factor and extend the resonance bandwidth well beyond what achievable with a passive tuning inductor.

4.4 NON-FOSTER PIEZOELECTRIC RADIATOR

We employ a negative impedance converter (NIC) to realize our non-Foster matching load. A NIC circuit inverts the sign of the impedance of a circuit element by flipping the sign of its input voltage or current. For example, a current inversion NIC can transform the impedance of a component from *Z* to –*Z* by supplying current to a source instead of drawing current from it in response to an applied voltage. The flow can be

reversed because the NIC is an active circuit with its own power source. These circuits have historically found use in the design of active RC filters and, more recently, in the study of non-Hermitian and PT symmetric systems. NIC circuits can be synthesized using op-amps or transistors. Floating (ungrounded) NICs require the use of multiple op-amps [171]. We choose instead to use a grounded NIC topology, which can be realized with a single op-amp. This choice necessitates the use of a current source, or a voltage source with a large internal resistance R_s. The goal is to combine this grounded NIC negative capacitor in parallel with a piezoelectric transducer to create a broad low frequency resonance (Fig. 4.4).

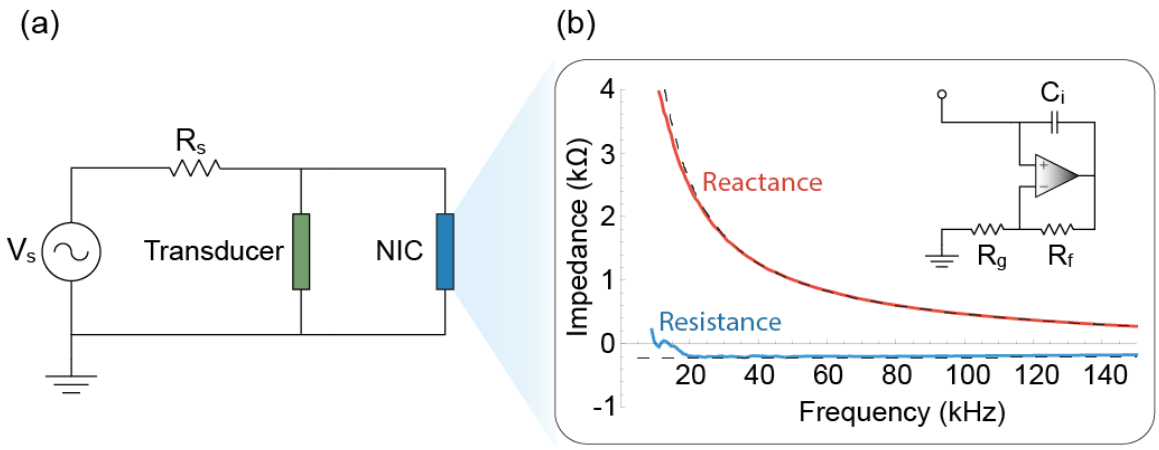

Figure 4.4: A non-Foster piezoelectric radiator. (a) A negative impedance converter is used to induce a low-frequency resonance in a piezoelectric transducer. (b) The real part (resistance) and imaginary part (reactance) of the input impedance to the NIC circuit, showing experimental (solid) and theoretical (dashed) results. The NIC is composed of a single op-amp whose feedback gain is controlled by two resistors and turns capacitor C_i into a negative capacitor with a non-Foster, negatively-sloped reactance.

The NIC negative capacitor topology, shown in the inset of Fig. 4.4(b), is a non-inverting amplifier with the capacitor placed between its input and output. The complex impedance of the NIC is a function of the closed loop gain G,

$$Z_{NIC} = \frac{1}{sC_i(1-G)}, \tag{4.8}$$

where s is the complex frequency. When the closed loop gain is 2, the NIC impedance is the one of a negative capacitor $-C_i$. However, since the gain is a dispersive complex function, there is an accompanying real part of Z_{NIC} and the effective negative capacitance is bandwidth limited. This limitation is captured by modeling the open loop gain of the op-amp with a single pole model, $A_0/\left(1+s/\omega_p\right)$, where A_0 is the zero-frequency open loop gain and ω_p is the 3 dB frequency. The closed loop gain is then

$$G = \frac{A_0}{1+\frac{s}{\omega_p}+\frac{A_0}{G_0}}. \tag{4.9}$$

Resistors R_f and R_g form a voltage divider where G_0 is the reciprocal of the voltage division ratio: $G_0 = 1 + R_f / R_g$. The amount of closed-loop feedback is controlled by adjusting the ratio of R_f and R_g. The desired closed-loop feedback gain is much less than the zero-frequency open loop gain of a typical op-amp. This feedback gain is achieved by keeping G_0 small such that $G_0 \ll A_0$. As seen from Eq. (4.9), the feedback gain G is then given by G_0 at low frequencies.

We physically implemented this NIC circuit and measured its input impedance to compare with our circuit model predictions [Fig. 4.4(b)], finding an overall good agreement. An Agilent E5071C network analyzer is used to measure the S_{11} scattering parameter (reflection coefficient) of the NIC circuit. The input impedance is then calculated

from S_{11} using $Z = Z_0\left(1+S_{11}\right)\big/\left(1-S_{11}\right)$ where Z_0 is the 50 Ω line impedance. We observe the desired non-Foster negative slope of the negative capacitor in the frequency range of interest with some accompanying negative resistance. The synthesized non-Foster element can be used to induce a broadband low-frequency resonance in our piezoelectric transducer.

4.5 Experimental realization of a non-Foster acoustic source

The non-Foster acoustic source is completed by placing the fabricated NIC circuit [Fig. 4.5(a)] in parallel with a cylindrical piezoelectric transducer [Fig. 4.5(b)] and a waveform generator. A swept sine input is used for input and the velocity of the transducer is measured from 0 to 45 kHz with a laser Doppler vibrometer [Fig. 4.5(c)]. We see that the amount of negative capacitance provided by the NIC is enough to induce a resonance near 20 kHz, significantly lower than the transducer's 120 kHz natural resonance. As a point of comparison, the same measurement is performed when an inductor is used as the tuning element. The inductor is subject to Foster's reactance theorem and the bandwidth is limited. With the Foster-violating NIC circuit, we see that the bandwidth shows a 320% improvement. The peak level of the NIC response is also modestly higher, resulting in a combined gain bandwidth improvement of 450%.

The piezoelectric transducer is a 1 mm thick, 10 mm long PZT-4 cylinder with an outer radius of 5 mm. The overmold is Stycast 2651 and covered the cylinder and two Macor end caps [172]. The piezoelectric material was radially poled and the primary mechanical resonance is the radial breathing mode. The NIC circuit is based on the Texas Instruments OPA549 op-amp. The capacitor and feedback gain parameters, 3 nF and 2.03 respectively, are chosen as they were observed to induce a subwavelength resonance at a frequency and amplitude similar to that of the Foster tuning element, which was a 22 mH inductor (Bourns RL181S-223J-RC).

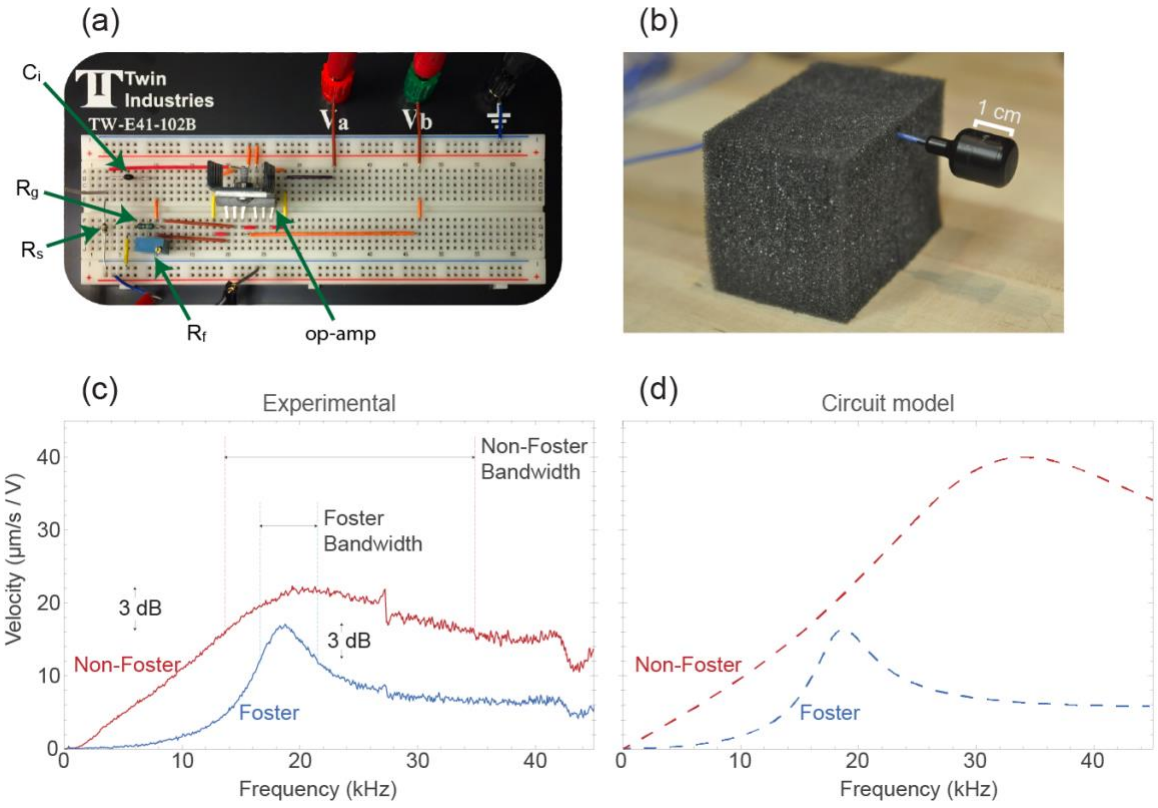

Figure 4.5: Bandwidth of a non-Foster acoustic source. (a) Implementation of the NIC circuit. External connections are to the cylindrical piezoelectric transducer, shown in (b), to the power source for the op-amp, and to the function generator. (c), (d) Experimental and modelled velocity spectra of the piezoelectric transducer when connected to the Foster (blue) and non-Foster (red) tuning elements. The non-Foster tuning extends the measured low-frequency resonant bandwidth while ensuring stability.

The measurement is performed with an Agilent 33120A function generator connected in series with a 10 kΩ resistor to provide approximately constant-current output. The velocity of the transducer is measured at a central point on the curved face of the protective overmold using a Polytec PSV-500 laser Doppler vibrometer. The piezoelectric element supports predominately a breathing radial motion in this frequency range with the highest levels of vibration seen along the central equator of the cylinder. The vibrometer captures the magnitude of this motion by measuring the outward surface velocity at a point

in this region of maximum response. Extraneous low frequency noise is removed with a 1 kHz high pass filter. The function generator supplies a 3 Vpp swept frequency input and the op-amp is powered by an Agilent E3631A supply set to a symmetric 25 V which supplies on average 24 mA during the measurements.

The theoretical model of the non-Foster acoustic source is completed by retrieving the circuit model parameters for the piezoelectric transducer. Circuit model parameters are retrieved based on a measurement of the velocity of the piezoelectric transducer connected to the Foster tuning element. Parameters are chosen that provide the best fit around the induced and mechanical resonant frequencies. In this retrieval process, loss in the tuning inductor is modelled as a series 30.8 Ω resistance, a value estimated from the quality factor and DC resistance provided by the manufacturer. The self-resonant frequency of the inductor is sufficiently high to ensure that any effective capacitance could be safely neglected. The best fit is found with the transducer parameters C_e = 3.4 nF, N = 0.3, C_m = 0.48 nF, L_m = 3.85 mH, and R_m = 60 Ω.

With a fully specified circuit model, we can examine the predicted velocity of the transducer per input volt. The transfer function between the velocity output and voltage input is a function of the complex variable s. To see how our circuit model compares to our experimental results, we plot the magnitude of the transfer function as a function of the real frequency ω by letting $s = i\omega$ [Fig. 4.5(d)]. We find that it captures the salient features of the measured response. An even better fit could be obtained by using a more complex circuit model to describe the transducer response. The level of circuit complexity we chose to use here ensures that the model is able to make accurate predictions (for example, for the stability analysis in the following), while maintaining enough simplicity for the results to be easily interpretable.

We further our results by exploring the system response as the parameters of the NIC are varied. Experimentally we observe that, by increasing the amplifier feedback gain G_0, we can adjust the bandwidth and peak amplitude of the radiator with great flexibility [Fig. 4.6(a)]. In numerical simulations, we employ our circuit model to explore combinations of G_0 and C_i over a wide range. A suitable performance metric is the gain bandwidth product (*GBW*, peak amplitude multiplied by bandwidth) of the non-Foster system normalized to the one of a passive matching network. The numerical results reveal a band in parameter space where the performance is maximized, reaching gain bandwidth improvements of about eight [Fig. 4.6(b)].

However, the magnitude of the transfer function only contains information about the steady-state response of the transducer. Attention must be paid to the transient response, as it may grow without bound in systems with active components and become oscillatory or unstable. A system is unstable if any pole of the transfer function (i.e., any frequency s where it diverges) lies in the right half of the complex plane. By evaluating the location of the transfer function poles as G_0 and C_i are varied, we can see what combinations assure stable operation [Fig. 4.6(b), red curve]. We see that the band of highest gain bandwidth follows the region of instability, indicating a tradeoff between maintaining a margin of stability and achieving the best possible performance. We also have experimentally validated the instability contour by measuring the onset of instability at a few locations in parameter space [Fig. 4.6(c)], verifying that it indeed follows our theoretically derived contour. To create the instability curve, a potentiometer is used to increase the feedback gain to the point where unstable oscillations were seen in the velocity and voltage signals. After swapping in a new capacitor C_i the process is repeated. We continue this procedure until the full parameter space is sufficiently explored. These results make clear that, within the region of high gain-bandwidth, there is increased sensitivity to the system parameters,

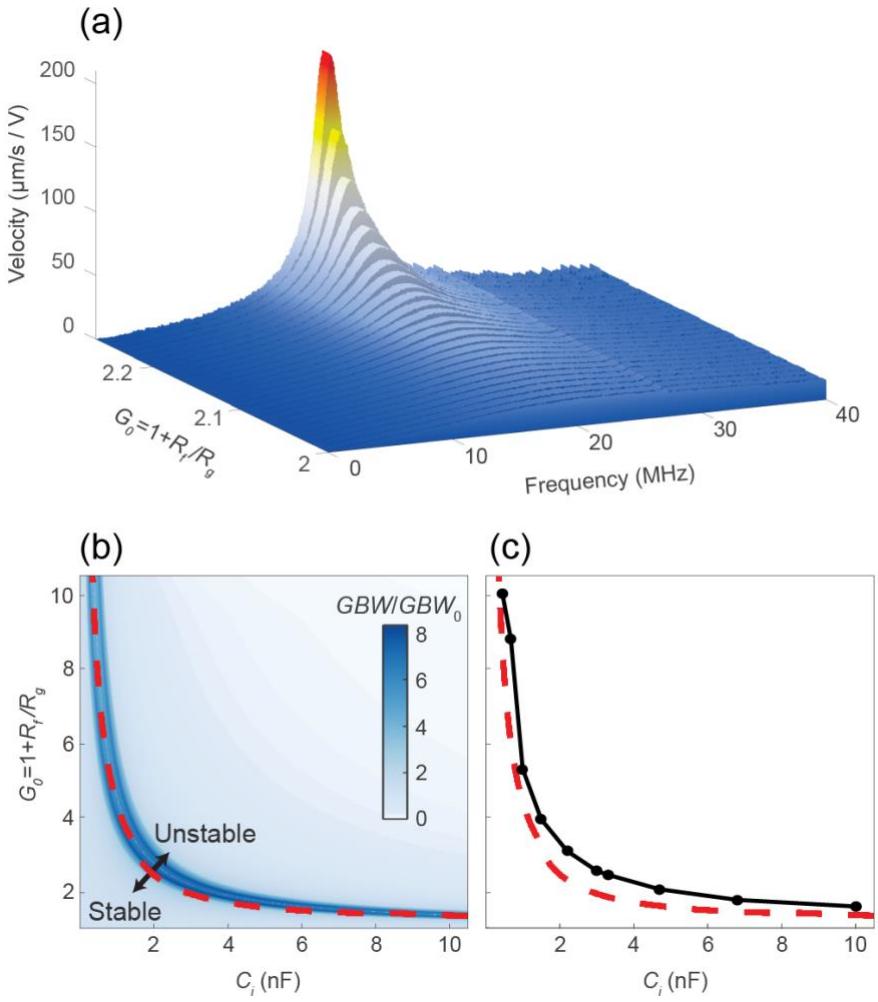

Figure 4.6: Stability bound of non-Foster acoustic source. (a) The velocity frequency response as the amplifier's feedback gain, G_0, is increased from 2 to 2.26. (b) Numerical examination of the non-Foster gain bandwidth, *GBW*, normalized to the Foster gain bandwidth, GBW_0, as G_0 and C_i are varied in the NIC. The red curve is the boundary of stability predicted by the model. (c) To validate the numerical stability results, we compare the theoretical instability curve (red, dashed) to measured points of instability onset (black, solid).

which is helpful in understanding why there is not more agreement with the experimental results in Fig. 4.5. A more complex model of the underlying circuits may be able to capture better the dispersion in this region, but at the price of a less intuitive physical picture. Anyhow, both the experimental demonstration and the analysis of our model confirm that

the proposed technique can practically achieve broadly enhanced gain-bandwidth products for acoustic radiation from a subwavelength transducer, well beyond the limitations of passive radiating elements.

4.6 NON-FOSTER ACOUSTIC METAMATERIAL

A metamaterial with exotic effective constitutive parameters can be realized as an array of subwavelength resonators. However, the frequency dispersion of the effective parameters is generally limited by passivity and causality considerations, consistent with Kramers-Kronig relations, which are the analogue of the Foster's reactance theorem applied to material properties. These considerations imply that exotic material responses, such as a negative density or bulk modulus, necessarily occur over a narrow frequency range in passive metamaterials, typically aligned with the resonant response of the underlying constituent elements.

As already discussed, the resonant response of small resonators can be extended well beyond the passivity limitations by non-Foster loading. By realizing a metamaterial with these active inclusions, the effective material properties are not expected to obey the bandwidth limitations of passive metamaterials. Consider for instance a 3D array of subwavelength piezoelectric elements with non-Foster loading. In a pressure field with wavelength significantly larger than the element size, the incident pressure p_{inc} is roughly uniform over the surface of the piezoelectric and causes the element to uniformly expand and contract. This modulation of the element's volume works as a harmonic source of volume in the fluid of density ρ, with a volume velocity $Q = \frac{1}{\rho}\frac{\partial M}{\partial t}$ where M is the monopole moment $M = \int_{V_0} \rho dV$. In a time-harmonic field we can write the relations $M = \frac{\rho Q}{i\omega} = \frac{\rho \int \mathbf{u} \cdot d\mathbf{S}}{i\omega} = \frac{\rho u S}{i\omega}$, where the volume velocity is the integrated normal velocity over the element surface, which we take to be a constant. The velocity u is the expansion

and contraction of the element by the incident pressure, which can be obtained from the element's mechanical input impedance: $u = Sp_{inc} / Z_{in}$. The amount of monopole moment created by an incident pressure is given by the monopole polarizability α, defined by $M = \alpha p_{inc}$. With these relations in place, we find

$$\alpha = \frac{\rho S^2}{i\omega Z_{in}}. \tag{4.10}$$

An array of these elements in the background fluid of bulk modulus B_0 supports an effective bulk modulus B_{eff} that can be defined through a suitable homogenization procedure [62,173]:

$$\frac{B_0}{B_{eff}} = 1 + \frac{V^{-1}}{c^{-2}\alpha^{-1} - C_{\text{int}}}, \tag{4.11}$$

where c is the speed of sound in the background fluid. When the elements are not densely packed, we can neglect the interaction term C_{int} and the bulk modulus is linearly related to the element's polarizability. Exotic values of the effective bulk modulus are obtained when the element's polarizability are resonant which, from Eq. (4.10), we achieve by minimizing the element's input impedance. As before, we can use a tuning element placed across the electrical terminals of the piezoelectric to cancel the reactance of the transducer and bring the impedance to a very small value at a subwavelength frequency. Using the circuit model from before, we have impedances from the electrical and mechanical portions of the transducers (Z_e and Z_m) and an impedance from the tuning element (Z_t). While previously we examined the input impedance into the electrical portion of the circuit model, the impedance of interest here is the one looking into the mechanical portion of the circuit.

Circuit theory allows us to express the input impedance in a form where the effect of the tuning impedance is readily apparent [174], using the circuit model in Fig. 4.7. We get:

$$Z_{in} = Z_{in,Z_t \to \infty} \frac{Z_t + Z_N}{Z_t + Z_D}, \tag{4.12}$$

where $Z_{in,Z_t \to \infty}$ is the input impedance if the tuning element is open-circuited and Z_N and Z_D are the impedances seen by the tuning element with the input shorted and open, respectively. To bring Z_{in} to a small value, we need the tuning impedance to minimize both real and imaginary parts of Z_N.

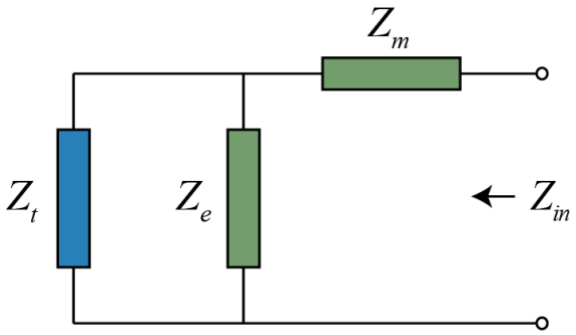

Figure 4.7: Input impedance of a piezoelectric transducer with mechanical and electrical impedances. Tuning impedance Z_t is applied across the terminals of the piezoelectric to make the input impedance small.

The impedance seen by the tuning element with the input shorted is the parallel impedance of the mechanical and electrical portions of the transducer: $Z_N = Z_m \parallel Z_e$. At low frequency, the transducer impedance is dominated by the electrical and mechanical capacitances and the main requirement for the tuning element is to cancel out the large imaginary impedance of the parallel capacitances. This can be clearly seen by examining a plot of the susceptance as in Fig. 4.8. We use the model parameters from before for a

spherical element with a 5 mm radius. The transducer susceptance ($\mathrm{Im}[1/Z_N]$) is nearly a straight line as expected from an effectively capactive response. We can cancel this susceptance near $kd = 0.15$ (k is the wavenumber in the background medium and d is the average distance between neighboring array elements) by adding to it the negative susceptance of a 1.5 H inductor. Shown in Fig. 4.8(a), this brings the total input susceptance to zero in a narrow range. Alternatively, using a non-Foster circuit such as a theoretical negative capacitor [Fig. 4.8(b)] we can cancel the susceptance over a broad range. As a specific example of a negative capacitor, we consider our NIC circuit with a capacitance and feedback gain of 3 nF and 2.1477, respectively connected in series with a 206 Ω resistor to eliminate residual negative resistance [Fig. 4.8(c)]. The non-Foster tunings are able to bring the susceptance low over a broad frequency range.

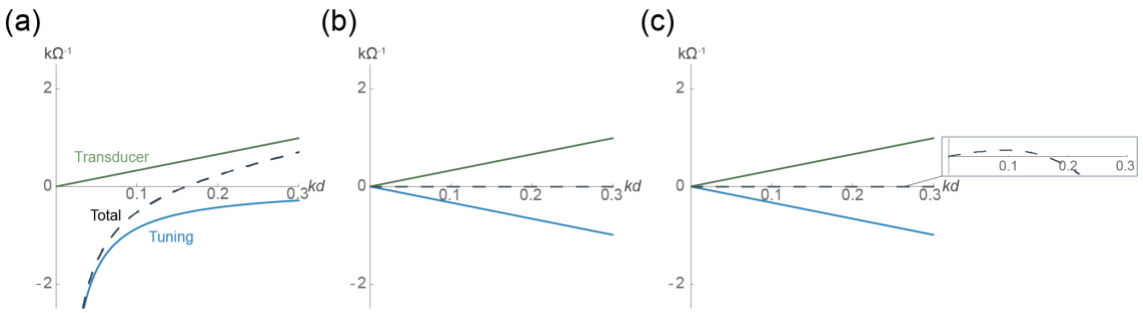

Figure 4.8: Susceptance of the piezoelectric transducer ($\mathrm{Im}[1/Z_N]$), the tuning element ($\mathrm{Im}[1/Z_t]$), and the resulting total input impedance ($\mathrm{Im}[1/Z_{in}]$). (a) The addition of the transducer capacitance with a tuning inductance minimizes the susceptance over a narrow frequency range. (b) An ideal negative capacitance can drive the susceptance to zero over a broad range. (c) A synthesized negative impedance circuit also drives the susceptance near zero with some dispersion.

Considering water as the background material and a filling ratio of 0.1, we plot the polarizability and bulk modulus of our metamaterial using Eqs. (4.10) and (4.11). As expected, driving the input impedance close to zero creates a resonant peak in the

polarizability [Fig. 4.9(a)] and a large dispersion in the effective bulk modulus [Fig. 4.9(b)]. A negative effective bulk modulus is achieved due to the collective response of the

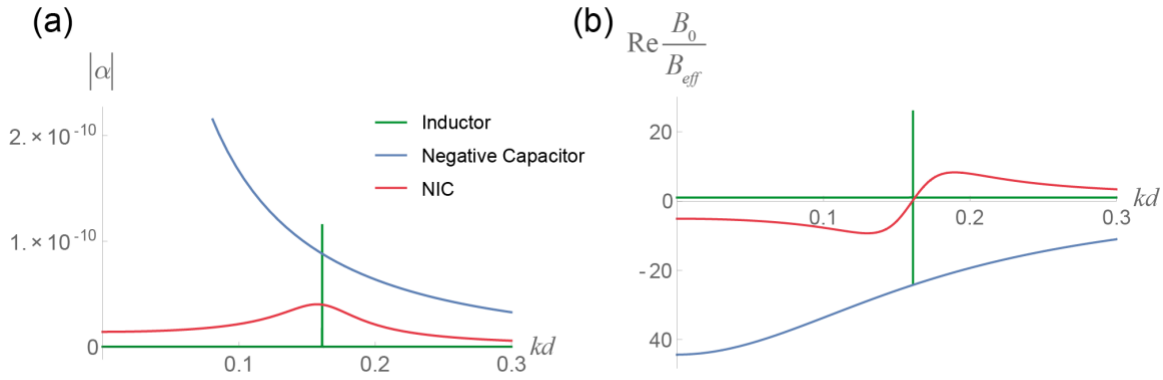

Figure 4.9: Frequency dispersion of the effective bulk modulus of an array of piezoelectric elements in water is widened by non-Foster tuning. (a) Polarizability and (b) resulting effective bulk modulus are very narrow when an inductor is used as the tuning element of the resonant inclusions, but it can be made mich larger using an ideal negative capacitor. A realistic negative impedance circuit (NIC) enables a realistic implementation of a negative capacitor, yielding a broad bandwidth over which the effective bulk modulus is negative.

resonant inclusions. In the case of an ideal negative capacitor, the bandwidth is made extremely wide with a bulk modulus that is negative until the frequency is high enough that the transducer's mechanical inductance and resistance become comparable to the capacitances. The NIC tuning case illustrates the wide bandwidth behavior that can arise from a realizable non-Foster tuning of metamaterial elements, implying an ultrabroadband negative bulk modulus, well beyond the bandwidth limitations implied by Kramers-Kronig relations for passive media. Ref. [175], as an example, shows a passive metamaterial offering a relatively broad range of frequencies over which the bulk modulus is negative. However, its dispersion is fundamentally limited by the Kramers-Kronig bounds, and

flatter frequency dispersion, leading to broader bandwidths of operation for practical devices, may be achieved only by overcoming passivity, linearity or time invariance, as proposed in our work. With our approach, a three-dimensional acoustic metamaterial with near zero or negative parameters can be created with a bandwidth constrained only by stability considerations.

This result shows that the non-Foster loading opens unique opportunities to realize broadband acoustic metamaterials overcoming the bandwidth limitations of passive systems for a variety of opportunities in the context of exotic sound manipulation.

4.7 DISCUSSION

Our results outline the exciting opportunities offered by non-Foster circuits in the context of active acoustic sources and metamaterials, offering bandwidth enhancements well beyond the limits of passive systems. Our derived quality factor limit provides a general lower bound on the bandwidth of any passive acoustic resonator, given its size. To approach this limit, a transducer needs to minimize its internal stored energy and loss. For a piezoelectric transducer, this requires low moving mass, high compliance, high electro-mechanical coupling, and low electrical and mechanical losses. A typical piezoelectric transducer operates far from this limit, and our approach to active circuit loading can compensate for this excess stored energy, extending significantly the available bandwidth for low-frequency resonances.

Stability considerations determine the ultimate limits of performance in these scenarios. In our work, we have presented an analytical model that captures the main phenomena describing active radiating elements, which can accurately predict the stability boundaries of this approach. Our simple non-Foster op-amp circuit loading a piezoelectric transducer already shows a significant bandwidth enhancement, and further improvements

can be expected by considering more complex circuit layouts and dispersion engineering to extend the stability region. Further optimization of the dispersion of the active tuning elements paves the way towards even larger gain bandwidths from subwavelength acoustic sources, of interest in a wide range of applications.

Non-Foster loads also offer a new approach to improve the bandwidth of acoustic metamaterials, which have been shown to enable exotic sound-matter interactions but typically only over a narrow frequency range. This limitation is tied to the frequency response of the individual subwavelength resonators that constitute the material. By using active non-Foster loads, the bandwidth of each individual element can be extended beyond the passivity limitations, while maintaining a subwavelength footprint that ensures the possibility of homogenizing the array of elements as a bulk material response. We have studied a metamaterial made of an array of subwavelength non-Foster elements, showing that it can support exotic bulk material properties over large bandwidths, beyond the limitations of passive acoustic metamaterials. Our findings therefore open interesting opportunities for metamaterial technology, not necessarily limited only to the acoustic domain, but extendable also to mechanics, electromagnetics and nano-optics.

Chapter 5: Compressibility-near-zero acoustic radiation[4]

In the previous chapters we have discussed constraints that arise due to time-reversal symmetry and the absence of gain. Part of the motivation for this research is to improve the performance of acoustic metamaterials. These architected structures are noteworthy for their ability to shape sound waves in ways that exceed what is possible with natural materials. In this chapter we present a novel acoustic source based on a metamaterial zero-index effect. As the basic functionality of the device, a structure that transforms a simple omnidirectional source into a highly directive beam of sound, does not rely on broken time-reversal symmetry or passivity, its performance is bound by the constraints discussed in the previous chapters. Future work could include the addition of symmetry or passivity-breaking effects to endow the acoustic zero-index directional device with asymmetrical propagation characteristics or broader bandwidth performance.

A hallmark of near-zero-index materials is the uniform phase profile that the waves experience as they propagate with static-like properties in these media. This feature has been exploited in electromagnetics for several applications, including for the realization of compact, highly directive antennas illuminated by a single source. Here we discuss the promise of near-zero metamaterials for acoustic radiation, based on the cutoff of a higher-order mode in a waveguide with small holes. We show that the near-zero nature of this phenomenon ensures unusual robustness to disorder, which is analyzed using a statistical description of the radiation patterns for randomly generated location of the holes. The radiation pattern can be made more directive by simply increasing the overall radiating aperture, without having to worry about the specific location of the individual holes and their relative distance. The proposed zero-compressibility material offers a promising

[4] Reprinted with permission from C. Rasmussen and A. Alù, Compressibility-near-zero acoustic radiation, Phys. Rev. Appl. **15**, 024022 (2021). Copyright 2021 by the American Physical Society.

alternative to traditional acoustic directive sources due to its design simplicity, inherent robustness and compact profile.

5.1 INTRODUCTION

Highly directive radiation implies the need for a large aperture, since the far-field angular distribution of a given source is the spatial Fourier transform of the source plane [72]. Transducer arrays can provide a large radiating area, but they are overly costly and require a complex feeding network, making them unappealing for many applications. Reflectors and lenses, such as the sound domes used in museums to broadcast sound to a single listener, are simpler, but rely on large and bulky external structures. Superdirectivity from small apertures is possible, but it implies extremely large reactive fields, in practice enabling only modest gains over the directivity of a uniform aperture of the same size [176]. In another alternative, the tradeoff between aperture and directivity can be sidestepped by exploiting nonlinear phenomena, such as in parametric arrays, where a beam of high amplitude ultrasound is demodulated to audible frequencies through nonlinearities during propagation. The resulting radiated beam is highly directional, though these speakers generally suffer from poor bass response, limited efficiencies and large costs.

Recent advances in the field of near-zero materials provide an intriguing alternative to these approaches [177,178]. Acoustic metamaterials supporting exotic values of their effective density and compressibility have enabled a plethora of new phenomena, such as enhanced absorption, cloaking, and subdiffraction imaging [25,140]. These properties have been associated with negative effective constitutive parameters, which are necessarily bandwidth limited, implying that there is always a frequency where density and/or compressibility transition from negative to positive values, at which the material shows

near-zero-index properties, with propagation characterized by very long wavelengths and a quasi-static phase distribution. This field uniformity has been used in electromagnetic near-zero materials to realize various phenomena, including the possibility of implementing highly directive antennas [179,180].

In acoustics, negative and near-zero density can arise from collective dipolar resonances, such as in dense arrays of resonant membranes forming metamaterials [181,182]. Collections of monopolar resonances, as in Helmholtz resonators [183], modify instead the effective compressibility. Resonances of both these constitutive parameters in the same frequency band can result from scatterers that support multiple mode types [184,185], such as coupled membranes [186], star-shaped scatterers [187], cylindrical inclusions [188], coiled space structures [189] or Mie resonators [190,191]. As an alternative technique, it has been recently shown that the dispersion of a hollow waveguide operated at its higher-order acoustic mode can provide a simple yet effective way to implement negative or zero compressibility with very low loss and maximized bandwidth [192]. This is dual to the electromagnetic scenario, in which negative permittivity has been achieved in a parallel-plate waveguide by Rotman [193], and exploited in various metamaterial implementations [194,195].

In this work, we demonstrate how the effective zero-index response of a cavity excited near its higher-order cutoff, with small holes coupling the fields to free-space, can be used to realize a highly directive acoustic source. The field uniformity in this radiating structure makes it resilient to changes in geometry and disorder. We show that the directivity can be simply controlled by varying the lateral dimensions of the cavity and that its directive emission is largely independent of the location of the radiating holes.

5.2 A ZERO-INDEX DIRECTIVE ACOUSTIC SOURCE

In an acoustic waveguide, transverse confinement induces inherent dispersion of the phase speed for all modes that are not uniformly distributed in the transverse plane. This implies the presence of a cutoff frequency, below which the mode cannot propagate. At the cutoff, forward and backward propagation are degenerate, the phase velocity is infinite, since the wave number is zero, and the wavelength is correspondingly infinite. Figure 5.1(a) shows the propagation of an incoming sound wave through narrow channels feeding a larger middle waveguide section designed to operate at the cut-off of its higher-order mode. Indeed, we can observe how the wave experiences close to zero phase advance throughout this middle section, despite its length being comparable to the wavelength in the feeding channels. The feed and exit waveguides are located near the antinodes of the excited mode in the middle section to ensure large coupling. In this region the effective index of refraction, defined as the ratio of the sound speed to the phase speed, $n = c/c_p = c\sqrt{\rho_{eff} C_{eff}}$, is effectively zero because the phase speed diverges. In particular, it is the effective compressibility in the middle section to go to zero $C_{eff} \approx 0$, not the density. This can be seen by noting that the impedance $Z = p/u_{axial} = \sqrt{\rho_{eff}/C_{eff}}$ is infinite instead of zero as the axial particle velocity $u_{axial} \approx 0$. The effectively zero phase speed means that the axial wavenumber is also effectively zero: $\beta = \omega\sqrt{\rho_{eff} C_{eff}} \approx 0$ where ω is the angular frequency. The middle section in Fig. 5.1(a) therefore acts as an axial compressibility-near-zero (CNZ) medium around its cut-off frequency. The difference in cross-section between the feeding channels and the middle section in this geometry compensates for the large impedance mismatch between the two media, enabling complete tunneling of the wave through the zero-index cavity, known as supercoupling [196]. As detailed in [192], the channel is connected at the bottom of the large CNZ section, so that the zero-order plane wave mode in the feeding waveguides can efficiently couple to the

higher-order mode of the larger middle section operated at cut-off. Despite the cut-off, and correspondingly very large impedance, the wave is fully transmitted through the cavity and preserves the same phase throughout the length of the CNZ section.

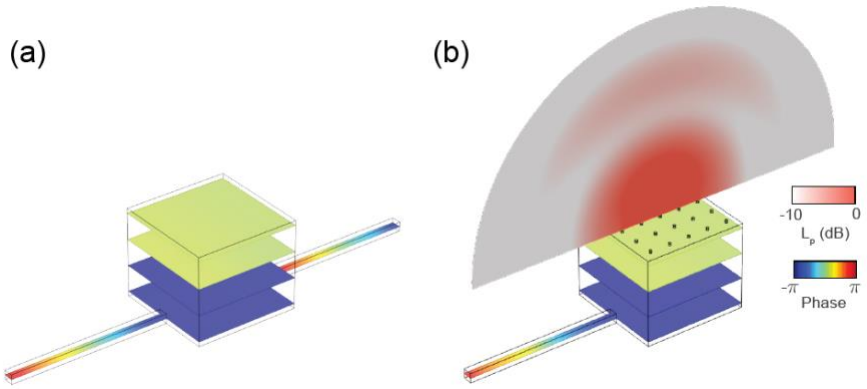

Figure 5.1: Compressibility-near-zero directive radiation. (a) The phase of an incoming travelling wave is unchanged as it traverses the CNZ cavity operated near the cutoff of its higher-order mode. The wave is fully transmitted through the exit waveguide. (b) Efficient broadside radiator with a uniformly-illuminated aperture realized by a square array of holes carved in the top wall of the CNZ cavity.

The uniform phase distribution across a large aperture is ideally suited for efficient broadside acoustic radiation with large directivity, in analogy with the wavefront manipulation properties of zero-index materials in optics [197]. We achieve this functionality by carving small holes in the top plate of the CNZ section and removing the exit waveguide, as illustrated in Fig. 5.1(b), small enough to only weakly perturb the resonant mode, but sufficient to efficiently couple the incoming wave to free space. Interestingly, because the resonance of interest in the cavity arises transversely, as the mode is at cutoff, the distance between the lateral walls of the cavity is irrelevant to control the resonance features, and the established mode is expected to efficiently leak towards the far-field in the broadside direction for any total size of the hole array, given its uniform

field profile. This is in contrast to an electromagnetic cavity antenna operating in its lowest mode (of type 101 or 011), where the aperture efficiency is at most 81%, because of its nonuniform phase profile [198]. In contrast, the CNZ cavity uniformly broadens the size of the localized source for broadside radiation, leading to unitary aperture efficiency. Our design also differs from acoustic leaky-wave antennas, in which a travelling wave is made leaky through periodic holes introducing a -1 spatial Floquet mode within the sound cone [199,200]. Acoustic leaky-wave antennas typically suffer from largely inefficient use of the aperture, as the wave is attenuated along the waveguide and eventually absorbed to prevent backreflection [199]. These leaky modes also typically experience a cutoff for radiation at broadside, implying very inefficient radiation.

Insights into the operation of the CNZ acoustic radiator can be gained using a Green's function approach, assuming that the cavity is fed by a generic monopole source placed inside the cavity, as in Fig. 5.2. Using an $e^{-i\omega t}$ time convention, we seek a solution to the equation $\nabla^2 p + k^2 p = -4\pi S\delta\left(\vec{x}_0 - \vec{x}\right)$ for the acoustic pressure *p* at location $\vec{x}$ due to a source at $\vec{x}_0$. Assuming for simplicity that all walls are sound hard, the solution can be expressed in terms of the three-dimensional orthonormal cavity eigenmodes $\psi_m = \sqrt{\alpha/L^2 H}\cos\left(m_x \pi x/L\right)\cos\left(m_y \pi y/L\right)\cos\left(m_z \pi z/H\right)$, where the cavity side length is *L*, the height is *H*, and the mode index is $m = \left(m_x, m_y, m_z\right)$. The normalization factor $\alpha = \alpha_x \alpha_y \alpha_z$, where $\alpha_i = 1$ if $m_i = 0$, $\alpha_i = 2$ if $m_i > 0$, ensures orthonormality over the cavity volume, $\int \psi_m \psi_n \, dV = \delta_{mn}$. The solution in the cavity with walls of (large) wall impedance *Z* is [72]

$$p = -4\pi S \sum_m \frac{\psi_m \psi_{m0}}{k^2 - k_m^2 + ik\rho c \sum_n \iint \frac{\psi_m \psi_n}{Z} dS}. \tag{5.1}$$

In the case of all sound hard walls ($Z \to \infty$), the last term in the denominator vanishes and the level of excitation of mode *m* is determined by how close the mode wavenumber $k_m = \sqrt{(\pi m_x / L)^2 + (\pi m_y / L)^2 + (\pi m_z / H)^2}$ is to the free space wavenumber $k = \omega / c$ and by the overlap integral between the source and the modal distribution which in this case is simply $\psi_{m0} \equiv \psi_m(\vec{x}_0)$. In our CNZ cavity, all the walls are sound hard except for the top surface, where the response of the surface patterned with holes is approximated by a large impedance Z_t. In this case, the surface integrals collapse and the expression for the pressure reduces to

$$p = -4\pi S \sum_m \frac{\psi_m \psi_{m0}}{k^2 - k_m^2 + ik\rho c\alpha_z / Z_t H} \equiv \sum_m a_m \psi_m , \tag{5.2}$$

where the amplitude of mode *m* is a_m.

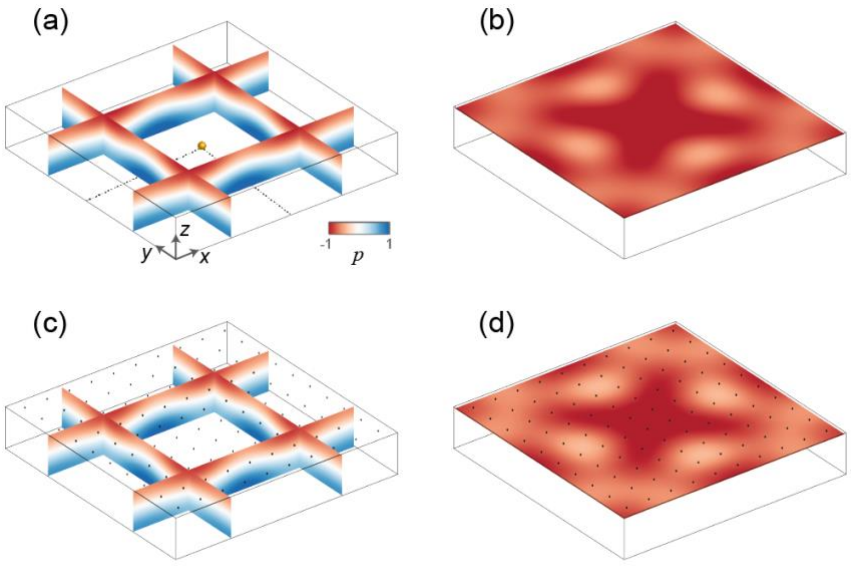

Figure 5.2: Green's function analysis with a holey top surface. (a,b) Theoretical calculation of the normalized pressure response in the CNZ cavity. The source is centrally located on the bottom of the cavity and it produces a wave field consisting mainly of the 001 mode with *xy* uniformity. (c,d) Corresponding full-wave simulation results.

The impedance Z_t of the top surface is the one of a holey plate. Intriguing scattering phenomena have been shown to arise in holey plates when the acoustic wavelength is comparable to either the hole length or hole-to-hole spacing due to collective resonant behavior [201,202]. Further effects due to surface and plates modes are expected when the plate elasticity is taken into account [203]. In our geometry the structural parameters are sufficiently subwavelength that the specific acoustic transfer impedance can be rigorously homogenized and is well-approximated by a lumped mass and resistance [204]:

$$Z_t = \frac{d^2 \rho \omega}{\pi} \left(k + \frac{i\left(l + 1.7a\right)}{a^2} \right). \tag{5.3}$$

The resistance scales with the free space wavelength, while the reactance grows as the hole size shrinks. For the cavity in Fig. 5.2, with hole radius a = 1 mm, hole length l = 2 mm, and hole spacing d = 5 cm operating at 2000 Hz, the impedance is mostly reactive, Z_t = 443 + 44,770i Pa·s/m. We further model the air as inviscid and thermally non-conducting with density ρ = 1.21 kg/m^3 and sound speed c = 343 m/s. While some amount of thermoviscous loss is expected in the subwavelength holes, the overall behavior of the cavity as a directive source remains largely unaffected by the presence of dissipation as the viscous and thermal boundary layers, δ_ν = 0.049 mm and δ_t = 0.057 mm, are significantly smaller than the hole size. Maa's model for the impedance of a microperforated plate with thermoviscous losses can be used to capture the role of viscothermal effects [205]. The impedance in this case is 1,365 + 46,135i Pa·s/m. Vibroacoustic coupling can be minimized by choosing a high impedance material with sufficient thickness. A thicker top plate would lead to more thermoviscous losses, affecting the radiation efficiency, but due to symmetry the uniform aperture illumination would remain unchanged.

The time-averaged power supplied by the source can be retrieved by integrating the intensity vector over a sphere of vanishing size centered at the source. This procedure yields

$$W = W_{ff} \operatorname{Im} \frac{p}{kS}\bigg|_{\vec{x}_0}, \tag{5.4}$$

where $W_{ff} = 2\pi|S|^2 / \rho c$ is the power radiated by the source in free space. With Eq. (5.2), the relative amount of power injected by the source to mode *m* is then $W_m \propto \psi_{m0} \operatorname{Im} a_m / S$. In a cavity with all walls sound hard ($Z_t \to \infty$) there is no mechanism for energy dissipation and all modal amplitudes are purely real. As the power is proportional to the imaginary part of the pressure, the power delivered by the source is zero, as it is unable to deliver any power to a totally reactive load. In a practical realization of the antenna, a feed network that transforms the input impedance of the radiator to match the source impedance would enable maximum power transfer.

Using the lumped impedance model of the holey top surface, we can calculate the power provided by a source located in the bottom center of the cavity to each mode, in order to ensure that the response is dominated by the desired 001 mode. We plot the acoustic pressure given by Eq. (5.2) in Fig. 5.2(a) for a cavity with side length *L* = 0.5 m and height *H* equal to half wavelength (~8.6 cm). Based on Eq. (5.4), we estimate that the power provided to mode 001 is 90 times (19.5 dB) larger than the one provided to the closest mode (440). To validate our analysis, we also ran full-wave finite-element simulations of the geometry, finding very good agreement, as shown in Fig. 5.2(b). Extracting the modal power from the full-wave results indeed shows that the 001 and 440 are the two dominant modes, separated by 18.5 dB. Similar results have been obtained for other source positions, confirming the robustness in performance of the CNZ radiator.

5.3 DIRECTIVITY CONTROL

The uniform phase distribution on the top plate of the cavity and the fact that its shape does not affect the cutoff frequency for the *z*-directed mode ensure that we can increase or decrease the source directivity by simply increasing or decreasing the lateral dimensions of the cavity. With reconfigurable walls we may span the directivity from the one of a compact source – with directivity near unity – to a highly directive beam as the aperture area increases. We test the variation in directivity as the aperture is increased in Fig. 5.3, where we plot the directivity retrieved from simulations as a function of *kL*, the wavenumber multiplied by the side length, assuming a lattice constant d = 5 cm, subwavelength at the operation frequency of 2000 Hz. The simulations agree well with the

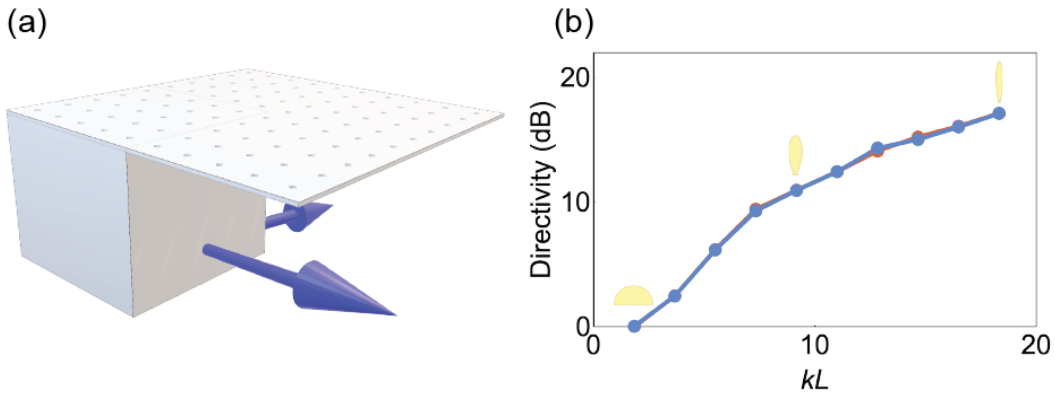

Figure 5.3: Directivity controlled by the cavity side length. (a) Underneath a surface patterned with holes, a cavity with adjustable side walls can be used to control the directivity of the CNZ radiator. (b) The directivity from full-wave simulations (blue) matches the one of a square array of monopole sources (red), showing the nearly perfect illumination regardless of size. Insets: Beam patterns in the *xz* plane for three side lengths showing directivity ranging from omnidirectional to highly directive.

directivity of a rectangular array of point sources excited with uniform phase and amplitude, for which the directivity $D = 2\pi \Big/ \int_0^{2\pi} \int_0^{\pi/2} |A|^2 \sin\theta d\theta d\varphi$ is obtained through the array factor

$$|A|^2 = \left| \frac{\sin\left(N_x \gamma_x / 2\right)}{N_x \sin\left(\gamma_x / 2\right)} \right|^2 \left| \frac{\sin\left(N_y \gamma_y / 2\right)}{N_y \sin\left(\gamma_y / 2\right)} \right|^2, \tag{5.5}$$

where $\gamma_x = k d_x \sin\theta\cos\varphi$ and $\gamma_y = k d_y \sin\theta\sin\varphi$. For the square array of holes in our CNZ cavity $d_x = d_y = d$ and $N_x = N_y$. The good agreement between our simulations and the analytical formula for a phased array clearly demonstrates the nearly ideal aperture illumination and inherent reconfigurability of our CNZ radiator.

5.4 DISORDER INTOLERANCE

The field uniformity in the CNZ cavity adds the interesting advantage of immunity to disorder. The eigenfrequency of an electromagnetic zero-index cavity can be made robust to shape variations by embedding a dielectric inclusion [206]. In the geometry at hand, the array of holes is expected to achieve uniform illumination regardless of the lateral cross-sectional cavity shape, as long as the excited field is dominated by the selected cavity mode. Interestingly, this insensitivity to disorder applies also to the position of the holes in our geometry. In the extreme case of holes being positioned entirely at random over the aperture, the main broadside beam is still expected to arise, with little change in directivity. Figure 5.4 shows the effect of this disorder, as we study the *x*-*z* plane beam patterns for 1,500 randomly generated hole samples, and compare them to the periodic square array. For each disordered sample, the position of the 100 holes was pulled from a uniform distribution over the 0.5 m by 0.5 m top surface. Figure 5.4(a) shows one of the disordered samples, where the location of any individual hole was equally likely to be anywhere in

the square cross section. The baseline ordered array is a square lattice with 5 cm spacing between holes. All results are calculated for airborne propagation at 2000 Hz with 100 coupling holes of radius 1 mm and height 2 mm. The far-field intensity patterns are retrieved from full-wave simulations assuming the aperture in an infinite baffle.

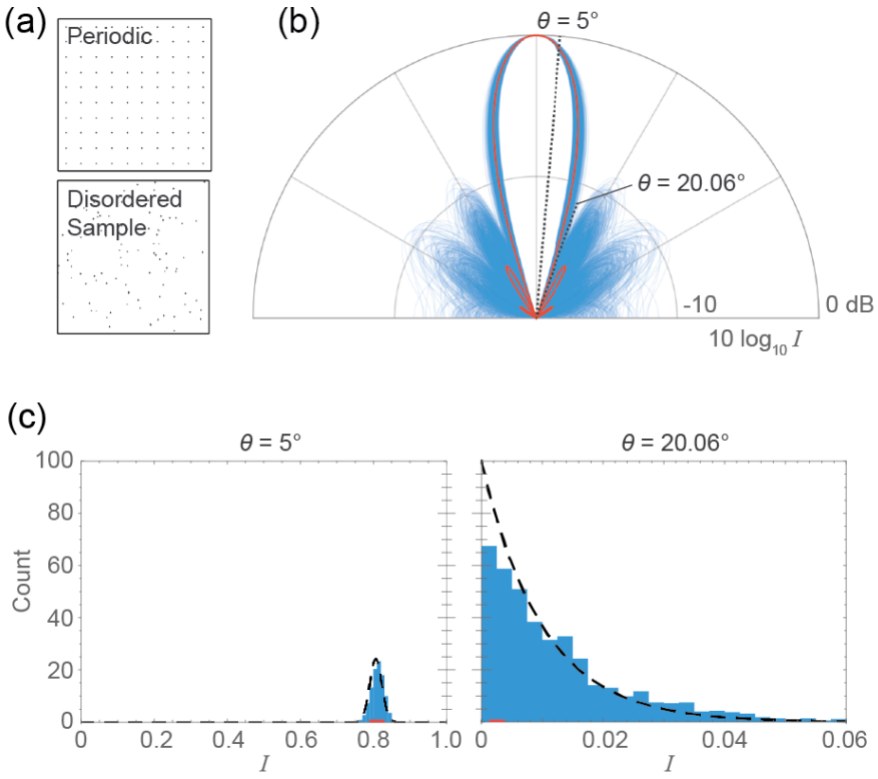

Figure 5.4: Effect of disorder in the hole position. (a) Top surfaces for the periodic square array of holes and a sample disordered array. (b) Comparison of the *xz* intensity radiation pattern from full-wave simulations of the 1,500 disordered samples (blue) and the baseline periodic square array (red). All results are normalized to the intensity of the ordered array at broadside. The main lobe of the beampattern maintains its width and direction in all randomly generated geometries. (c) Probability distributions of the intensities of the disordered samples at 5º and 20.06º from broadside with theoretically predicted results (black dashed line). The small red bars mark the intensities of the periodic array.

The statistical distribution of the random beam patterns can be understood by examining the Fraunhofer far-field where the sound pressure is the Fourier transform of the source plane velocity:

$$p = \frac{-ik\rho c}{2\pi}\frac{e^{-ikr}}{r}\iint u_0(x_0, y_0) e^{-\frac{ik}{r}(xx_0+yy_0)}\, dx_0\, dy_0, \tag{5.6}$$

with r as the radial coordinate. In particular, the intensity $I = |p|^2 / 2\rho c$ at broadside ($x = y = 0$) is simply given by the integration of the particle velocity across the aperture:

$$I_{\theta=0^\circ} = \left|\frac{k}{4\pi z}\iint u_0\, dx_0\, dy_0\right|^2 \equiv \left|\frac{k}{4\pi z} Q\right|^2. \tag{5.7}$$

Considering the holes as point velocity sources of unit strength, the volume velocity Q remains unchanged as long as the number of holes is kept constant and as long as the position and geometry of the holes do not significantly affect the cavity mode: $Q = \iint \sum_{l=1}^{N} \delta(x_l - x_0, y_l - y_0)\, dx_0 dy_0 = N$. This matches the agreement across all samples at broadside seen in Fig. 5.4(b) and it indicates that the holes do not largely influence the cavity mode excitation, meaning that the particle velocities are the same at all coupling holes and that the system can be analyzed as a nonuniformly spaced (spatially tapered) array of point sources with equal amplitude. Normalizing these values, we can describe the distribution of the intensities of the random samples as a delta function centered at one: $f(I)_{\theta=0^\circ} = \delta(I-1)$.

Away from broadside, the statistical distribution of the intensities can be obtained using the central limit theorem. Because the holes are uniformly excited, the far-field pressure is simply the sum of the phases due to the relative positions of the holes. In the x-z plane, only the x positions of the holes are relevant. The normalized pressure magnitude is $P = \frac{1}{N}\left|\sum_{l=1}^{N} e^{-i\Psi_l}\right|$, where $\Psi_l = X_l k \sin\theta$ is the phase contribution of the l-th hole in terms

of the *x* coordinate X_l uniformly sampled over the interval defined by the cavity length: $\left[-L/2, L/2\right]$. At the critical angle θ_c, given by $2\pi = Lk\sin\theta_c$, the phase Ψ_l is sampled over the full $\left[-\pi,\pi\right]$ angular range. At that angle of radiation, the composite pressure is a sum of *N* two-dimensional (2D) vectors in the complex plane of unit length with random orientation.

Interestingly, this property connects our problem to the theory of random walks, with a probability distribution in terms of Bessel functions, derived using characteristic functions [207]

$$f\left(P\right) = P\int_0^\infty \left[J_0\left(\xi/n\right)\right]^N J_0\left(P\xi\right)\xi\, d\xi. \tag{5.8}$$

As the number of holes becomes large this integral becomes equal to the Rayleigh distribution with variance $1/2N$:

$$f\left(P\right) = 2NPe^{-NP^2}. \tag{5.9}$$

The statistics for the intensity can be similarly derived, and follow an exponential decay:

$$f\left(I\right) = Ne^{-IN}. \tag{5.10}$$

These distributions are a common first step in describing the statistics of disordered media, such as that of speckle patterns, rogue events or spectroscopy. In the problem at hand, they are a first approximation, as they rigorously apply only at the angle θ_c. At other angles, the phases can take on values over an arbitrary range $\left[-\Phi/2, \Phi/2\right]$, which can be thought of as a 2D random walk where the orientation of each step is limited to an angular range of Φ radians. In this case, with recourse to the central limit theorem the probability distribution for the intensity is derived assuming a large number of holes, and is given by

$$f(I)=\int_0^{2\pi}\frac{1}{4\pi\sigma_X\sigma_Y}e^{-I\cos^2\theta'/2\sigma_Y^2}e^{-\left(\sqrt{I}\sin\theta'-\mu_X\right)^2/2\sigma_X^2}\,d\theta'. \tag{5.11}$$

The dependence on Φ is contained in the mean and variances of the underlying Gaussian distributions that arise from the central limit theorem. The closed-form expressions are

$$\begin{aligned}\mu_X &= \frac{2\sin(\Phi/2)}{\Phi},\\ \sigma_X{}^2 &= \frac{\Phi^2-4+\Phi\sin\Phi+4\cos\Phi}{2\Phi^2 N},\\ \sigma_Y{}^2 &= \frac{\Phi-\sin\Phi}{2\Phi N}.\end{aligned} \tag{5.12}$$

Here, X and Y refer to the distributions of the real and imaginary parts of the random variable $e^{-i\Psi}=X+iY$. As the interval is symmetric about the real axis, the mean of Y is always zero. Eq. (5.10) is used to plot the probability distribution at the critical angle $\theta=\theta_c=20.06^\circ$ in Fig. 5.4(c) and Eq. (5.11) is used to plot it at an angle closer to the normal ($\theta=5^\circ$). The good agreement found with the histograms from the full-wave simulations validates that the operation of the CNZ source is well protected from disorder. The coupling holes are uniformly illuminated even when they are randomly placed, and can thus be treated simply as a nonuniformly spaced array.

Nonuniform hole locations can be used as a knob to reduce sidelobe levels or increase directivity. Foundational theoretical studies [208,209] and more recent optimization schemes [210,211] describe the advantages and design procedures for spatially tapered arrays. Here, these advantages are achieved using a single source. For example, grating lobes are generically not present in non-uniform arrays as seen in Fig. 5.5 (inset, gray lines). A lack of periodicity can then be a useful approach to limit the levels of all sidelobes. To examine this effect, we widen the hole spacing of the previous geometry

to the size of a wavelength and correspondingly increase the cavity size to $L = \sqrt{N} d\pi/3$ (the $\pi/3$ factor is to avoid the excitation of spurious modes). We are operating now at the point of a Rayleigh-Wood anomaly, where Fig. 5.5 shows the expected horizontal grating lobes appearing in the periodic array, compared to the aperiodic radiation patterns for a few random samples. At small Φ, i.e., close to broadside, the distribution is a delta function centered at 1, as previously noted. This is apparent in Fig. 5.5, as the dark blue distributions approach the shape of a Gaussian peaked at 1 as Φ reaches its lowest values.

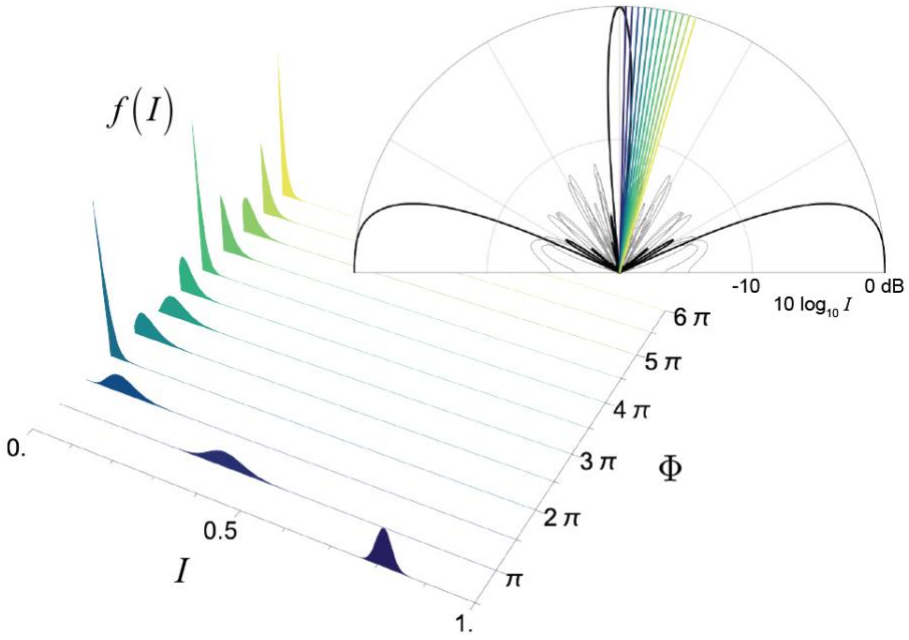

Figure 5.5: Probability distributions as the radiation angle increases from broadside. The distributions of intensity values are color coded according to what angle of radiation corresponds to the particular value of Φ. Inset: The intensity radiation patterns of an ordered array of holes spaced one wavelength apart (black) compared to the aperiodic patterns of five disordered runs (gray). Colored lines indicate the radiation angles at which the probability distributions are evaluated.

At angles of radiation where $\Phi = 2\pi l,\ l \in \mathbb{Z}^+$ the distributions are the exponential functions in Eq. (5.10). While at these multiples of 2π the distributions are exactly exponential, the behavior between multiples of 2π is somewhere between the one of an exponential decay and a Gaussian centered away from the origin. However, there is less deviation from the exponential behavior between multiples of 2π as *l* becomes large. This can be understood by considering where a random walker would end up after taking *N* = 100 steps: when Φ is small, only a narrow range of angles in the forward direction is allowed for each random step. After the full 100 steps, the walker inevitably ends up in about the same place as any other walker (all disordered samples have the same behavior near broadside). When Φ is a multiple of 2π, all directions are equally likely for each step and it is likely that the walker will be found somewhere near the origin after the 100 steps. In the intermediate case $\Phi = 3\pi$, the walker can step in any direction, but it is 2 times as likely to take a step in the forward direction, the $\left[-\pi/2, \pi/2\right]$ angular range, than in the backward direction. If $\Phi = 5\pi$, the walker is now just 1.5 times as likely to take a step in the forward direction. In this way, as Φ gets large, the exact value of Φ becomes less important and the distribution approaches the one of an exponential decay for any large value of Φ, as seen in Fig. 5.5. The implication is that the sidelobe levels of our random hole arrays are unlikely to ever match the level of the main lobe, in the same way as the random walker with all directions available for each step is unlikely to take 100 consecutive steps in the same direction. Strictly speaking, the random walker analogy holds for the distribution of pressure magnitudes $f\left(P\right)$, though the conceptual framework gives insight into $f\left(I\right)$ as well.

5.5 CONCLUSIONS

Following ideas developed in the context of zero-index electromagnetic metamaterials, we have introduced an approach for directive sound radiation robust to disorder. By selectively exciting a suitable cavity mode at cutoff, we have shown that an acoustic resonant cavity provides ideal aperture efficiency, even in the presence of disorder. It should be emphasized that some care should be taken into the cavity geometry and source location, so that the desired mode is selectively excited. For example, while the lateral dimensions of the cavity were able to increase over many lattice increments, it is necessary that the lattice constant is not a simple fraction of the wavelength to avoid the excitation of other modes with lateral field variations. In addition to cavity shape, the desired mode may be selectively excited through the use of a judicious source configuration, such as the location and shape of a waveguide feed.

The decoupling of temporal and spatial variation in near-zero media gives freedom to modify the overall aperture geometry without affecting the useful properties of the wave field. As an example, we have shown how reconfigurable walls in a CNZ cavity can directly shape the directionality of the emitted sound. And, drawing from probability theory, we have developed a statistical model to demonstrate that the CNZ source is highly robust to disorder. With a sufficient number of holes, the radiation of disordered samples becomes predictable in the presence of any level of disorder. The model shows that disorder can potentially become even beneficial, generically acting to suppress grating lobes while maintaining the behavior of the zeroth-order broadside beam.

The resonant condition dictates that the cavity be a half wavelength in height. The coupling holes modify this condition slightly and a stronger response in the cavity is possible at a slightly shifted frequency, but this is a small effect and the results are not presented here, as the overall behavior is similar in both cases. It should be pointed out

that, by modifying the impedance of the top surface, for example with a more sophisticated engineered surface, the profile of the cavity can be drastically reduced, as demonstrated in electromagnetics [212,213]. This concept is illustrated in Fig. 5.6. A resonant broadside beam is maintained as the height of the radiator decreases by specifying the required phase-

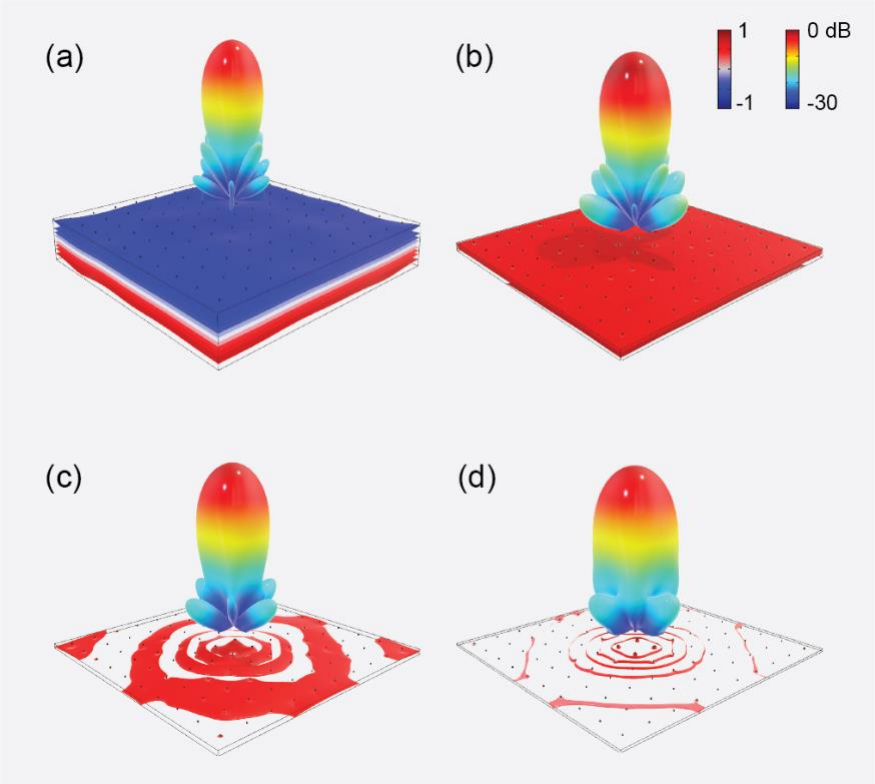

Figure 5.6: Phase-shifting metasurfaces to reduce the radiator height. Pressure isosurfaces are shown within the structure and radiation patterns are shown above. (a) A holey sound hard top surface with the structure height equal to a half-wavelength. (b-d) The radiator height is decreased while changing the impedance of the top plate to ensure a resonant response.

shifting impedance for the top plate. The wave in the cavity is reflecting off the bottom surface, which is sound hard and so it imparts no phase shift in reflection, and the top surface, which can also be approximated as a sound hard boundary. In this case the resonant

condition is given by the phase relationship $2\pi m = 4\pi H/\lambda$, with m being an integer. If the top surface is instead engineered to impart a phase shift φ_r to the reflected wave, the phase relationship becomes $2\pi m = 4\pi H/\lambda + \varphi_r$. In essence, the reflection phase is a degree of freedom that uncouples the relationship between the height of the cavity and the wavelength of operation. Figure 5.6 shows the case for which the top surface offers different amounts of reflection phase shift, enabling the antenna profile to become much smaller than a wavelength. In addition, a phase shifting surface can also be useful to increase the source frequency bandwidth by compensating the frequency-dependent free space phase with a linearly-varying reflection phase, as demonstrated for an electromagnetic antenna in [214].

A waveguide operated near cutoff provides a particularly straightforward path towards near-zero-index responses in acoustics. But other near-zero methods, such as the use of resonant inclusions, provide further options for acoustic near-zero directive sound, though it can be difficult to maintain consistency among the inclusions. Regardless of how the near-zero behavior is obtained, our work shows a promising pathway of the underlying phenomena to shape acoustic radiation patterns as an alternative to more traditional directive acoustic designs.

Chapter 6: Conclusions and Future Work

Time-reversal symmetry and passivity are broad concepts in the study of wave propagation. Surveying these topics is a bit like a stargazer observing the vast panorama of the nighttime sky. The expansive sight gives the viewer an understanding of the overall structure among the celestial bodies and can reveal large-scale relationships and patterns. An examination of fundamental aspects of wave propagation is valuable in this way and it allows us to make sweeping statements about the behavior of acoustic systems based on only a couple of pieces of information. Describing acoustic systems in terms of physical symmetries is an example of this. These symmetries, broken or not, act as great organizing principles, allowing us to make firm predictions about the performance of a device or material without needing to know the details of its composition. In this work we have adopted this broad vantage point and illustrated the possibilities that are opened by the breaking of time-reversal symmetry. We have showed how it is often accompanied by the breaking of reciprocity and enables devices and phenomena that are sensitive to the direction of acoustic propagation. An overview of phenomena enabled by these nonreciprocal effects and a thorough description of reciprocity theorems was given. This included a discussion of what techniques have been used or could be used in the future to break these reciprocity theorems. We also broadly considered passivity and showed how this leads to the acoustic Chu limit, which gives a strict bound on the bandwidth-efficiency of any passive acoustic radiator based only on its maximum radial length.

This dissertation also contains analysis of some specific acoustic devices. These projects provided a different vantage point – that of an astronomer with a telescope, now narrowing in on a particular promising piece of the sky. The broad principles are brought to life as the individual systems are specific illustration of the underlying scientific laws. These acoustic systems are devices or materials with properties that are predictable based

on the general principles of wave propagation. This dissertation contained studies of time-reversal- and passivity-breaking structures that exemplify this zoomed-in perspective, brought to life through numerical simulations and physical proofs of concept. In chapter 3, we used steady flow to create an acoustic isolator with a design inspired by the Mach-Zehnder interferometer. Other isolator designs were presented, including one based on phononic transitions induced in a notched waveguide with flow. By coupling such a structure to free space, we demonstrated an acoustic leaky-wave antenna with transmission/reception asymmetry. Chapter 4 contained an illustration of the bandwidth enhancement made possible by the inclusion of a gain element in an acoustic radiator. We synthesized a non-Foster circuit and connected it to a piezoelectric transducer and measured its widened resonant linewidth. This work showed how it is possible to overcome the acoustic Chu limit through the use of acoustic gain, subject to stability concerns. And, by considering an array of acoustic transducers loaded with non-Foster elements, we showed how the frequency range of negative material properties of acoustic metamaterials can be widened.

This work paves the way for many future research opportunities, with possibilities in both fundamental studies on time-reversal- and passivity-breaking and in innovations centered around the particular devices and structures described here. One promising future direction is the breaking of time-reversal by temporal modulation. By keeping temporal modulations unreversed in reciprocal scenarios, they are sources of time-reversal breaking and nonreciprocity. Dynamic metamaterials, in which waves interact with time-dependent systems, enable effects such as active steering and frequency mixing not seen in their static counterparts [215,216]. As discussed in chapter 2, modulation has been previously studied in the context of nonreciprocal effects, but the focus up to now has been mostly restricted to fairly simple modulation schemes. There is a large body of theoretical, computational,

and technological work to be done in examining more arbitrary spatiotemporal variations. Also of future interest is time-reversal and passivity breaking in acoustic bianisotropic structures. Bianisotropic, or Willis, media have coupled momentum density and volume strain fields which gives them substantial ability to shape sound and vibration, for example in recent demonstrations of bianisotropic metasurfaces efficiently redirecting [217] and blocking sound [64]. These promising features could be extended through the introduction of gain elements. And, in a demonstration of the possibilities unlocked by broken time-reversal symmetry in Willis structures, a recent paper has shown unusual material property response made possible by flow in a Willis structure [68]. Another direction is to advance the work in near-zero acoustics. A highly-directive acoustic source based on the compressibility-near-zero response of a waveguide at cutoff was introduced in this work, but other directive sources based on various near-zero acoustic effects are possible. The inclusion of active sources or temporal modulations in zero-index antennas could lead to novel capabilities and wider bandwidths. Future work could also include developing a better understanding of the tradeoff between stability margin and the bandwidth and efficiency of active acoustic materials and devices. While in principle, active media can bypass constraints such as the Chu limit or Kramers-Kronig relations, the amount of improvement is difficult to predict without an accurate accounting of stability margins. More work, in both simple toy models and in commonly used acoustic devices such as the piezoelectric transducer studied in chapter 4, could elucidate the sources of instabilities and indicate design principles when including gain sources. There is still much that can be done in the area of active acoustic devices and metamaterials.

By stopping to consider the contributions made by research in acoustics, we see that the ability to harness acoustic waves has led to remarkable advances in our ability to communicate with each other and explore the world around us. This is perhaps most readily

evident by considering the loudspeaker and microphone, devices that are foundational to an incredible array of modern technologies. With access to more knowledge and computational resources than ever before, we continue to uncover new ways to manipulate acoustic waves. And, through this process, we can bring into existence the acoustic devices of the future. The work presented here is a step in that direction.

References

[1] M. Fink, D. Cassereau, A. Derode, C. Prada, P. Roux, M. Tanter, J. L. Thomas, and F. Wu, Time-reversed acoustics, Reports Prog. Phys. **63**, 1933 (2000).

[2] H. Helmholtz, Theorie der luftschwingungen in röhren mit offenen enden, J. Reine Angew. Math. **57**, 1 (1860).

[3] Lord Rayleigh, Some general theorems relating to vibrations, Proc. London Math. Soc. **s1-4**, 357 (1873).

[4] H. Nassar, B. Yousefzadeh, R. Fleury, M. Ruzzene, A. Alù, C. Daraio, A. N. Norris, G. Huang, and M. R. Haberman, Nonreciprocity in acoustic and elastic materials, Nat. Rev. Mater. **5**, 667 (2020).

[5] P. M. Morse and K. U. Ingard, *Theoretical Acoustics* (Princeton University Press, Princeton, 1986).

[6] C. P. Wiederhold, D. L. Sounas, and A. Alù, Nonreciprocal acoustic propagation and leaky-wave radiation in a waveguide with flow, J. Acoust. Soc. Am. **146**, 802 (2019).

[7] R. Adlakha, M. Moghaddaszadeh, M. A. Attarzadeh, A. Aref, and M. Nouh, Frequency selective wave beaming in nonreciprocal acoustic phased arrays, Sci. Rep. **10**, 21339 (2020).

[8] R. Fleury, D. L. Sounas, C. F. Sieck, M. R. Haberman, and A. Alù, Sound isolation and giant linear nonreciprocity in a compact acoustic circulator, Science **343**, 516 (2014).

[9] N. Janković and A. Alù, Glide-symmetric acoustic waveguides for extreme sensing and isolation, Phys. Rev. Appl. **15**, 024004 (2021).

[10] A. Darabi, X. Ni, M. Leamy, and A. Alù, Reconfigurable Floquet elastodynamic topological insulator based on synthetic angular momentum bias, Sci. Adv. **6**, eaba8656 (2020).

[11] N. Wang, R.-Y. Zhang, and C. T. Chan, Robust acoustic pulling using chiral surface waves, Phys. Rev. Appl. **15**, 24034 (2021).

[12] P. Gao, Z. Zhang, and J. Christensen, Sonic valley-Chern insulators, Phys. Rev. B **101**, 020301(R) (2020).

[13] A. Srivastava, Causality and passivity: From electromagnetism and network theory to metamaterials, Mech. Mater. **154**, 103710 (2021).

[14] M. B. Muhlestein, C. F. Sieck, A. Alù, and M. R. Haberman, Reciprocity, passivity and causality in Willis materials, Proc. R. Soc. A **472**, 20160604 (2016).

[15] R. Fleury, D. Sounas, and A. Alù, An invisible acoustic sensor based on parity-time symmetry, Nat. Commun. **6**, 5905 (2015).

[16] C. Coulais, R. Fleury, and J. van Wezel, Topology and broken Hermiticity, Nat. Phys. **17**, 9 (2021).

[17] Ø. Lind-Johansen, K. Seip, and J. Skaar, The perfect lens on a finite bandwidth, J. Math. Phys. **50**, 012908 (2009).

[18] B. Nistad and J. Skaar, Causality and electromagnetic properties of active media, Phys. Rev. E **78**, 036603 (2008).

[19] R. M. Foster, A reactance theorem, Bell Syst. Tech. J. **3**, 259 (1924).

[20] E. J. Skudrzyk, Vibrations of a system with a finite or an infinite number of resonances, J. Acoust. Soc. Am. **30**, 1140 (1958).

[21] C. Shi, M. Dubois, Y. Chen, L. Cheng, H. Ramezani, Y. Wang, and X. Zhang, Accessing the exceptional points of parity-time symmetric acoustics, Nat. Commun. **7**, 11110 (2016).

[22] X. Zhu, H. Ramezani, C. Shi, J. Zhu, and X. Zhang, PT-symmetric acoustics, Phys. Rev. X **4**, 031042 (2014).

[23] T. Liu, G. Ma, S. Liang, H. Gao, Z. Gu, S. An, and J. Zhu, Single-sided acoustic beam splitting based on parity-time symmetry, Phys. Rev. B **102**, 014306 (2020).

[24] H. Z. Chen, T. Liu, H. Y. Luan, R. J. Liu, X. Y. Wang, X. F. Zhu, Y. B. Li, Z. M. Gu, S. J. Liang, H. Gao, L. Lu, L. Ge, S. Zhang, J. Zhu, and R. M. Ma, Revealing the missing dimension at an exceptional point, Nat. Phys. **16**, 571 (2020).

[25] G. Ma and P. Sheng, Acoustic metamaterials: From local resonances to broad horizons, Sci. Adv. **2**, e1501595 (2016).

[26] S. A. Cummer, J. Christensen, and A. Alù, Controlling sound with acoustic metamaterials, Nat. Rev. Mater. **1**, 16001 (2016).

[27] Y. Wu, M. Yang, and P. Sheng, Perspective: Acoustic metamaterials in transition, J. Appl. Phys. **123**, 090901 (2018).

[28] C. Caloz, A. Alù, S. Tretyakov, D. Sounas, K. Achouri, and Z. L. Deck-Léger, Electromagnetic nonreciprocity, Phys. Rev. Appl. **10**, 047001 (2018).

[29] A. C. Tam, Applications of photoacoustic sensing techniques, Rev. Mod. Phys. **58**, 381 (1986).

[30] B. Liang, B. Yuan, and J. C. Cheng, Acoustic diode: Rectification of acoustic energy flux in one-dimensional systems, Phys. Rev. Lett. **103**, 104301 (2009).

[31] B. Liang, X. S. Guo, J. Tu, D. Zhang, and J. C. Cheng, An acoustic rectifier, Nat. Mater. **9**, 989 (2010).

[32] B. I. Popa and S. A. Cummer, Non-reciprocal and highly nonlinear active acoustic metamaterials, Nat. Commun. **5**, 3398 (2014).

[33] N. Boechler, G. Theocharis, and C. Daraio, Bifurcation-based acoustic switching

and rectification, Nat. Mater. **10**, 665 (2011).

[34] D. M. Pozar, *Microwave Engineering* (John Wiley & Sons, Hoboken, 2011).

[35] A. Kord, D. L. Sounas, and A. Alù, Microwave nonreciprocity, Proc. IEEE **108**, 1728 (2020).

[36] K. Fang, Z. Yu, and S. Fan, Realizing effective magnetic field for photons by controlling the phase of dynamic modulation, Nat. Photonics **6**, 782 (2012).

[37] Q. Lin and S. Fan, Light guiding by effective gauge field for photons, Phys. Rev. X **4**, 031031 (2014).

[38] D. L. Sounas, C. Caloz, and A. Alù, Giant non-reciprocity at the subwavelength scale using angular momentum-biased metamaterials, Nat. Commun. **4**, 2407 (2013).

[39] N. A. Estep, D. L. Sounas, J. Soric, and A. Alù, Magnetic-free non-reciprocity and isolation based on parametrically modulated coupled-resonator loops, Nat. Phys. **10**, 923 (2014).

[40] N. Reiskarimian and H. Krishnaswamy, Magnetic-free non-reciprocity based on staggered commutation, Nat. Commun. **7**, 11217 (2016).

[41] D. L. Sounas and A. Alù, Fundamental bounds on the operation of Fano nonlinear isolators, Phys. Rev. B **97**, 115431 (2018).

[42] D. L. Sounas, J. Soric, and A. Alù, Broadband passive isolators based on coupled nonlinear resonances, Nat. Electron. **1**, 113 (2018).

[43] K. Y. Yang, J. Skarda, M. Cotrufo, A. Dutt, G. H. Ahn, M. Sawaby, D. Vercruysse, A. Arbabian, S. Fan, A. Alù, and J. Vučković, Inverse-designed non-reciprocal pulse router for chip-based LiDAR, Nat. Photonics **14**, 369 (2020).

[44] S. P. Wallen and M. R. Haberman, Nonreciprocal wave phenomena in spring-mass chains with effective stiffness modulation induced by geometric nonlinearity, Phys. Rev. E **99**, 013001 (2019).

[45] A. Darabi, L. Fang, A. Mojahed, M. D. Fronk, A. F. Vakakis, and M. J. Leamy, Broadband passive nonlinear acoustic diode, Phys. Rev. B **99**, 214305 (2019).

[46] I. Grinberg, A. F. Vakakis, and O. V. Gendelman, Acoustic diode: Wave non-reciprocity in nonlinearly coupled waveguides, Wave Motion **83**, 49 (2018).

[47] J. Bunyan, K. J. Moore, A. Mojahed, M. D. Fronk, M. Leamy, S. Tawfick, and A. F. Vakakis, Acoustic nonreciprocity in a lattice incorporating nonlinearity, asymmetry, and internal scale hierarchy: Experimental study, Phys. Rev. E **97**, 052211 (2018).

[48] Y. Shi, Z. Yu, and S. Fan, Limitations of nonlinear optical isolators due to dynamic reciprocity, Nat. Photonics **9**, 388 (2015).

[49] Z. Yang, F. Gao, X. Shi, X. Lin, Z. Gao, Y. Chong, and B. Zhang, Topological acoustics, Phys. Rev. Lett. **114**, 114301 (2015).

[50] A. B. Khanikaev, R. Fleury, S. H. Mousavi, and A. Alù, Topologically robust sound propagation in an angular-momentum-biased graphene-like resonator lattice, Nat. Commun. **6**, 8260 (2015).

[51] Y. Ding, Y. Peng, Y. Zhu, X. Fan, J. Yang, B. Liang, X. Zhu, X. Wan, and J. Cheng, Experimental demonstration of acoustic chern insulators, Phys. Rev. Lett. **122**, 014302 (2019).

[52] R. Fleury, D. L. Sounas, and A. Alù, Subwavelength ultrasonic circulator based on spatiotemporal modulation, Phys. Rev. B **91**, 174306 (2015).

[53] C. Shen, J. Li, Z. Jia, Y. Xie, and S. A. Cummer, Nonreciprocal acoustic transmission in cascaded resonators via spatiotemporal modulation, Phys. Rev. B **99**, 134306 (2019).

[54] C. Shen, X. Zhu, J. Li, and S. A. Cummer, Nonreciprocal acoustic transmission in space-time modulated coupled resonators, Phys. Rev. B **100**, 054302 (2019).

[55] X. Zhu, J. Li, C. Shen, G. Zhang, S. A. Cummer, and L. Li, Tunable unidirectional compact acoustic amplifier via space-time modulated membranes, Phys. Rev. B **102**, 024309 (2020).

[56] Y. Chen, X. Li, H. Nassar, A. N. Norris, C. Daraio, and G. Huang, Nonreciprocal wave propagation in a continuum-based metamaterial with space-time modulated resonators, Phys. Rev. Appl. **11**, 064052 (2019).

[57] G. Trainiti and M. Ruzzene, Non-reciprocal elastic wave propagation in spatiotemporal periodic structures, New J. Phys. **18**, 083047 (2016).

[58] B. M. Goldsberry, S. P. Wallen, and M. R. Haberman, Non-reciprocal wave propagation in mechanically-modulated continuous elastic metamaterials, J. Acoust. Soc. Am. **146**, 782 (2019).

[59] J. R. Willis, Variational principles for dynamic problems for inhomogeneous elastic media, Wave Motion **3**, 1 (1981).

[60] G. W. Milton and J. R. Willis, On modifications of Newton's second law and linear continuum elastodynamics, Proc. R. Soc. A **463**, 855 (2007).

[61] A. N. Norris, A. L. Shuvalov, and A. A. Kutsenko, Analytical formulation of three-dimensional dynamic homogenization for periodic elastic systems, Proc. R. Soc. A **468**, 1629 (2012).

[62] C. F. Sieck, A. Alù, and M. R. Haberman, Origins of Willis coupling and acoustic bianisotropy in acoustic metamaterials through source-driven homogenization, Phys. Rev. B **96**, 104303 (2017).

[63] L. Quan, Y. Ra'di, D. L. Sounas, and A. Alù, Maximum Willis coupling in

acoustic scatterers, Phys. Rev. Lett. **120**, 254301 (2018).

[64] B. I. Popa, Y. Zhai, and H. S. Kwon, Broadband sound barriers with bianisotropic metasurfaces, Nat. Commun. **9**, 5299 (2018).

[65] Y. Zhai, H. S. Kwon, and B. I. Popa, Active Willis metamaterials for ultracompact nonreciprocal linear acoustic devices, Phys. Rev. B **99**, 220301(R) (2019).

[66] Y. Chen, X. Li, G. Hu, M. R. Haberman, and G. Huang, An active mechanical Willis meta-layer with asymmetric polarizabilities, Nat. Commun. **11**, 3681 (2020).

[67] H. Nassar, X. C. Xu, A. N. Norris, and G. L. Huang, Modulated phononic crystals: Non-reciprocal wave propagation and Willis materials, J. Mech. Phys. Solids **101**, 10 (2017).

[68] L. Quan, S. Yves, Y. Peng, H. Esfahlani, and A. Alù, Odd Willis coupling induced by broken time-reversal symmetry, Nat. Commun. **12**, 2615 (2021).

[69] Y. Wang, B. Yousefzadeh, H. Chen, H. Nassar, G. Huang, and C. Daraio, Observation of nonreciprocal wave propagation in a dynamic phononic lattice, Phys. Rev. Lett. **121**, 194301 (2018).

[70] L. Quan, D. L. Sounas, and A. Alù, Nonreciprocal Willis coupling in zero-index moving media, Phys. Rev. Lett. **123**, 064301 (2019).

[71] F. J. Fahy, Some applications of the reciprocity principle in experimental vibroacoustics, Acoust. Phys. **49**, 217 (2003).

[72] A. D. Pierce, *Acoustics: An Introduction to Its Physical Principles and Applications* (Acoustical Society of America, Woodbury, 1989).

[73] G. S. Kino, The application of reciprocity theory to scattering of acoustic waves by flaws, J. Appl. Phys. **49**, 3190 (1978).

[74] J. T. Fokkema and P. M. Van Den Berg, *Seismic Applications of Acoustic Reciprocity* (Elsevier Science, Amsterdam, 1993).

[75] Lord Rayleigh, On waves propagated along the plane surface of an elastic solid, Proc. London Math. Soc. **s1-17**, 4 (1885).

[76] P. Delsing, A. N. Cleland, M. J. A. Schuetz, J. Knörzer, G. Giedke, J. I. Cirac, K. Srinivasan, M. Wu, K. C. Balram, C. Baüerle, T. Meunier, C. J. B. Ford, P. V. Santos, E. Cerda-Méndez, H. Wang, H. J. Krenner, E. D. S. Nysten, M. Weiß, G. R. Nash, L. Thevenard, C. Gourdon, P. Rovillain, M. Marangolo, J. Y. Duquesne, G. Fischerauer, W. Ruile, A. Reiner, B. Paschke, D. Denysenko, D. Volkmer, A. Wixforth, H. Bruus, M. Wiklund, J. Reboud, J. M. Cooper, Y. Q. Fu, M. S. Brugger, F. Rehfeldt, and C. Westerhausen, The 2019 surface acoustic waves roadmap, J. Phys. D: Appl. Phys. **52**, 353001 (2019).

[77] C. K. Campbell, Applications of surface acoustic and shallow bulk acoustic wave

devices, Proc. IEEE **77**, 1453 (1989).

[78] R. E. Camley, Nonreciprocal surface waves, Surf. Sci. Rep. **7**, 103 (1987).

[79] J. Heil, B. Lüthi, and P. Thalmeier, Nonreciprocal surface-acoustic-wave propagation in aluminum, Phys. Rev. B **25**, 6515(R) (1982).

[80] P. J. Shah, D. A. Bas, I. Lisenkov, A. Matyushov, N. Sun, and M. R. Page, Giant nonreciprocity of surface acoustic waves enabled by the magnetoelastic interaction, Sci. Adv. **6**, eabc5648 (2020).

[81] R. Verba, V. Tiberkevich, and A. Slavin, Wide-band nonreciprocity of surface acoustic waves induced by magnetoelastic coupling with a synthetic antiferromagnet, Phys. Rev. Appl. **12**, 054061 (2019).

[82] R. Verba, I. Lisenkov, I. Krivorotov, V. Tiberkevich, and A. Slavin, Nonreciprocal surface acoustic waves in multilayers with magnetoelastic and interfacial Dzyaloshinskii-Moriya interactions, Phys. Rev. Appl. **9**, 064014 (2018).

[83] M. Kü, M. Heigl, L. Flacke, A. Hörner, M. Weiler, M. Albrecht, and A. Wixforth, Nonreciprocal Dzyaloshinskii-Moriya magnetoacoustic waves, Phys. Rev. Lett. **125**, 217203 (2020).

[84] T. Yu, Nonreciprocal surface magnetoelastic dynamics, Phys. Rev. B **102**, 134417 (2020).

[85] X. Zhang, G. E. W. Bauer, and T. Yu, Unidirectional pumping of phonons by magnetization dynamics, Phys. Rev. Lett. **125**, 077203 (2020).

[86] M. Xu, K. Yamamoto, J. Puebla, K. Baumgaertl, B. Rana, K. Miura, H. Takahashi, D. Grundler, S. Maekawa, and Y. Otani, Nonreciprocal surface acoustic wave propagation via magneto-rotation coupling, Sci. Adv. **6**, eabb1724 (2020).

[87] A. Mazzamurro, Y. Dusch, P. Pernod, O. Bou Matar, A. Addad, A. Talbi, and N. Tiercelin, Giant magnetoelastic coupling in a Love acoustic waveguide based on TbCo2 / Fe Co nanostructured film on ST-cut quartz, Phys. Rev. Appl. **13**, 044001 (2020).

[88] S. Tateno, Y. Nozaki, and Y. Nozaki, Highly nonreciprocal spin waves excited by magnetoelastic coupling in a Ni / Si bilayer, Phys. Rev. Appl. **13**, 034074 (2020).

[89] Q. Wu, H. Chen, H. Nassar, and G. Huang, Non-reciprocal Rayleigh wave propagation in space–time modulated surface, J. Mech. Phys. Solids **146**, 104196 (2021).

[90] A. Palermo, P. Celli, B. Yousefzadeh, C. Daraio, and A. Marzani, Surface wave non-reciprocity via time-modulated metamaterials, J. Mech. Phys. Solids **145**, 104181 (2020).

[91] C. Cassella, G. Michetti, M. Pirro, Y. Yu, A. Kord, D. L. Sounas, A. Alù, and M. Rinaldi, Radio frequency angular momentum biased quasi-LTI nonreciprocal

acoustic filters, IEEE Trans. Ultrason. Ferroelectr. Freq. Control **66**, 1814 (2019).

[92] Y. Yu, G. Michetti, M. Pirro, A. Kord, D. L. Sounas, Z. Xiao, C. Cassella, A. Alù, and M. Rinaldi, Radio frequency magnet-free circulators based on spatiotemporal modulation of surface acoustic wave filters, IEEE Trans. Microw. Theory Tech. **67**, 4773 (2019).

[93] X. Xu, Q. Wu, H. Chen, H. Nassar, Y. Chen, A. Norris, M. R. Haberman, and G. Huang, Physical observation of a robust acoustic pumping in waveguides with dynamic boundary, Phys. Rev. Lett. **125**, 253901 (2020).

[94] I. Brouzos, I. Kiorpelidis, F. K. Diakonos, and G. Theocharis, Fast, robust, and amplified transfer of topological edge modes on a time-varying mechanical chain, Phys. Rev. B **102**, 174312 (2020).

[95] D. Guéry-Odelin, A. Ruschhaupt, A. Kiely, E. Torrontegui, S. Martínez-Garaot, and J. G. Muga, Shortcuts to adiabaticity: Concepts, methods, and applications, Rev. Mod. Phys. **91**, 045001 (2019).

[96] L. Sirota, R. Ilan, Y. Shokef, and Y. Lahini, Non-Newtonian topological mechanical metamaterials using feedback control, Phys. Rev. Lett. **125**, 256802 (2020).

[97] A. Ghatak, M. Brandenbourger, J. Van Wezel, and C. Coulais, Observation of non-Hermitian topology and its bulk-edge correspondence in an active mechanical metamaterial, Proc. Natl. Acad. Sci. U.S.A. **47**, 29561 (2020).

[98] Y. Hadad, D. L. Sounas, and A. Alù, Space-time gradient metasurfaces, Phys. Rev. B **92**, 100304(R) (2015).

[99] M. F. Hamilton, Y. A. Il'inskii, and E. A. Zabolotskaya, Nonlinear surface acoustic waves in crystals, J. Acoust. Soc. Am. **105**, 639 (1999).

[100] A. P. Mayer, Surface acoustic waves in nonlinear elastic media, Phys. Rep. **256**, 237 (1995).

[101] H. Ge, X. Ni, Y. Tian, S. K. Gupta, M. H. Lu, X. Lin, W. D. Huang, C. T. Chan, and Y. F. Chen, Experimental observation of acoustic Weyl points and topological surface states, Phys. Rev. Appl. **10**, 014017 (2018).

[102] B. Xie, H. Liu, H. Cheng, Z. Liu, J. Tian, and S. Chen, Dirac points and the transition towards Weyl points in three-dimensional sonic crystals, Light Sci. Appl. **9**, 201 (2020).

[103] H. He, C. Qiu, X. Cai, M. Xiao, M. Ke, F. Zhang, and Z. Liu, Observation of quadratic Weyl points and double-helicoid arcs, Nat. Commun. **11**, 1820 (2020).

[104] A. Darabi and M. J. Leamy, Tunable nonlinear topological insulator for acoustic waves, Phys. Rev. Appl. **12**, 044030 (2019).

[105] R. Chaunsali and G. Theocharis, Self-induced topological transition in phononic

crystals by nonlinearity management, Phys. Rev. B **100**, 014302 (2019).

[106] Y. Hadad, J. C. Soric, A. B. Khanikaev, and A. Alù, Self-induced topological protection in nonlinear circuit arrays, Nat. Electron. **1**, 178 (2018).

[107] Y. Hadad, A. B. Khanikaev, and A. Alù, Self-induced topological transitions and edge states supported by nonlinear staggered potentials, Phys. Rev. B **93**, 155112 (2016).

[108] S. Shankar, A. Souslov, M. J. Bowick, M. Cristina Marchetti, and V. Vitelli, Topological active matter, ArXiv 2010.00364 (2020).

[109] M. C. Marchetti, J. F. Joanny, S. Ramaswamy, T. B. Liverpool, J. Prost, M. Rao, and R. A. Simha, Hydrodynamics of soft active matter, Rev. Mod. Phys. **85**, 1143 (2013).

[110] M. Brandenbourger, X. Locsin, E. Lerner, and C. Coulais, Non-reciprocal robotic metamaterials, Nat. Commun. **10**, 4608 (2019).

[111] H. Masoud and H. A. Stone, The reciprocal theorem in fluid dynamics and transport phenomena, J. Fluid Mech. **879**, P1 (2019).

[112] J. D. Achenbach, *Reciprocity in Elastodynamics* (Cambridge Univ. Press, Cambridge, 2004).

[113] A. A. Maznev, A. G. Every, and O. B. Wright, Reciprocity in reflection and transmission: What is a "phonon diode"?, Wave Motion **50**, 776 (2013).

[114] D. Jalas, A. Petrov, M. Eich, W. Freude, S. Fan, Z. Yu, R. Baets, M. Popović, A. Melloni, J. D. Joannopoulos, M. Vanwolleghem, C. R. Doerr, and H. Renner, What is-and what is not-an optical isolator, Nat. Photonics **7**, 579 (2013).

[115] R. Sasaki, Y. Nii, Y. Iguchi, and Y. Onose, Nonreciprocal propagation of surface acoustic wave in Ni/LiNbO3, Phys. Rev. B **95**, 020407 (2017).

[116] H. Nassar, H. Chen, A. N. Norris, M. R. Haberman, and G. L. Huang, Non-reciprocal wave propagation in modulated elastic metamaterials, Proc. R. Soc. A Math. Phys. Eng. Sci. **473**, 20170188 (2017).

[117] R. Fleury, D. Sounas, M. R. Haberman, and A. Alù, Nonreciprocal acoustics, Acoust. Today **11**, 14 (2015).

[118] M. B. Zanjani, A. R. Davoyan, A. M. Mahmoud, N. Engheta, and J. R. Lukes, One-way phonon isolation in acoustic waveguides, Appl. Phys. Lett. **104**, 081905 (2014).

[119] Y. Hadad, J. C. Soric, and A. Alù, Breaking temporal symmetries for emission and absorption, Proc. Natl. Acad. Sci. U.S.A. **113**, 3471 (2016).

[120] D. Correas-Serrano, J. S. Gomez-Diaz, D. L. Sounas, Y. Hadad, A. Alvarez-Melcon, and A. Alù, Nonreciprocal graphene devices and antennas based on spatiotemporal modulation, IEEE Antennas Wirel. Propag. Lett. **15**, 1529 (2016).

[121] R. Fleury, A. B. Khanikaev, and A. Alù, Floquet topological insulators for sound, Nat. Commun. **7**, 11744 (2016).

[122] N. Swinteck, S. Matsuo, K. Runge, J. O. Vasseur, P. Lucas, and P. A. Deymier, Bulk elastic waves with unidirectional backscattering-immune topological states in a time-dependent superlattice, J. Appl. Phys. **118**, 063103 (2015).

[123] S. H. Mousavi, A. B. Khanikaev, and Z. Wang, Topologically protected elastic waves in phononic metamaterials, Nat. Commun. **6**, 8682 (2015).

[124] Z. G. Chen and Y. Wu, Tunable topological phononic crystals, Phys. Rev. Appl. **5**, 054021 (2016).

[125] X. Ni, C. He, X. C. Sun, X. P. Liu, M. H. Lu, L. Feng, and Y. F. Chen, Topologically protected one-way edge mode in networks of acoustic resonators with circulating air flow, New J. Phys. **17**, 10 (2015).

[126] O. A. Godin, Reciprocity and energy theorems for waves in a compressible inhomogeneous moving fluid, Wave Motion **25**, 143 (1997).

[127] Z. M. Gu, J. Hu, B. Liang, X. Y. Zou, and J. C. Cheng, Broadband non-reciprocal transmission of sound with invariant frequency, Sci. Rep. **6**, 19824 (2016).

[128] E. Walker, A. Neogi, A. Bozhko, Y. Zubov, J. Arriaga, H. Heo, J. Ju, and A. A. Krokhin, Nonreciprocal linear transmission of sound in a viscous environment with broken P symmetry, Phys. Rev. Lett. **120**, 204501 (2018).

[129] P. Hariharan, *Optical Interferometry* (Academic Press, London, 2003).

[130] S. V. Gaponenko, *Introduction to Nanophotonics* (Cambridge University Press, New York, 2010).

[131] H. Dötsch, N. Bahlmann, O. Zhuromskyy, M. Hammer, L. Wilkens, R. Gerhardt, P. Hertel, and A. F. Popkov, Applications of magneto-optical waveguides in integrated optics: Review, J. Opt. Soc. Am. B **22**, 240 (2005).

[132] Y. Shoji, K. Miura, and T. Mizumoto, Optical nonreciprocal devices based on magneto-optical phase shift in silicon photonics, J. Opt. (United Kingdom) **18**, 013001 (2015).

[133] D. L. Sounas and A. Alù, Non-reciprocal photonics based on time modulation, Nat. Photonics **11**, 774 (2017).

[134] P. Dong, Travelling-wave Mach-Zehnder modulators functioning as optical isolators, Opt. Express **23**, 10498 (2015).

[135] L. B. Soldano and E. C. M. Pennings, Optical multi-mode interference devices vased on self-imaging: Principles and applications, J. Light. Technol. **13**, 615 (1995).

[136] F. Bongard, H. Lissek, and J. R. Mosig, Acoustic transmission line metamaterial with negative/zero/positive refractive index, Phys. Rev. B **82**, 094306 (2010).

[137] R. Ghaffarivardavagh, J. Nikolajczyk, S. Anderson, and X. Zhang, Ultra-open acoustic metamaterial silencer based on Fano-like interference, Phys. Rev. B **99**, 024302 (2019).

[138] J. N. Winn, S. Fan, J. D. Joannopoulos, and E. P. Ippen, Interband transitions in photonic crystals, Phys. Rev. B **59**, 1551 (1999).

[139] Z. Yu and S. Fan, Complete optical isolation created by indirect interband photonic transitions, Nat. Photonics **3**, 91 (2009).

[140] M. R. Haberman and M. D. Guild, Acoustic metamaterials, Phys. Today **69**, 42 (2016).

[141] L. J. Chu, Physical limitations of omni-directional antennas, J. Appl. Phys. **19**, 1163 (1948).

[142] D. F. Sievenpiper, D. C. Dawson, M. M. Jacob, T. Kanar, S. Kim, J. Long, and R. G. Quarfoth, Experimental validation of performance limits and design guidelines for small antennas, IEEE Trans. Antennas Propag. **60**, 8 (2012).

[143] J. S. McLean, A re-examination of the fundamental limits on the radiation Q of electrically small antennas, IEEE Trans. Antennas Propag. **44**, 672 (1996).

[144] R. L. Fante, Quality factor of general ideal antennas, IEEE Trans. Antennas Propag. **17**, 151 (1969).

[145] R. E. Collin and S. Rothschild, Evaluation of antenna Q, IEEE Trans. Antennas Propag. **12**, 23 (1964).

[146] M. A. Kemp, M. Franzi, A. Haase, E. Jongewaard, M. T. Whittaker, M. Kirkpatrick, and R. Sparr, A high Q piezoelectric resonator as a portable VLF transmitter, Nat. Commun. **10**, 1715 (2019).

[147] A. Babakhani, D. B. Rutledge, and A. Hajimiri, Transmitter architectures based on near-field direct antenna modulation, IEEE J. Solid-State Circuits **43**, 2674 (2008).

[148] M. Manteghi, Fundamental limits, bandwidth, and information rate of electrically small antennas: Increasing the throughput of an antenna without violating the thermodynamic Q-factor, IEEE Antennas Propag. Mag. **61**, 14 (2019).

[149] K. Schab, D. Huang, and J. J. Adams, Pulse characteristics of a direct antenna modulation transmitter, IEEE Access **7**, 30213 (2019).

[150] A. Shlivinski and Y. Hadad, Beyond the Bode-Fano bound: Wideband impedance matching for short pulses using temporal switching of transmission-line parameters, Phys. Rev. Lett. **121**, 204301 (2018).

[151] H. Li, A. Mekawy, and A. Alù, Beyond Chu's limit with Floquet impedance matching, Phys. Rev. Lett. **123**, 164102 (2019).

[152] J. A. Bickford, A. E. Duwel, M. S. Weinberg, R. S. McNabb, D. K. Freeman, and P. A. Ward, Performance of electrically small conventional and mechanical

antennas, IEEE Trans. Antennas Propag. **67**, 2209 (2019).

[153] S. Selvin, M. N. Srinivas Prasad, Y. Huang, and E. Wang, Spinning magnet antenna for VLF transmitting, in *2017 IEEE Antennas Propag. Soc. Int. Symp. Proc.* (2017), pp. 1477–1478.

[154] T. Shi, M. C. Tang, Z. Wu, H. X. Xu, and R. W. Ziolkowski, Improved signal-to-noise ratio, bandwidth-enhanced electrically small antenna augmented with internal non-Foster elements, IEEE Trans. Antennas Propag. **67**, 2763 (2019).

[155] S. D. Stearns, Non-Foster circuits and stability theory, in *IEEE Int. Symp. Antennas Propag.* (Spokane, WA, 2011), pp. 1942–1945.

[156] N. Zhu and R. W. Ziolkowski, Design and measurements of an electrically small, broad bandwidth, non-Foster circuit-augmented protractor antenna, Appl. Phys. Lett. **101**, 024107 (2012).

[157] H. C. Chen, H. Y. Yang, C. C. Kao, and T. G. Ma, Slot antenna with non-Foster and negative conductance matching in consecutive bands, IEEE Antennas Wirel. Propag. Lett. **18**, 1203 (2019).

[158] T. Y. Shih and N. Behdad, Wideband, non-Foster impedance matching of electrically small transmitting antennas, IEEE Trans. Antennas Propag. **66**, 5687 (2018).

[159] M. M. Jacob and D. F. Sievenpiper, Non-Foster matched antennas for high-power applications, IEEE Trans. Antennas Propag. **65**, 4461 (2017).

[160] M. M. Jacob and D. F. Sievenpiper, Gain and noise analysis of non-Foster matched antennas, IEEE Trans. Antennas Propag. **64**, 4993 (2016).

[161] S. Assawaworrarit, X. Yu, and S. Fan, Robust wireless power transfer using a nonlinear parity-time-symmetric circuit, Nature **546**, 387 (2017).

[162] S. E. Sussman-Fort and R. M. Rudish, Non-Foster impedance matching of electrically-small antennas, IEEE Trans. Antennas Propag. **57**, 2230 (2009).

[163] S. Hrabar, I. Krois, and D. Zanic, Improving stability of negative capacitors for use in active metamaterials and antennas, in *2018 IEEE Int. Symp. Antennas Propag. Usn. Natl. Radio Sci. Meet.* (Boston, MA, 2018), pp. 1901–1902.

[164] C. R. White, J. S. Colburn, and R. G. Nagele, A non-Foster VHF monopole antenna, IEEE Antennas Wirel. Propag. Lett. **11**, 584 (2012).

[165] J. Loncar, S. Hrabar, and D. Muha, Stability of simple lumped-distributed networks with negative capacitors, IEEE Trans. Antennas Propag. **65**, 390 (2017).

[166] S. D. Stearns, Stable band-pass non-Foster circuits, in *2015 IEEE Int. Symp. Antennas Propag. Usn. Natl. Radio Sci. Meet.* (2015), pp. 1386–1387.

[167] A. K. Morozov, D. C. Webb, C. S. Chiu, P. F. Worcester, M. A. Dzieciuch, H. Sagen, J. Y. Guigné, and T. W. Altshuler, High-efficient tunable sound sources for

ocean and bottom tomography, 15 years of operating history, in *Ocean. 2016 MTS/IEEE Monterey* (2016).

[168] A. K. Morozov and D. C. Webb, Low-frequency sound source for underwater sound propagation research and calibration, US10144035B1 (4 December 2018).

[169] J. A. Mann, J. Tichy, and A. J. Romano, Instantaneous and time-averaged energy transfer in acoustic fields, J. Acoust. Soc. Am. **82**, 17 (1987).

[170] C. H. Sherman and J. L. Butler, Power factor and tuning, in *Transducers Arrays Underw. Sound* (2007), pp. 69–73.

[171] J. T. Aberle and R. Loepsinger-Romak, *Antennas with Non-Foster Matching Networks* (Morgan & Claypool Publishers, 2007).

[172] E. Willard, Acoustic Transducer Design for Active Reflection Cancellation in a Finite Volume Wave Propagation Laboratory, The University of Texas at Austin, 2019.

[173] A. Alù, First-principles homogenization theory for periodic metamaterials, Phys. Rev. B **84**, 075153 (2011).

[174] R. W. Erickson and D. Maksimović, *Fundamentals of Power Electronics*, 3rd ed. (Springer, Cham, 2020).

[175] S. H. Lee, C. M. Park, Y. M. Seo, Z. G. Wang, and C. K. Kim, Acoustic metamaterial with negative modulus, J. Phys. Condens. Matter **21**, 175704 (2009).

[176] C. Balanis, *Antenna Theory: Analysis and Design, Fourth Edition* (John Wiley & Sons, Inc., Hoboken, 2016).

[177] I. Liberal and N. Engheta, Near-zero refractive index photonics, Nat. Photonics **11**, 149 (2017).

[178] N. Engheta, Pursuing near-zero response, Science **340**, 286 (2013).

[179] S. Enoch, G. Tayeb, P. Sabouroux, N. Guérin, and P. Vincent, A metamaterial for directive emission, Phys. Rev. Lett. **89**, 213902 (2002).

[180] R. W. Ziolkowski, Propagation in and scattering from a matched metamaterial having a zero index of refraction, Phys. Rev. E **70**, 12 (2004).

[181] R. Fleury and A. Alù, Extraordinary sound transmission through density-near-zero ultranarrow channels, Phys. Rev. Lett. **111**, 055501 (2013).

[182] Y. Jing, J. Xu, and N. X. Fang, Numerical study of a near-zero-index acoustic metamaterial, Phys. Lett. A **376**, 2834 (2012).

[183] N. Fang, D. Xi, J. Xu, M. Ambati, W. Srituravanich, C. Sun, and X. Zhang, Ultrasonic metamaterials with negative modulus, Nat. Mater. **5**, 452 (2006).

[184] S. H. Lee and O. B. Wright, Origin of negative density and modulus in acoustic metamaterials, Phys. Rev. B **93**, 024302 (2016).

[185] Y. Lai, Y. Wu, P. Sheng, and Z. Q. Zhang, Hybrid elastic solids, Nat. Mater. **10**, 620 (2011).

[186] M. Yang, G. Ma, Z. Yang, and P. Sheng, Coupled membranes with doubly negative mass density and bulk modulus, Phys. Rev. Lett. **110**, 134301 (2013).

[187] R. Graciá-Salgado, V. M. García-Chocano, D. Torrent, and J. Sánchez-Dehesa, Negative mass density and ρ-near-zero quasi-two-dimensional metamaterials: Design and applications, Phys. Rev. B **88**, 224305 (2013).

[188] M. Dubois, C. Shi, X. Zhu, Y. Wang, and X. Zhang, Observation of acoustic Dirac-like cone and double zero refractive index, Nat. Commun. **8**, 14871 (2017).

[189] Z. Liang and J. Li, Extreme acoustic metamaterial by coiling up space, Phys. Rev. Lett. **108**, 114301 (2012).

[190] J. Li and C. T. Chan, Double-negative acoustic metamaterial, Phys. Rev. E **70**, 4 (2004).

[191] Y. Cheng, C. Zhou, B. G. Yuan, D. J. Wu, Q. Wei, and X. J. Liu, Ultra-sparse metasurface for high reflection of low-frequency sound based on artificial Mie resonances, Nat. Mater. **14**, 1013 (2015).

[192] H. Esfahlani, M. S. Byrne, M. McDermott, and A. Alù, Acoustic supercoupling in a zero-compressibility waveguide, Research **2019**, 1 (2019).

[193] W. Rotman, Plasma simulation by artificial dielectrics and parallel-plate media, IRE Trans. Antennas Propag. **10**, 82 (1962).

[194] I. Liberal, A. M. Mahmoud, Y. Li, B. Edwards, and N. Engheta, Photonic doping of epsilon-near-zero media, Science **355**, 1058 (2017).

[195] R. Marqués, J. Martel, F. Mesa, and F. Medina, Left-handed-media simulation and transmission of EM waves in subwavelength split-ring-resonator-loaded metallic waveguides, Phys. Rev. Lett. **89**, 183901 (2002).

[196] M. G. Silveirinha and N. Engheta, Theory of supercoupling, squeezing wave energy, and field confinement in narrow channels and tight bends using ε near-zero metamaterials, Phys. Rev. B **76**, 245109 (2007).

[197] A. Alù, M. G. Silveirinha, A. Salandrino, and N. Engheta, Epsilon-near-zero metamaterials and electromagnetic sources: Tailoring the radiation phase pattern, Phys. Rev. B **75**, 155410 (2007).

[198] A. Epstein, J. P. S. Wong, and G. V. Eleftheriades, Cavity-excited Huygens metasurface antennas for near-unity aperture illumination efficiency from arbitrarily large apertures, Nat. Commun. **7**, 10360 (2016).

[199] C. J. Naify, M. D. Guild, C. A. Rohde, D. C. Calvo, and G. J. Orris, Demonstration of a directional sonic prism in two dimensions using an air-acoustic leaky wave antenna, Appl. Phys. Lett. **107**, 133505 (2015).

[200] C. J. Naify, C. N. Layman, T. P. Martin, M. Nicholas, D. C. Calvo, and G. J. Orris, Experimental realization of a variable index transmission line metamaterial as an acoustic leaky-wave antenna, Appl. Phys. Lett. **102**, 203508 (2013).

[201] B. Hou, J. Mei, M. Ke, W. Wen, Z. Liu, J. Shi, and P. Sheng, Tuning Fabry-Perot resonances via diffraction evanescent waves, Phys. Rev. B **76**, 054303 (2007).

[202] M. H. Lu, X. K. Liu, L. Feng, J. Li, C. P. Huang, Y. F. Chen, Y. Y. Zhu, S. N. Zhu, and N. Ben Ming, Extraordinary acoustic transmission through a 1D grating with very narrow apertures, Phys. Rev. Lett. **99**, 174301 (2007).

[203] H. Estrada, F. J. García De Abajo, P. Candelas, A. Uris, F. Belmar, and F. Meseguer, Angle-dependent ultrasonic transmission through plates with subwavelength hole arrays, Phys. Rev. Lett. **102**, 144301 (2009).

[204] D. T. Blackstock, *Fundamentals of Physical Acoustics* (Wiley-Interscience, New York, 2000).

[205] D.-Y. Maa, Theory and design of microperforated panel sound-absorbing constructions, Sci. Sin. **18**, 55 (1975).

[206] I. Liberal, A. M. Mahmoud, and N. Engheta, Geometry-invariant resonant cavities, Nat. Commun. **7**, 10989 (2016).

[207] B. D. Hughes, *Random Walks and Random Environments* (Clarendon Press, New York, 1995).

[208] Y. T. Lo, A mathematical theory of antenna arrays with randomly spaced elements, IEEE Trans. Antennas Propag. **12**, 257 (1964).

[209] B. D. Steinberg, The peak sidelobe of the phased array having randomly located elements, IEEE Trans. Antennas Propag. **20**, 129 (1972).

[210] N. Jin and Y. Rahmat-Samii, Advances in particle swarm optimization for antenna designs: Real-number, binary, single-objective and multiobjective implementations, IEEE Trans. Antennas Propag. **55**, 556 (2007).

[211] S. Karimkashi and A. A. Kishk, Invasive weed optimization and its features in electromagnetics, IEEE Trans. Antennas Propag. **58**, 1269 (2010).

[212] L. Zhou, H. Li, Y. Qin, Z. Wei, and C. T. Chan, Directive emissions from subwavelength metamaterial-based cavities, Appl. Phys. Lett. **86**, 1 (2005).

[213] A. Ourir, A. De Lustrac, and J. M. Lourtioz, All-metamaterial-based subwavelength cavities ($\lambda/60$) for ultrathin directive antennas, Appl. Phys. Lett. **88**, 084103 (2006).

[214] A. P. Feresidis and J. C. Vardaxoglou, High gain planar antenna using optimised partially reflective surfaces, IEE Proc. Microwaves, Antennas Propag. **148**, 345 (2001).

[215] C. Caloz and Z. L. Deck-Leger, Spacetime metamaterials-part I: general concepts,

IEEE Trans. Antennas Propag. **68**, 1569 (2020).

[216] A. M. Shaltout, V. M. Shalaev, and M. L. Brongersma, Spatiotemporal light control with active metasurfaces, Science **364**, eaat3100 (2019).

[217] J. Li, C. Shen, A. Díaz-Rubio, S. A. Tretyakov, and S. A. Cummer, Systematic design and experimental demonstration of bianisotropic metasurfaces for scattering-free manipulation of acoustic wavefronts, Nat. Commun. **9**, 1342 (2018).